

# Electronic strong coupling of molecular materials in the liquid phase

Hadi Bahsoun

▶ **To cite this version:**

Hadi Bahsoun. Electronic strong coupling of molecular materials in the liquid phase. Theoretical and/or physical chemistry. Université de Strasbourg, 2017. English. NNT : 2017STRAF030 . tel-01715288

**HAL Id: tel-01715288**
**https://theses.hal.science/tel-01715288**

Submitted on 22 Feb 2018

**HAL** is a multi-disciplinary open access archive for the deposit and dissemination of scientific research documents, whether they are published or not. The documents may come from teaching and research institutions in France or abroad, or from public or private research centers.

L'archive ouverte pluridisciplinaire **HAL**, est destinée au dépôt et à la diffusion de documents scientifiques de niveau recherche, publiés ou non, émanant des établissements d'enseignement et de recherche français ou étrangers, des laboratoires publics ou privés.

# UNIVERSITÉ DE STRASBOURG

*ÉCOLE DOCTORALE DES SCIENCES CHIMIQUES*

**ISIS (UMR 7006)**

**Laboratoires des Nanostructures**

# THÈSE présentée par :

**Hadi BAHSOUN**

Soutenue le : **14 Septembre 2017**

pour obtenir le grade de : **Docteur de l'université de Strasbourg**

Discipline/ Spécialité : Physique

# Electronic Strong Coupling of Molecular Materials in the Liquid Phase

**THÈSE dirigée par :**

**Prof. EBBESEN Thomas** — Professeur, Université de Strasbourg

**RAPPORTEURS :**

**Prof. GOMEZ RIVAS Jaime** — Professeur, Université Technique Eindhoven

**Prof. RUBIO Angel** — Professeur, Max Planck Institute for the Structure and Dynamics of Matter

---

**AUTRES MEMBRES DU JURY :**

**Dr. GENET Cyriaque** — Directeur, CNRS, Université de Strasbourg

# Acknowledgements

First, I want to dedicate my gratitude and appreciation to my supervisor Prof. Thomas W. Ebbesen for giving me the opportunity to have this PhD in his lab (Nanostructures laboratories), and for his trust to freely use all the available resources to serve this scientific project during the past three years. I learned a lot from his wide scientific knowledge and experience, and gained new approaches in science and life in general. He was always concerned to optimize the success of my work and his door was always open for guidance, support and advice.

I would particularly like to thank Dr. James A. Hutchison for all the scientific and experimental support he offered me, and for his follow up on my projects. His enthusiasm was a huge source of inspiration and motivation for me. My deepest appreciation goes to Dr. Eloïse Devaux for her technical support, teachings, and kindness. Her presence and patience in solving all the technical problems were the major reason behind the smooth running of experiments. I also thank Dr. Cyriaque Genet who was very careful to deliver the correct scientific picture, for his kind advice and also for accepting to be a member of my thesis jury.

Here, I seize the opportunity to express my gratitude to Prof. Angel Rubio and Prof. Jaime Gómez Rivas for accepting to be among the jury members of my thesis and for their time to evaluate my thesis report.

I want to thank all my colleagues at ISIS in general, and at Nanostructure Laboratories in particular. One can never wish for a more united and supportive team than the one that I worked with during my PhD. I have the honor to be one of you. For this, I dedicate special thanks to Jino George, Anoop Thomas, and Atef Shalabney for all their experimental support, and generosity in sharing their scientific knowledge and experiences. They are also close friends who were always there to provide me with personal support and helpful advice. I am indebted for Thibault Chervy, who proved to be an outstanding young scientist, an active team member, and a gentle person. He was my companion for the past three years; I learned much from him about the topic and he offered me a lot of help during critical stages of my thesis. I also thank Shaojun Wang for the time he spent to engage me

with his research projects and to help me improve my research skills. I also want to thank him for his own thesis which was a source of inspiration to mine.

I want to thank also my colleagues Xiaolan Zhong, Stefano Azzini, Robrecht Vergauwe, Oussama Sentissi, Gabriel Schnoering, and Yoseline Rosales-Cabara for their kind cooperation and for maintaining a friendly and positive atmosphere at work. And I also express my appreciation to Madam Marie-Claud Jouaiti who held the pressure of all the administrative work and made these procedures less time consuming.

I would like to express my deepest heartfelt gratitude to my parents, brothers, sisters, other family members and friends, who believed in me and supported me continuously on both moral and emotional levels. They never hesitated to keep pushing me forward, and surrounded me with all the love throughout these years. In this context, I want to thank my friend Amer Hamdi-Sakr for the wonderful 13 years of friendship, and for his company during this long scientific and life exploration journey (in Beirut, Dubai, and Strasbourg) which started in our second year of University, and I wish him all the success he deserves in his PhD and future plans.

Many thanks and respect to the French government and its people for their openness to host foreign students and treat them as their own citizens. I am also grateful for the University of Strasbourg for funding my project and managing all the beneficial formations and conferences, and to all its obliging staff members who always offered high quality service.

To all of you, thank you.

Hadi

**Contents**

Acknowledgements I

**I. Fundamentals 1**

**1. General Introduction 2**

1.1- Basics of Light-Matter Interaction……..... 2

1.2- Coupling Regimes: Weak Coupling and Strong Coupling……. 4

1.2.1- The Weak Coupling Regime…… 5

1.2.2- The Strong Coupling Regime……... 6

1.3- Brief History of Light-Matter Strong Coupling Research…….. 7

1.4- State-of-the-art Light-Molecule Strong Coupling…….. 10

1.5- Outline of This Thesis……. 15

**2. Theoretical Description of Strongly Coupled Systems 17**

2.1- Classical Description…….. 17

2.1.1- Anti-Crossing of Normal Modes…….. 17

2.1.2- Numerical Applications…… 22

2.2- Quantum Description…….. 25

2.2.1- Single Two-Level System…… 25

2.2.2- Collective Rabi Splitting…….. 30

**II. Results 32**

**3. Strong Coupling on Plasmonic Structures 33**

3.1- Surface Plasmon Polariton…….. 33

3.1.1- Dispersion of SPPs……... 35

3.1.2- The Evanescent Field of SPPs…….. 37

3.1.3- The Excitation of SPPs……. 39

3.1.4- Strong Coupling on Plasmonic Arrays……. 46

3.2- Wetting Properties Under Strong Coupling…… 48

3.2.1- Experimental Section…… 50

3.2.2- Results and Discussions……... 56
3.3- Conclusions …… 65

**4. Strong Coupling in Liquid Fabry-Perot Nanocavities 66**

4.1- The Physics of Fabry-Perot Cavities…… 67
4.2- Electronic Light-Molecule Strong Coupling in Liquid Fabry-Perot Nanocavities…… 70
4.2.1- Fabrication of Fabry-Perot Liquid Nanocavities ……. 71
4.2.2- Experimental Section…… 74
4.2.3- Results and Discussions……... 79
4.2.4- Quantum Yield Calculations…… 84
4.3- Conclusions …… 87

**Thesis Conclusions and Outlook 88**

References……. 91
Publications and Conferences…… 106

# Part I.

# Fundamentals

# CHAPTER 1:
# General Introduction

This chapter gives an introduction to the basics of light-matter interactions. The two fundamental interaction regimes, the weak and strong coupling regimes, will be discussed with an emphasis on the latter. A brief history of the theory of strong light-matter coupling will be provided, highlighting the important stages of emergence of this field. Some examples from state-of-the-art experiments on strong coupling of light with various material systems will be presented. Results on strong coupling of light with organic materials will be a particular focus, highlighting the need to explore this area further for both the fundamental science and applications.

## 1.1- Basics of Light-matter Interaction

Our visual perception of the world around us in all its forms and colors is governed by a myriad of diverse light-matter interactions. We have long striven to understand the reasons behind many visual observations, for instance, why do we see daylight on earth and darkness in outer space despite the permanent presence of the sun, why are some objects opaque while others are transparent, why do objects seem bent or closer to an external observer when they are in water? Over time, the understanding of light-matter interaction phenomena like scattering, transmission, refraction and dispersion have answered these questions and many others concerning the observable world around us.[1] This understanding grew phenomenally first with the advent of Maxwell's

*Electromagnetic Theory of Light* that treats the propagation of light classically, and then later with the view of the dual wave/particle nature of light put forward by Albert Einstein and the development of quantum theory starting with Max Planck.[2] Finally the fusion of the two theories into quantum electrodynamics (QED) has taken the study of light-matter interactions from the macroscopic scale to the single photon-atom level.[3]

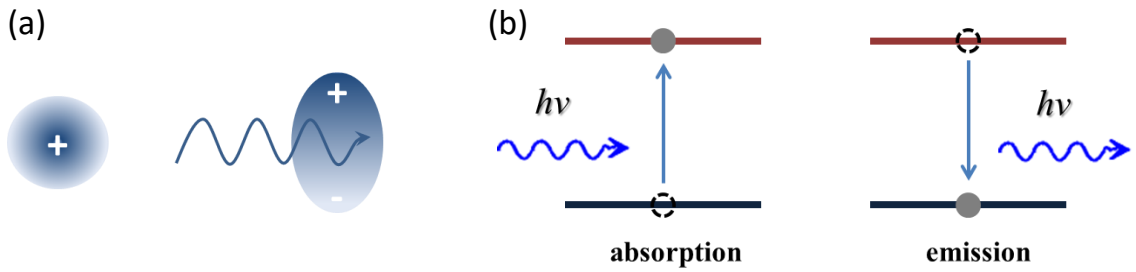



**Figure 1.1:** Schematic representation of basic light-matter interaction. (a) Atom with a positively charged center and its electronic cloud before and after its interaction with light which leads to the formation of a transient dipole moment. (b) Successive absorption and emission of a photon of energy *hv* by a two-level atom/molecule.

Two basic events that govern many interactions of light with a material are the successive absorption and emission of a photon by an absorber. When a photon with energy *hv* strikes a material (for example a two-level atom as schematically presented in Figure 1.1a) having a transition with same energy, the photon is absorbed by the atom via a dipole coupling interaction, leaving the atom in an excited state. The atom can return to its ground state by releasing a photon with the same energy *hv* (as can be seen in Figure 1.1b), conserving the total energy of the system. Of course many other types of light-matter interaction may take place depending on the properties of the light field (frequency, polarization, and intensity), the material (size, chemical composition, electronic density, etc…), and the circumstances of the interaction (environment, phase relationships, angle of incidence, etc…).

In general we can define two light-matter interaction regimes: the weak and the strong coupling regimes, which depend on the fate of the photon after the absorption/emission process discussed above. If, after emission, the photon propagates away and is lost to the system, the interaction is 'weak', and the photon and atom remain separately measureable entities. If however the two species (photon and absorber) are placed in an environment where they are allowed to continuously interact by multiple absorption/emission events, the interaction can enter the strong coupling regime where the photon and atom become hybridized leading to the formation of new hybrid light-matter eigen-states. In this thesis, we seek to explore such hybrid light-matter states involving molecules and investigate their properties.

## 1.2- Coupling Regimes: Weak Coupling and Strong Coupling

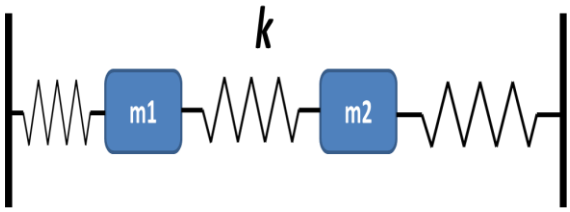



**Figure 1.2:** Schematic of a coupled oscillator system: two harmonic oscillators, represented as two weights, $m_1$ and $m_2$, attached by a spring to a surface, coupled by, and exchanging energy through, a spring of coupling strength *k*.

Any two harmonic oscillators that are allowed to exchange energy can be considered as a single coupled oscillator system. For instance, two mechanical oscillators can exchange energy through a spring of coupling strength *k*, connecting them (Figure 1.2a), while some energy is lost to the environment by friction. The coupled system exhibits very different behavior depending upon the quantitative relationship between the two processes i.e the energy exchange and energy losses. The notion of moving from the weak to the strong coupling regime is tied to exactly this change of behavior at the

threshold where the rate of energy exchange overcomes the rate of energy dissipation. In analogy to this system, the energy exchange between light and matter is mediated by coupling factor whose strength will determine the coupling regime. Further discussion about the coupling strength in the case of light-matter interaction is presented in the next chapter.

## 1.2.1- The Weak Coupling Regime

In the weak coupling regime, where losses overwhelm energy exchange between the oscillators, modifications to the original frequencies of the coupled oscillators in Figure 1.2 are minor. Returning from the classical model in Figure 1.2 to the dipole coupling between a light field of a cavity and an atom, a similar behavior is observed qualitatively. For instance, the radiative rate of the atom can be modified by the interaction but the molecule emission frequency remains unchanged.[4] An example is the Purcell effect[5] whereby the spontaneous emission rate is either enhanced or inhibited due to the modified photonic mode density inside an optical cavity. This effect will be further explored and demonstrated experimentally in chapter 5.

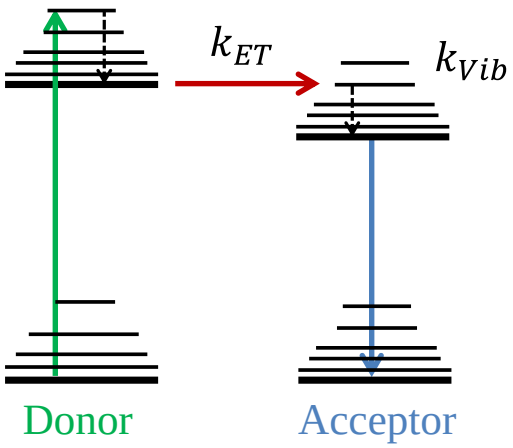



**Figure 1.3:** Förster energy transfer mechanism between singlet dipole-dipole interactions.

Another example of weak coupling, this time between the transition dipoles of two absorbers, is Förster energy transfer[6] between donor and acceptor molecules. In the case of molecules having resonant emission and absorption transitions (see Figure 1.3), the energy transfer is irreversible when transfer rate ($k_{ET}$) from donor to acceptor is smaller than the relaxation rate ($k_{Vib}$) of the acceptor. In contrast, when $k_{ET}$ is greater than any other relaxation mechanisms of the excited state, back and forth transfer of energy can occur and the system enters the strong coupling regime. In this limit, new delocalized eigenstates that extend collectively over several molecules are generated, known as excitons as proposed by Davydov.[7] A similar reshaping of the energy levels of the system occurs via strong coupling of photons and matter as will be discussed in the next section.

## 1.2.2- The Strong Coupling Regime

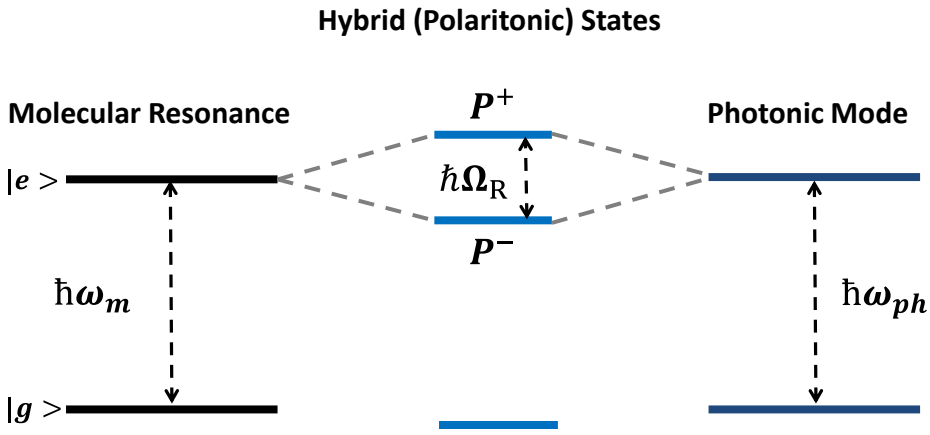



**Figure 1.4:** Formation of two hybrid polaritonic states due to light-matter strong coupling

Under certain conditions, a transition dipole moment of a two-level system can exchange energy with a resonant light mode (Figure 1.4). Again, the strong coupling is achieved when the energy exchange rate exceeds all dissipation processes during the interaction. . Here we note that dissipations in the system can occur through the EM mode (radiative decay), or by the relaxation pathway of the excited state.[8–11] When the above conditions are achieved, the phenomenon of strong coupling gives rise to two new light-

matter hybrid states known as polaritonic states. In the quantum electrodynamics point of view, these new states, P+ and P- presented in Figure 1.4, inherit both fermionic and bosonic properties from the coupled constituents.[9] The hybrid states are separated by an energy called the Rabi splitting which is directly proportional to the product of transition dipole moment of the material and the electric field magnitude. Further explanation about the quantitative and qualitative properties of these states is discussed in Chapter 2.

When the light-matter strong coupling involve the interaction of many molecules with one optical mode, the hybrid states are delocalized over many molecules and the Rabi splitting is enhanced, thereby affecting the properties of the coupled system. As detailed in Chapter 2, the condition of strong coupling can be achieved even in the absence of light due to the interaction of the zero-point energy fluctuations of the optical mode and the transition dipole moment of the molecules. The light-matter strong coupling can be achieved with different optical structures. Our focus in this thesis will be on strongly coupling molecules to resonant surface plasmon polaritons (SPP) modes (Chapter 3), and with resonant Fabry-Perot (FP) cavity modes (Chapters 4).

## 1.3- Brief History of Light-Matter Strong Coupling Research

The first experimental observations of self-induced Rabi oscillations were reported by S. Haroche's group in 1983,[10] putting *N* Rydberg atoms into a resonant cavity with high finesse. Later, in 1987,[11] a subsequent experiment was done on a single Rydberg atom in a superconducting cavity showing quantum "collapse and revival" of the Rabi oscillations predicted by the Janes-Cumming model. However, it wasn't until 1989 that the first optical observation of normal-mode splitting of *N* Rydberg atoms in an optical cavity[12] was established. The experiment was repeated in 1992,[13] and normal mode splitting was also observed but this time of a single atom coupled within a cavity with superconductive mirrors. These results provided an experimental validation for the theory of strong

coupling and took the first steps on the journey towards exploring the rising field of so-called cavity quantum electrodynamics.[14,15]

Consequently cavity quantum electrodynamics attracted the interest of solid state physicists, and strong coupling was implemented on semiconductors such as quantum dots and quantum wells.[16,17] Excitons, or electron-hole pairs, were coupled with resonant photonic modes giving rise to exciton-polaritons. The first exciton-polariton mode splitting was demonstrated by C. Weisbuch et al. in 1992,[18] who succeeded in spectrally resolving the Rabi splitting for GaAs quantum wells imbedded in distributed Bragg's reflectors (DBR) Fabry-Perot (FP) cavities. It was noticeable that larger Rabi splitting values were recorded for exciton-polaritons as compared with those occurred in the case of atoms-cavity systems, and this is due to the larger number of dipoles contributing to the energy exchange in the cavities. Subsequent experiments were performed to explore photoluminescence properties of exciton-polaritons.[19] For instance, the polariton dispersion curve was deduced from angle resolved photoluminescence measurements and validated the theoretical dispersion of the exciton-polaritons.[20] Other contemporary studies investigating exciton-polaritons dynamics[21,22] have led to the observation of Bose Einstein Condensates (BEC) and superfluidity in semiconductor planar micro-cavities embedding quantum wells.[23]

In general, relatively low values of Rabi splitting energies result from the coupling of inorganic semiconductors (in the order of 10 meV).[24] This is due to the low binding energy of the Wannier-Mott (WM) type of excitons[25] taking part in the coupling process. WM excitons have large radii (larger than the lattice distances of the crystal) and consequently low effective mass due to the large electric field screening the Coulomb's forces that holds them to their nuclei. Hence WM exciton binding energies can be less than thermal energy at room temperature (~26 meV at room temperature) making them unstable, with concomitant broadening of their transition line-widths making it difficult to resolve the Rabi splitting. Under such circumstances, special conditions (cryogenic set ups and very high Q-factor DBRs) are required to clearly observe the Rabi splitting in inorganic semiconductors. For this reason, attention turned towards excitons with binding energies that are large enough to observe the Rabi energy oscillations at room temperature.

This was established on systems like GaN in high finesse DBRs,[26] CdSe nanocrystals coupled to surface plasmon polaritons,[27] two-dimensional $MoS_2$ atomic crystals,[28] two-dimensional $WS_2$ monolayers coupled to surface plasmons,[29] and single QD strongly coupled with single photon in high Q micro-cavity.[30] These results have significant impact on many applications like nonlinear optics and quantum information processing.[24]

Influenced by the coupling of phonon modes to surface plasmons,[31] light-organic molecule strong coupling was demonstrated for the first time by Pockrand et al. in 1983[32] when they coupled cyanine dye molecules to resonant plasmon polaritons on Ag surface. Nevertheless, little attention was given to organic molecule strong coupling at that time. Only after two papers on light-molecule strong coupling were published in 1998[33,34] did the interest to employ molecules in the strong coupling research increase, leading eventually to the observation of room temperature lasing[35,36] and polariton condensation,[37,38] in 2014. Interestingly, organic molecules exhibit a set of characteristics which give them advantages over inorganic semiconductors for strong coupling. Firstly, their excitons are of the Frenkel type, displaying large transition dipole moment[39] and higher binding energies (~0.1 to 1eV) as compared to WM-type excitons. Secondly, high concentrations of molecules can be confined in small volumes to collectively interact with a photonic mode. These features allow high values of Rabi splitting to be observed at room temperature even within low Q-factor cavities. For instance, light-molecule strong coupling with a Rabi splitting of 700 meV was reported in 2011, representing 32 % of the molecule's transition energy,[40] using a photochrome coupled to either a metallic FP cavity or a plasmonic mode, consequently putting the system in the ultra-strong coupling regime.[40–44]

Another exciting feature of using molecules for strong coupling is that they can exist as liquids, gases, and solutes, allowing the exploration of strong coupling in a great variety of phases of matter. Liquid phase strong coupling was demonstrated very recently at the nanostructures laboratory in ISIS-Strasbourg, by the coupling of a vibrational transition of Citronellal in a micro-fluidic FP cavity.[45] Subsequent experiments reported the first multi-mode Rabi splitting in the vibrational states of strongly coupled $Fe(CO)_5$ in

the liquid phase.[42] Such ultra-strong coupling modifies the optical, molecular and material properties of the coupled system.

## 1.4- State-of-the-Art Light-Molecule Strong Coupling

As mentioned earlier, the strong interaction of cavity electromagnetic modes with molecules can drastically alter the states of molecules allowing for new possibilities to control the properties of this quantum-mechanical ensemble.[46] In the past few years, extensive effort from different teams[9,37,41,47–50] was invested in exploring the properties of strongly coupled molecular systems towards fundamental understanding and potential applications. Molecules with various properties were studied under strong coupling in order to investigate physical phenomena,[35,37,38] devices,[40,47,51,52] and any consequence for material and molecular science.[47,53,54] For example J-aggregates were extensively employed in strong coupling research,[32,55–63] due to their well suited characteristics including intense, narrow absorption and emission peaks and small Stokes shifts. In the next few paragraphs the state-of-the-art of the photophysical, chemical, and dynamical properties of polaritonic eigenstates arising from light-molecule strong coupling will be summarized.

In 2005, the first demonstration of strong coupling of an organic light emitting diode (LED) in a microcavity was reported by Bulović and his team.[61] Thin films of polyelectrolyte J-aggregate dyes embedded in a resonant microcavity were shown to emit upon electrical injection of carriers. Subsequently, Kéna-Cohen and his team showed that organic LED's electroluminescence can be achieved at lower voltages under ultra-strong coupling.[51] They also demonstrated in the same paper an enhancement in external quantum efficiency due to ultra-strong coupling which could impact the development of organic LEDs. In 2010, Kéna-Cohen and Forrest reported the room temperature lasing of polaritons arising from the coupling of melt-grown anthracene single crystals sandwiched between DBR mirrors,[35] the result which was also reported very recently by Gomez Rivas and his team, but this time via the coupling of organic rylene dye with resonant surface plasmons on top of silver array.[36] Shortly afterward, temporal and spatial coherence of

emission from hybrid polaritons were studied. For instance the real-time observation (on 10 fs scale) of ultrafast Rabi oscillation in a J-aggregate/metal nanostructure was reported by Lienau's group,[62] indicating coherent energy transfer between excitons and SPP fields. On the other hand, in 2012 Bellessa and coworkers[63] reported spatial coherence of emission from disordered J-aggregates strongly coupled to the surface plasmon polaritons of a metallic film, an effect that is absent in the weak coupling regime. Two years later, Törmä and coworkers[64] studied the evolution of spatial coherence properties of organic fluorescent molecules coupled to plasmonic surface lattice resonances as their system went from the weak to strong coupling regime. Two groups reported room temperature polariton condensation.[37,38] These findings show that organic molecule polaritonic states can allow the study of quantum condensates under ambient conditions and might benefit soft matter optoelectronic devices.[65] In the same context, Chervy et al. have very recently investigated second harmonic generation (SHG) of polaritons.[66] Using porphyrin nanofiber crystals in a metallic cavity, they observed an enhancement by 2 orders of magnitude of the SHG efficiency from the lower polaritons as compared to that of the same material outside the microcavity. Recently strong coupling of a few molecules with plasmonic nanocavities at room temperature was reported by Baumberg and colleagues.[67] The latter results promise to have numerous applications including single-photon emitters and nonlinear optics.

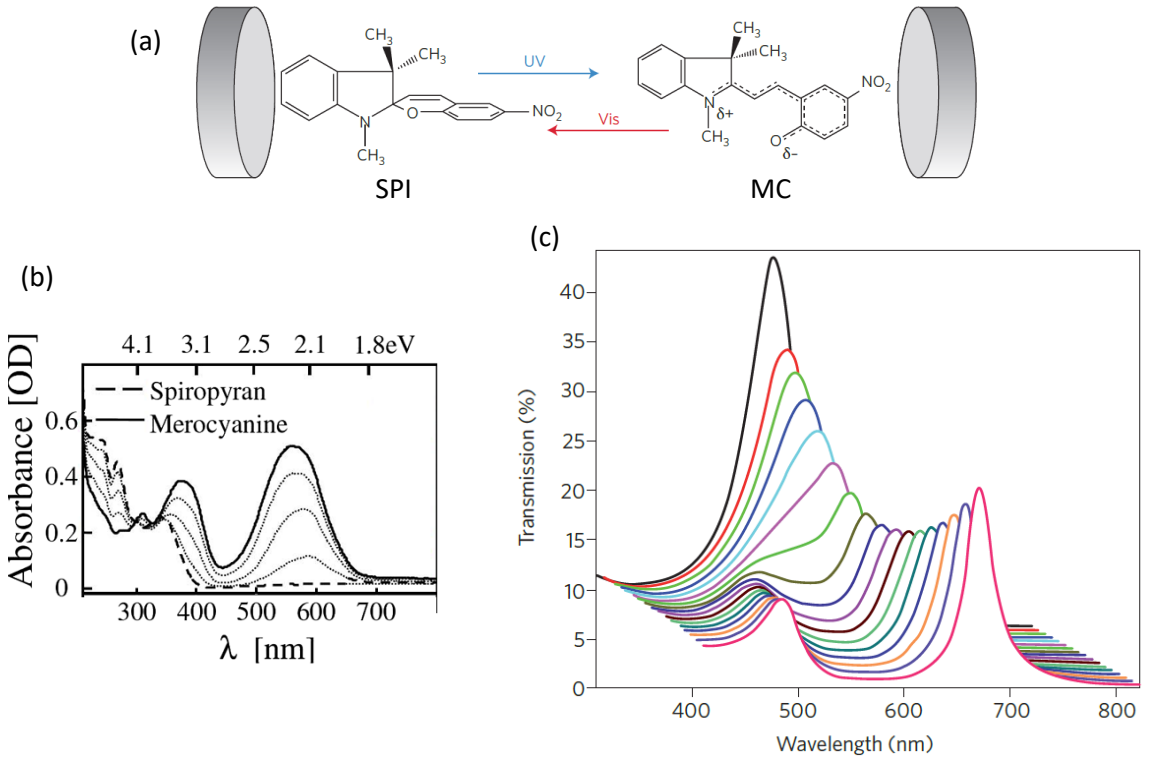



**Figure 1.5:** Observing ultra-strong coupling. (a) Schematic of the photochromic conversion between merocyanine (MC) and spiropyran (SP) in a micro-cavity. (b) Absorption spectra for a film in the SPI (dashed line) and MC (solid line) forms. (c) The evolution of transmission spectrum of the coupled system under UV illumination. The initial (black) spectrum corresponds to the cavity transmission in presence of SP molecules. By exposing SP to 330 nm UV light, they are converted into MC, resulting in resonance with the cavity. As the concentration of MC increases, a transition from weak to strong coupling and eventually ultrastrong coupling occurs. Figures are from references [40,46,68].[40,46,68]

So far we have discussed how light-molecule strong coupling is manifested in quantum physics and photo-physical phenomena. However, this is not the sole province in which strong coupling can play a role. In fact, over the past decade the study of strong coupling has been shown to modify chemical and bulk properties of the molecules. For instance, Hutchison et al. studied the strong coupling of a photochromic cyanine dye which experiences reversible conversion from a colorless molecule to one with a well-defined absorption band at 560 nm under illumination with UV light (visible light for the reverse process),[40] allowing the system to switch from the weak to the ultra-strong coupling regime and vice-versa via sample irradiation (see Figure 1.5). Accordingly, they were able to show

the rate of evolution of the photochrome towards the photostationary state decreased and the yield increased under strong coupling.[69] They have also examined the same system to show bulk modification of the work-function of these molecules when coupled to a resonant metallic cavity as well as surface plasmon resonances.[53] Note that this system was involved in the experiments in Chapter 3 of the thesis. The conductivity of a semi-conducting molecules can be enhanced when strongly coupled to surface plasmon polaritons.[47] Wang et al. reported that strong coupling could influence the hysteresis and dynamics of a perovskite phase transition.[70]

Another interesting feature of the delocalized wave functions of the polaritonic states is that they can alter the distance-dependence of energy transfer processes between two species. Recently it was shown that non-radiative energy transfer is characterized by a larger critical distance under strong coupling compared to that for a pure Förster-type process.[48,71] The length-scale of the energy transfer becomes defined by the extent of the cavity mode (typically larger than 200 nm) to which the molecules are coupled, rather than typical Forster distance of a few nanometres. The observation of double vacuum Rabi splitting due to coupling of two molecules to a single optical mode provides the possibility for energy transfer processes to occur among the hybrid modes.[72] Very recently, Zhong et al. reported amplified non-radiative energy transfer between two J-aggregate cyanine dyes strongly coupled to the vacuum field of a cavity.[60] With the help of femtosecond transient-transmission spectroscopy, they were able to extract the transfer rates and demonstrate enhancement by a factor of 7 as compared with the uncoupled system. They explained this behavior by the presence of delocalized hybrid states that played the role of a connector between the donor and acceptor molecules. The ability to transfer energy over distances comparable to the wavelength of light has vast implications for light-harvesting systems, solar energy conversion, and coherent energy transport.[48,60,71,72]

The strong coupling of molecular vibrational modes is a promising direction for modifying chemical reactions.[73–75] Vibrational transitions are found in the IR so that micro-fluiduic FP cavities can be used for such studies.[45] In the ultra-strong coupling regime, multiple Rabi splittings can be observed.[42] In 2016, using a simple deprotection reaction, the Strasbourg group demonstrated that not only is the chemical reaction rate reduced

under vibrational strong coupling but more importantly the activation enthalpy and entropy of the reaction significantly modified indicating a change in the reaction mechanism.[76] Very recently, Rabi splitting of protein vibrational modes strongly coupled to resonant IR modes,[77] and the strong coupling of electronic excitations of chlorosomes[78] were reported. These initial reports will very likely attract scientists from biological backgrounds to exploit the phenomenon of strong coupling in their future research.

All this experimental work has stimulated many theoretical studies and has led to the developments of new approaches to handle the complexity of the strongly coupled molecular system.[79–85] In so doing, many of the experimental results have been confirmed and new predictions have emerged and thereby enriching the strong coupling field. Needless to say that such system are very different from the the two-level Jaynes-Cummings theory discussed in Chapter 2.

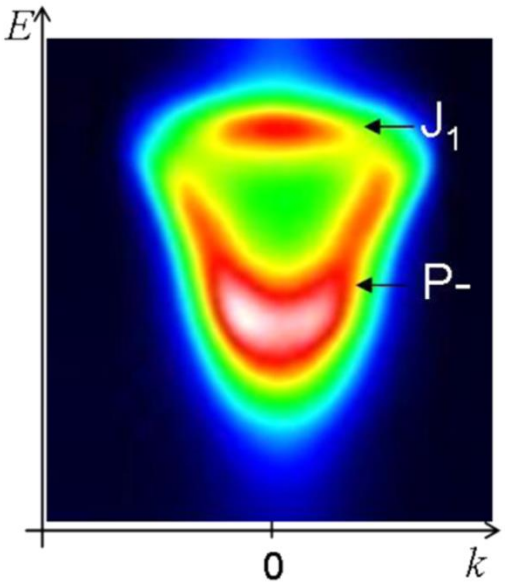



**Figure 1.6:** Emission of a strongly coupled dye molecule plotted as a function of $k_{//}$. The nondispersive emission is from the uncoupled molecules ($J_1$) in the cavity, while the coupled ones give rise to dispersive emission from the lower polaritons (P-). Figure is taken from references [9, 59]. [9,59]

Polariton dynamics has been the focus of interest of many researchers. Polariton states lifetime, relaxation processes and quantum efficiencies were studied.[59,86,87] A

thorough study was carried out by Schwartz et al. investigating the polariton dynamics under strong coupling.[56] They used steady-state and femtosecond time-resolved emission and absorption spectrometry on a J-aggregate cavity system to demonstrate the unexpected long lifetime of the lower polariton states. Later Wang et al. studied the strong coupling emission quantum efficiency by acquiring the emission as a function of the position of the active molecular layer inside a metallic resonant cavity.[59] The emission from the lower polaritons P- was observed to be dispersive as shown in Figure 1.6, emphasizing the bosonic quality of the polaritonic states. However, they found that the polariton decay is dominated by non-radiative processes resulting in low quantum yields. The lifetime of these hybrids were also reported, and a longer lifetime was recorded by the lower polaritons compared with those of the bare molecules, which was explained by the non-Markovian character of the relaxation process.[88] Polariton dynamics and photophysical properties constitute part of our study in this thesis, as described in Chapter 4.

## 1.5- Outline of This Thesis

It is clear from the past two sections that understanding light-matter strong coupling is evolving and gradually unveiling new and exciting phenomena. The field is advancing at good pace and leading towards promising applications. Nevertheless, there are still many unsolved issues concerning light-molecule strong coupling that require examination. Strong coupling theory has mostly been well developed beyond the two level systems to date, and is showing progress when applied with systems involving much more complicated energy diagram, as in the case of molecules. In this thesis we report further studies of light-molecule strong coupling which we hope will contribute to the overall understanding of this phenomenon and its potentials.

In the next chapter, derivation of the theoretical framework for strong coupling phenomena will be presented and explained. The quantitative description of the Rabi splitting for an ensemble of $N$ molecules shall be represented from the classical and quantum point of views. Based on results showing bulk property changes, we were interested to test whether those modifications could possibly affect the surface energy of

strongly coupled materials. In Chapter 3, we will describe an attempt to find a way to answer this question and discuss the challenges faced during those experiments.

In all of the experiments to date, electronic excitations coupled to light modes were studied with systems having molecules in the solid phase. Mixed within polymer matrices, molecules are restricted in terms of rotation and diffusion, restricting some relaxation pathways and thus limiting the dynamics study of the hybrid states. In Chapter 4, we demonstrate the excitonic state strong coupling of molecules mixed in liquid solution in resonance with an especially designed Fabry-Perot nano-cavity. Theses liquid FP nanocavities will be characterized, and the relation between the value of Rabi splitting and the number of coupled molecules $N$ will be experimentally demonstrated. Then, in the same chapter, a study of the dynamics and the photo-physical properties in the weak and strong coupling regime of a chlorin dye is reported. A comparison between our results and ones reported for similar studies will be provided.

# CHAPTER 2:
# Theoretical Description of Strongly Coupled Systems

The mechanism of strong light-matter interactions has been investigated theoretically from different point of views: classical, semi-classical, and quantum. Some of the basic features of strong coupling that we discussed in the previous section, such as the anti-crossing behavior, Rabi splitting, and delocalized wave functions of the hybrid states are described in this chapter by using theoretical models. Classically, we have treated the matter as a Lorentzian oscillator driven by an electric field force. We have also performed numerical applications to predict the behavior of organic molecules in a resonant cavity. From the quantum point of view, a single two level system interacting with a single optical mode was treated using Janes-Cumming Hamiltonian. For an ensemble of N-molecules, we have adapted Dicke's Hamiltonian to show the collective property of Rabi splitting.

## 2.1- Classical Description

### 2.1.1- Anti-crossing of Normal Modes

In order to study the strong interaction, we begin by considering the matter as a classical Lorentzian oscillator[2,89] composed of a point-like electric dipole oscillating with a frequency $\omega_0$. Since we are dealing with the system from a classical point of view, the

dipole is considered to be driven by a harmonic force created by the electric field *E(r,t)*, and consequently displaced by a distance $r$ from its equilibrium position. With such considerations, the equation of motion of the electron under the force of the field is:

$$m\frac{d^2r}{dt^2} + m\gamma\frac{dr}{dt} + \omega_0^2 mr = -eE(r,t) \tag{2.1}$$

where $m$ is the mass of the electron and $e$ is its charge, and $\gamma$ represents the energy dissipated in the system due to damping forces. The local field of the charges and all other magnetic forces were neglected[90] in equation (2.1). Since the electron displacement is very small compared to the wavelength of the EM-field in the visible range, then *E(r,t)* is constant in $r(t)=r\,e^{-i\omega t}$ and varies harmonically with time as $e^{-i\omega t}$ where $\omega$ is the frequency of the field. Consequently, the electron's motion will follow the same harmonic time dependence as that of the driving field force. Therefore, after applying these assumptions and performing simple derivatives, equation (2.1) will become:

$$m(-\omega^2 - i\omega\gamma + \omega_0^2)r = -eE \tag{2.2}$$

Now consider a set of $N$ electrons are experiencing harmonic movement upon the interaction with the field. If each electron is polarized by –er, then the polarization density $P$ of the electrons present in a unit volume $V$ is given by:

$$P = -\frac{N}{V}er \tag{2.3}$$

Substituting (2.2) in (2.3) will give:

$$P = \frac{Ne^2}{mV}\frac{1}{(\omega_0^2 - \omega^2 - i\omega\gamma)}E \tag{2.4}$$

However, the macroscopic linear polarization of a dipole is defined as:

$$P = \varepsilon_0\chi E \tag{2.5}$$

where $\chi$ is the electric susceptibility of the matter, and $\varepsilon_0$ is the permittivity in vacuum. Also by simple substitution, one can obtain $\chi$ as a function of $\omega$:

$$\chi(\omega) = \frac{A}{(\omega_0^2 - \omega^2 - i\omega\gamma)} \tag{2.6}$$

where we have substituted in $A$ all the constant values as a function of $\omega$: $A = (Ne^2)/(m\varepsilon_0 V)$ . This means that besides having a real part, $\chi(\omega)$ has an imaginary part which corresponds to the delayed response of the dipole to the field. The permittivity of the medium is correlated to the susceptibility by:

$$\varepsilon(\omega) = 1 + \chi(\omega) \tag{2.7}$$

which by substituting in (2.6) will give:

$$\varepsilon(\omega) = 1 + \frac{A}{(\omega_0^2 - \omega^2 - i\omega\gamma)} \tag{2.8}$$

Now let us consider the simplified energy-momentum dispersion relation of a transverse EM wave inside a FP cavity or propagating at a metal-dielectric interface[44] (which is the case in our experiments) as follows:

$$k = \frac{\omega}{c}\sqrt{\varepsilon(\omega)} \tag{2.9}$$

For simplicity, let's denote $\kappa = kc$ (where $c$ is the speed of light in vacuum), then the new term for the momentum $\kappa$ is expressed as:

$$\kappa^2 = \omega^2\varepsilon(\omega) = \omega^2(1 + \frac{A}{\omega_0^2 - \omega^2 - i\omega\gamma}) \tag{2.10}$$

By applying simple algebraic rearrangements, equation (2.10) can be also written as:

$$\kappa^2 - \omega^2 = \frac{A}{\omega_0^2 - \omega^2 - i\omega\gamma} \tag{2.11}$$

$$(\kappa - \omega)(\kappa + \omega) = \frac{A}{(\omega_0 - \omega)(\omega_0 + \omega) - i\omega\gamma} \tag{2.12}$$

The presence of $\omega$ in the damping term $i\omega\gamma$ of equation (2.10) causes a term of the third order, which is difficult to solve in closed form, unlike the case when the damping term $\gamma$ is 0.[41] By applying the approximations $(\kappa - \omega) \sim 2\omega_0$ and $(\omega_0 + \omega) \sim 2\omega_0$, the expression above can be derived as:

$$2\omega_0(\kappa - \omega) = \frac{A}{2\omega_0(\omega_0 - \omega) - i\omega\gamma} \tag{2.13}$$

In the case where the frequency of the field is close to that of the dipole (i.e. $\omega \simeq \omega_0$), equation (2.13) becomes:

$$(\kappa - \omega)(\omega_0 - \omega - i\,\gamma/2) = \frac{A}{4} \tag{2.14}$$

which is the dispersion relation for the coupling of a material dipole with an EM-field wave. This equation has two solutions:

$$\omega_{\pm} = \frac{\kappa}{2} + \frac{\omega_0}{2} - i\frac{\gamma}{4} \pm \frac{1}{2}\sqrt{A + (\kappa - \omega_0 + i\frac{\gamma}{2})^2} \tag{2.15}$$

The two solutions $\omega_+$ and $\omega_-$ are called the normal modes of the system. At resonance, $\kappa = \omega_0$ and therefore:

$$\omega_{\pm} = \omega_0 - i\frac{\gamma}{4} \pm \frac{1}{2}\sqrt{A - \frac{\gamma^2}{4}} \tag{2.16}$$

It is clear that the dissipation in the optical mode is absent in our derivation[41]. In order to account for the losses in the optical mode, we replace $\kappa$ by $\kappa - \gamma_{OM}/2$ and equation (2.16) becomes:

$$\omega_{\pm} = \omega_0 - i\frac{\gamma}{4} - \frac{\gamma_{OM}}{4} \pm \frac{1}{2}\sqrt{A - (\frac{\gamma}{4} - \frac{\gamma_{OM}}{4})^2} \tag{2.17}$$

Equation (2.17) clearly shows that dissipation from both the dipole oscillator and the EM mode are present in the new normal modes $\omega_{\pm}$. The energy difference between the normal modes $(\omega_+ - \omega_-)$ determines the Rabi splitting (or Rabi frequency) $\Omega_R$, and consequently the strong coupling condition can be written as:

$$\Omega_R = \sqrt{A - (\frac{\gamma}{4} - \frac{\gamma_{OM}}{4})^2} \tag{2.18}$$

The Equation in (2.18) shows that $\Omega_R$ requires the condition that $A > (\frac{\gamma}{4} - \frac{\gamma_{OM}}{4})^2$ and it is maximum when $\gamma_{OM} \sim \gamma$. If we neglect the damping forces, the Rabi frequency is expressed as:

$$\Omega_R = \sqrt{A} = \sqrt{\frac{N}{V}} \frac{e}{\sqrt{m\varepsilon_0}} \tag{2.19}$$

Equation (2.19) shows a direct correlation between the Rabi splitting and the concentration $C$ of coupled molecules since $\sqrt{C} = \sqrt{N/V}$. This correlation will be experimentally observed in chapter 5.

The exact solutions of the dispersion relation obtained in (2.10) are represented in Figure 2.1. The dispersions of the normal modes $\omega_{\pm}$ are displayed by assuming that there are no losses in the system (i.e. $\gamma_{OM} = \gamma = 0$) and that the constant $A$ represents a small fraction of $\omega_0^2$. The graph takes into account only a small range of values of the wavenumber $\kappa$ around the bare dipole frequency $\omega_0$. At larger detunings, the normal modes disperse asymptotically with the original dipole transition frequency and that of the photonic mode (dashed lines in Figure 2.1). However, as the system approaches resonance the curves spread away from the original dispersions and the energy gap between the normal modes increases in a behavior referred as the anti-crossing. At resonance (i.e. $\omega/\omega_0 = \kappa/\omega_0 = 1$), the energy splitting is at its maximum, and the value at maximum energy splitting is called the Rabi splitting (or Rabi frequency) as we have mentioned earlier. Experimentally speaking, the presence of the anti-crossing behavior in our dispersion relations is a typical proof that the system is in the strong coupling regime and is associated with hybrid character of the modes. These hybrid modes have become the topic of interest for many researches including our work in this thesis.

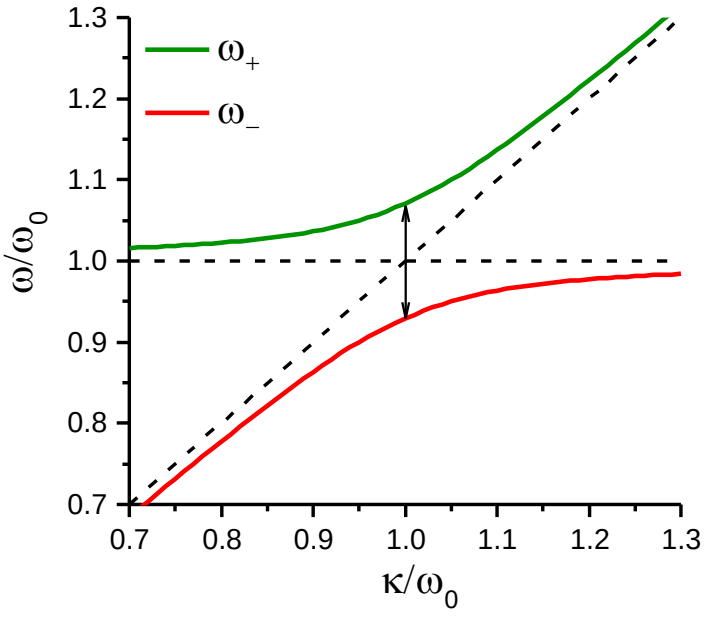



**Figure 2.1:** Normal modes dispersion of the coupled system as a function of the optical mode tuning, showing the anti-crossing behavior of energy at resonance with a Rabi splitting $\Omega_R = 0.14\omega_0$. The calculation neglects the dissipations of the coupled system. The horizontal and sloped dotted lines display the energy of the matter and dispersion of optical modes respectively in the absence of coupling.

## 2.1.1- Numerical Applications

The quantitative description in the above section is appropriate for a single dipole (for instance an atom) interacting with a field mode. The situation is different in our experiments, because matter here is an ensemble of organic molecules embedded in a polymer matrix or mixed in a solution. For this reason, the line-shapes are far more complicated than those present in single dipole due to the molecule's inhomogeneous broadening and vibrational manifolds.[43,59,88] For this reason, we simulate our systems via numerical method namely the Transfer or T-matrix formalism for multi-layer systems. This formalism is an equation that relates the EM field input with its output through a matrix which accounts for the boundary conditions of the field at each interface. We use plane waves as an exact solution to the Maxwell's equations and assume that each layer can be described by a uniform index of refractions. The optical response of the active layer

(embedded molecules) includes the material's contribution to the refractive index $n$ which is a complex number having the real part $n'$ and an imaginary part $n''$. The latter part is known as the extinction index and can be obtained from the absorption spectrum $a(\omega)$ through the following relation:

$$a(\omega) = \frac{\omega}{c} n'' \tag{2.20}$$

Then by using Kramers-Kronig[91] relations, one can obtain the value of the real index $n'$:

$$n' = 1 + \frac{2}{\pi} \wp \int_0^\infty \frac{\omega' n''(\omega')}{\omega'^2 - \omega^2} d\omega' \tag{2.21}$$

where $\wp$ represents the principle value. Consequently, the real and imaginary parts of the permittivity ($\varepsilon'$ and $\varepsilon''$) can be calculated using the following relations:

$$\varepsilon' = n'^2 - n''^2 \tag{2.22}$$

$$\varepsilon'' = 2n'n'' \tag{2.23}$$

Both real and imaginary parts of the index depend on the energy $\omega$ (see Fig. 2.2a and b). The absorption has a maximum value at the energy $\omega_0$(Fig. 2.2a). The variation of the real index $n'$ can be analyzed according to the relative value of the energy values with respect to the absorption peak (Figure 2.2b). Far from $\omega_0$, $n'$ is very close to the background index (which is 1.41 in this case) either from above (for $\omega < \omega_0$) or below (for $\omega > \omega_0$). As the energy approaches resonance, $n'$ increases in a behavior similar to the "normal" dispersion. However, it drops suddenly at energies very close to resonance resulting in a peak and dip around $\omega_0$.

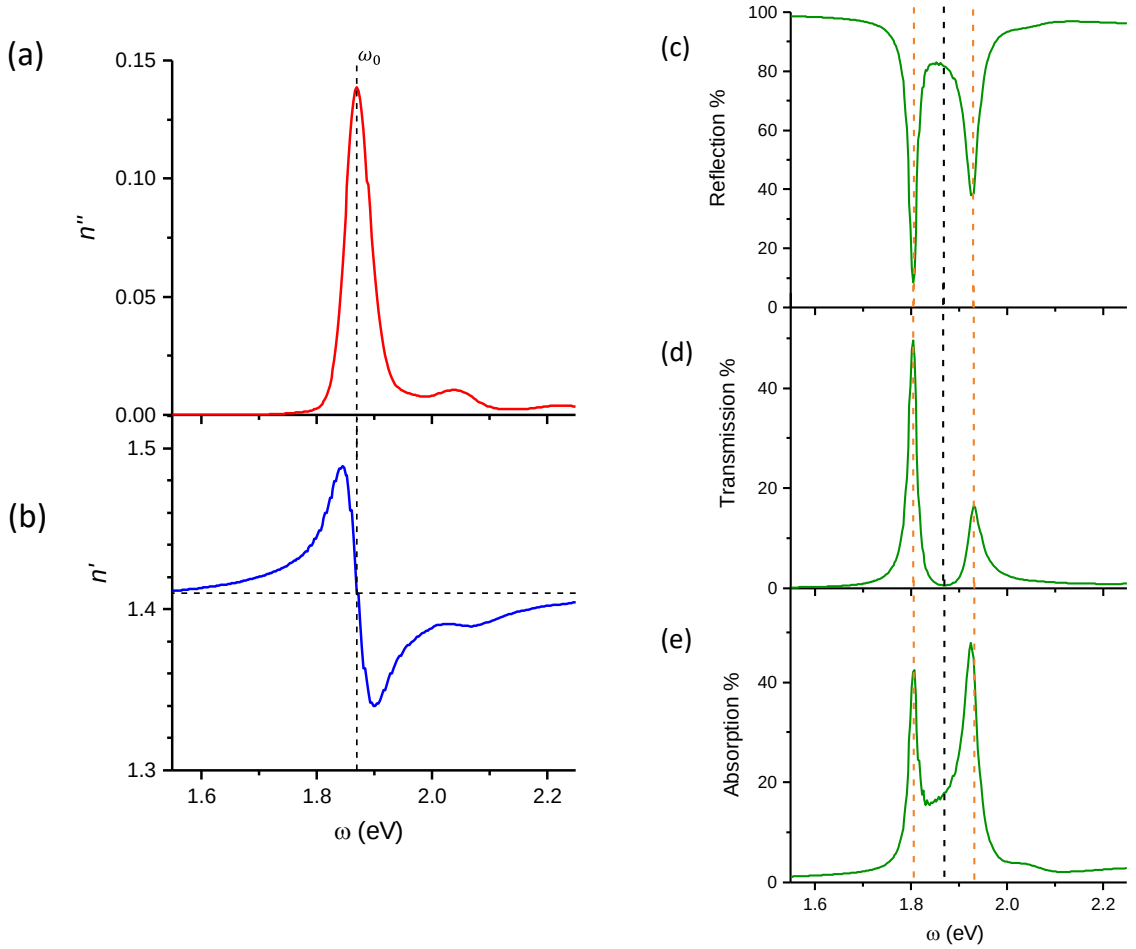



**Figure 2.2:** The real (a) and imaginary (b) part of the refractive index of Chlorin e6 (Ce6) dissolved in dimethylformamide (DMF). The vertical line shows the resonant frequency $\omega_0$ of this molecule and the horizontal line in (b) corresponds to the background refractive index. Figures (c), (d) and (e) are the calculated reflection (R%), transmission (T%) and absorption (A%=1- T%- R%) spectra respectively of the coupled system, demonstrating that the original resonant mode (the middle black dotted line) splits into two new normal modes (the orange dotted lines) when a 420 nm active layer is placed in a resonant cavity formed by two 30 nm thick Ag mirrors.

When the system is placed into a resonant cavity, the peak and dip of the real index will produce two normal modes with opposite phases. Experimentally, these normal modes appear as two distinct peaks under spectroscopic observation. However, by making use of the T-matrix formalism, we can predict the transmission, reflection, and absorption spectra of a sample molecule placed in a resonant cavity. The spectra show the presence two peaks

representing the normal modes under strong interaction with the cavity mode (the orange dotted lines in Figures 2.2 c, d, and e). As we will see in Chapter 4, similar numerical methods using the T-matrix were used to calculate the absorption of molecules when placed in liquid Fabry-Perot (FP) nanocavities.

# 2.2- Quantum Description

## 2.2.1- Single Two-level System

In order to study the light-matter coupling from the quantum point of view, we begin by considering the emitter as a single two-level system interacting with a quantized electromagnetic field (see Figure 2.3).

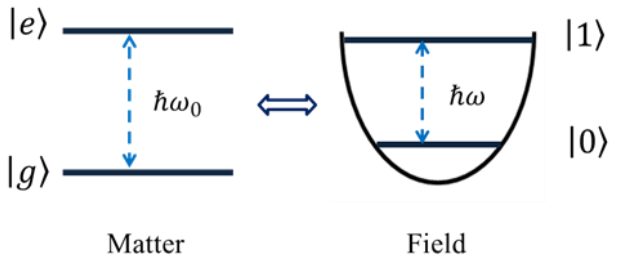



**Figure 2.3:** A two-level system coupled to a single field mode treated as a harmonic oscillator.

The quantum emitter is modeled as a spin-1/2 dipole whose magnetic field is aligned with the quantization axis z, having an upper level $|e\rangle$ and a lower level $|g\rangle$ connected by the transition angular frequency $\omega_0$. In the basis of the spin along z, we define the following spin-flip operators:

$$\sigma_+ = |g\rangle\langle e| \qquad \sigma_- = |e\rangle\langle g| \qquad \sigma_z = |e\rangle\langle e| - |g\rangle\langle g| \tag{2.24}$$

On the other hand, the EM field is taken as a quantized harmonic oscillator with frequency $\omega$, and we denote by $a$ and $a^\dagger$ the bosonic creation and annihilation operators respectively. If we denote the Hamiltonian of the spin-flip by $\mathcal{H}_a$ , that of the optical mode by $\mathcal{H}_b$ and the interaction term by $\mathcal{H}_{ab}$ , the general form of the Hamiltonian $\mathcal{H}$ of the system is expressed as:

$$\mathcal{H} = \mathcal{H}_a + \mathcal{H}_b + \mathcal{H}_{ab} \tag{2.25}$$

The interaction term $\mathcal{H}_{ab}$ is defined by the product of the transition dipole operator $\boldsymbol{\mathcal{D}}$ by the electric field operator $\boldsymbol{\mathcal{E}}$ , which will usually bring about 4 terms. Two terms accounting for the normal absorption/emission of a photon associated with a transition to the upper/lower states, and two terms for the anti-resonant processes during which the annihilation/creation of a photon is accompanied by a transitions to the lower/upper states. Using the rotating wave approximation (RWA), we neglect the anti-resonant processes leaving $\mathcal{H}_{ab}$ with only two terms. In this case, the total Hamiltonian of the system is called the Jaynes-Cumming Hamiltonian, and is expressed in terms of the defined operators as:

$$\mathcal{H} = \frac{\hbar}{2}\,\omega_0\sigma_z + \frac{\hbar}{2}\omega a^\dagger a - i\frac{\hbar}{2}\Omega_R[a\sigma_+ - a^\dagger\sigma_-] \tag{2.26}$$

The factor $\Omega_R$ which accounts for all the constant values resulting from the operators' product $-\boldsymbol{\mathcal{D}}.\boldsymbol{\mathcal{E}}$ measures the coupling strength. $\Omega_R$ is called the Rabi frequency and is expressed as follows:

$$\Omega_R = \frac{2d}{\hbar}\xi_0 \tag{2.27}$$

$$\xi_0 = \sqrt{\frac{\hbar\omega}{2\varepsilon_0 V}} \tag{2.28}$$

where *d* is the transition dipole moment of matter and $\xi_0$ is the electric field amplitude per photon in the mode volume *V*. In the general case when the two-level system interacts with $n$ photons, the eigenvectors of the system will be a set of: $|e,n\rangle$ and $|g,n+1\rangle$, and the coupling term will be expressed as:

$$\Omega_{R,n} = \frac{2d}{\hbar}\xi_0\sqrt{n+1} \tag{2.29}$$

Here it is interesting to note that in the absence of photons ($n = 0$); the Rabi splitting sustains a finite value. This is due to the interaction of the dipoles with the zero point energy fluctuations of the confined field. In this case, the regime is referred as the Vacuum Rabi splitting and it is the condition present in all the experiments in this thesis.

Now in order to determine the eigenvalues of our system, we restrict our conditions to the case of a dipole interaction with only a single photon mode. Keeping in mind the Janes-Cumming coupling terms, we introduce the eigenvectors of the dipole-field system: $|e,0\rangle$ and $|g,1\rangle$. Let $\Delta = \omega - \omega_0$ be the dipole-field detuning constant. Therefore, the new form of equation (2.26) is expressed as:

$$\mathcal{H} = \frac{\hbar}{2}(\omega+\omega_0).\mathbb{I} + \frac{1}{2}\begin{pmatrix}\Delta & -i\Omega_R \\ i\Omega_R & -\Delta\end{pmatrix} \tag{2.30}$$

and $\mathbb{I} = \begin{pmatrix}1 & 0\\ 0 & 1\end{pmatrix}$ is the well-known unitary matrix. The diagonalization of (2.30) will result in the energy eigenvalues expressed as follows:

$$E_{\pm} = \frac{\hbar}{2}(\omega+\omega_0) \pm \frac{1}{2}\sqrt{\Delta^2+\Omega_R^2} \tag{2.31}$$

In analogy with the classical description, the general form of the energy eigenvalues in (2.31) is similar to the normal modes of equation (2.15) obtained in the previous section. Plotting the dispersion of the energies in equation (2.31) will result in a similar anti-

crossing behavior as that present in Fig. 2.1. Nevertheless, we can also deduce from the previous diagonalization the following eigenstates:

$$|P^{+}\rangle = \cos\left(\frac{\theta}{2}\right)|e,0\rangle + i\sin\left(\frac{\theta}{2}\right)|g,1\rangle \tag{2.32}$$

$$|P^{-}\rangle = \sin\left(\frac{\theta}{2}\right)|e,0\rangle - i\cos\left(\frac{\theta}{2}\right)|g,1\rangle \tag{2.33}$$

$|P^{+}\rangle$ and $|P^{-}\rangle$ known as the polaritonic states, were expressed as a function of $\theta$ which is the angle that the field makes with the z quantization axis and it is defined by:

$$\tan\theta = \frac{\Omega_R}{\Delta} \tag{2.34}$$

At resonance, $\theta = \pi/2$ and the two polaritonic states become:

$$|P_{res}^{+}\rangle = \frac{1}{\sqrt{2}}(|e,0\rangle + i|g,1\rangle) \tag{2.35}$$

$$|P_{res}^{-}\rangle = \frac{1}{\sqrt{2}}(|e,0\rangle - i|g,1\rangle) \tag{2.36}$$

In this sense, the polaritonic states represent a coherent superposition of an excited state with no photon and a ground state with one photon. Therefore, we were able to mathematically show how the polaritonic states arising from the strong light-matter interaction inherit fermionic and bosonic characteristics from their constituents. Moreover, the separation between these states is assigned to the reversible energy exchanged between the matter and light mode.

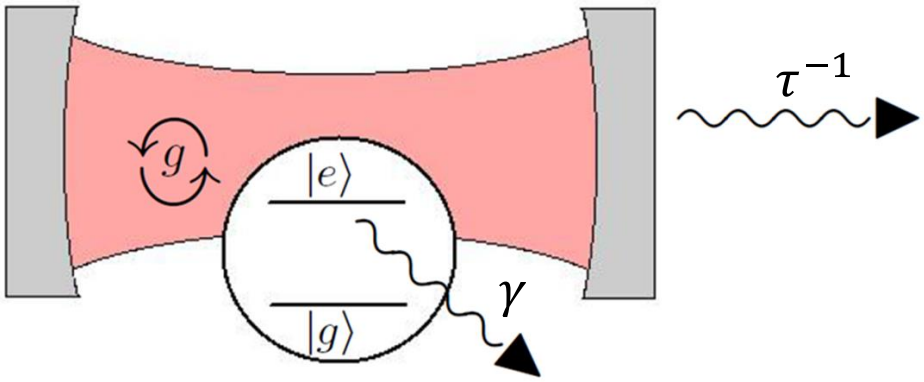



**Figure 2.4:** A two-level system coupled Rabi oscillation. An excited dipole is placed into a cavity and undergoes vacuum Rabi oscillations mediated by the matter-field coupling strength $g = \Omega_R/2$, resulting in one quantum being added to the mode. Dissipation mechanisms are also illustrated although not discussed in the main text. $\gamma$ is the atomic damping rate and τ is the cavity lifetime. Figure is adapted from reference.[92]

The time-evolution of the states will help studying the energy exchange mechanism between the interacting species. Let us consider a dipole in the ground state interacting with a trapped photon in its environment. The time-evolution of such system is given by:

$$|\Psi(t)\rangle = \cos\left(\frac{\Omega_R t}{2}\right)|e,0\rangle - i\sin\left(\frac{\Omega_R t}{2}\right)|g,1\rangle \tag{2.37}$$

The system is constantly oscillating between the lower and higher states and consequently performing the so-called "Rabi oscillations" (see Figure 2.4). This is a typical description for the case of a molecule placed inside a resonant cavity. The photon emitted by the relaxed molecule is trapped and reabsorbed maintaining the Rabi oscillations. Moreover, we can obtain the probability $P_r$ for finding the system in state $|g,1\rangle$ by:

$$P_r = \cos^2\left(\frac{\Omega_R t}{2}\right) = \frac{1+\cos\Omega_R t}{2} \tag{2.38}$$

## 2.2.2- Collective Rabi Splitting:

The quantum description explained above suffices to understand the origin of the Rabi oscillations arising from reversible matter-field energy exchange at the level of a single two-level system. Moreover, it was able to quantitatively expose the origins of the new states $|P^+\rangle$ and $|P^-\rangle$ arising from this coupling. On the other hand, when dealing with an ensemble of N two-level systems interacting with a confined mode (which is the case of our experiments in this thesis), a many-body approach accounting for such ensemble is required. For this reason, we adapt the so-called Dicke[93–95] or Tavis-Cummings[96] Hamiltonian which is given by:

$$\mathcal{H}^N \approx \hbar\omega_0\left(-\frac{N}{2}+b^\dagger b\right)+\hbar\omega a^\dagger a - i\frac{\sqrt{N}\hbar\Omega_R}{2}(a^\dagger b - a b^\dagger) \tag{2.39}$$

The system is here is treated as a giant quantum oscillator having an effective transition dipole moment $\sqrt{N}d$. The new bosonic operator $b$ represents a mapping of the spin-systems to bosonic systems[41]. We associate $|G,1\rangle$ and $|D,0\rangle$ to the ground and excited states of the N-emitters system respectively, where the excitation is evenly distributed over the N identical molecules (so-called Dicke's states). Their expression is given by:

$$|G,1\rangle = |(g,g,g,\dots),1\rangle \tag{2.40}$$

$$|D,0\rangle = \frac{1}{\sqrt{N}}\sum_{i=1}^{N}|(g,g,\dots e_i,\dots g),0\rangle \tag{2.41}$$

By using the above expressions and solving for the eigenstates of $\mathcal{H}^N$, in the absence of other photons interacting with the system, one can get the expression of the vacuum Rabi splitting:

$$\hbar\Omega_R = 2\sqrt{N}d\xi_0 \tag{2.42}$$

It can be noticed that the collective Rabi splitting increases as a function of the number of coupled emitters. Thus, we have so far validated this relationship by two distinct

quantitative approaches (classical and quantum). We will also observe experimentally (in Chapter 4) how this relationship has played the role for bringing our system from the weak to the strong coupling regime. Moreover, we have considered the case where $n$ photons interfere in the energy exchange process and consequently showed that the Rabi splitting has a finite value even in the absence of photons. All the experiments present in this thesis are performed in the vacuum Rabi splitting conditions.

# Part II.

# Results

# CHAPTER 3:
# Strong Coupling on Plasmonic Structures

In this chapter we investigate the strong coupling between surface plasmon polaritons (SPPs) and organic molecules. An introduction to SPPs including its origins, dispersion relation, and other properties are provided, followed by the basics of organic molecules strong coupling with surface plasmon resonances. Experimental observation for the molecule strong coupling with SPPs is presented in parallel with the methods and procedures. Consequently, changes of surface properties under the coupling of a cyanine dye with SPPs are investigated by studying its wetting properties. Contact angle measurements are performed for the detection of such modifications, and discussed in order to highlight the challenges of this experiment.

## 3.1- Surface Plasmon Polaritons

In metals, one can image the electrons of the conduction band as a sea inside which the "fixed" nuclei or core atoms constituting the metallic bulk are immersed. On the surface of a metal, the electrons are exposed to the interfacial dissymmetry unlike those in the bulk.[97] These surface electrons can undergo collective oscillations and experience EM excitations called surface plasmon polaritons (SPPs). Hence SPPs are a mixture of EM waves and surface charge oscillations (Figure 3.1a). SPPs can be confined in subwavelength volumes, a feature that favors strong coupling effects.[98,99]

The EM waves of SPPs are transverse magnetic (TM) modes in character, since the electric field *E* and magnetic field *H* respectively within or perpendicularly to the plane of incidence of light at the metal-dielectric interface, as illustrated in Figure 3.1a. The mixed character of SPPs leads to the dispersion of the electric field confined at the interface, and to an electric field in the *z* direction, which is maximum at the surface ($z$ =0) and decreases exponentially into the dielectric (metal) as *z* increases positively (negatively) as shown in Figure 3.1b. The field in this case is said to be evanescent in z, and further explanation about such evanescence behavior is discussed in later paragraphs.

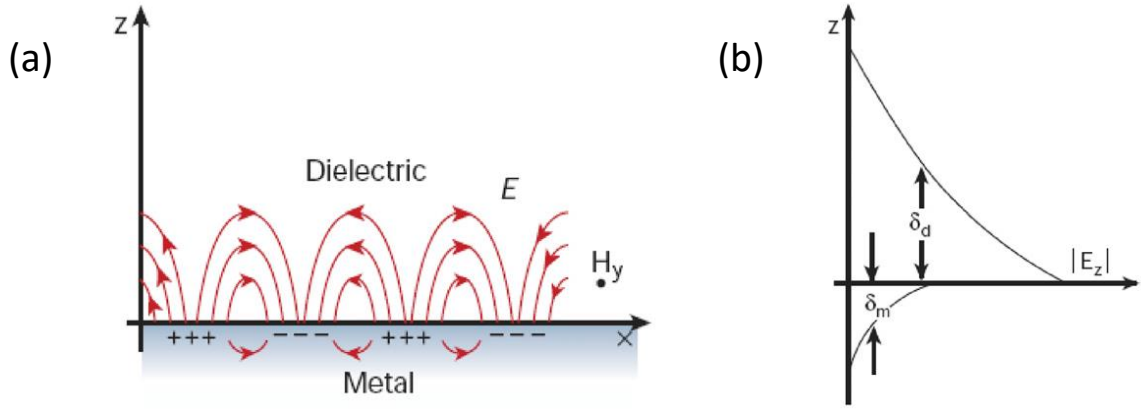



**Figure 3.1:** (a) Schematic illustration of electromagnetic wave and surface charges at the metal-dielectric interface. (b) The electric field evanescence along the z-axis and its corresponding penetration depth into the dielectric *($\delta_d$)* and metal *($\delta_m$)* respectively.

The electric field due the surface plasmons $E_{SP}$ is given by the following equation:

$$E_{SP} = E_0^{\pm} exp[i(k_x.x \pm k_z.z - \omega t)] \quad (3.1)$$

where $E_0^{\pm}$ is the magnitude of the electric field in the positive (+) and negative (-) directions along the z-axis respectively. $k_x$ and $k_z$ represent the complex wave vectors of the field in the $x$ and $z$ directions respectively, and $\omega$ is the frequency of plasma oscillations. By inserting the equation (3.1) into Maxwell's equations, one can obtain the dispersion relation of SPPs, which is discussed next.

### 3.1.1- Dispersion of SPPs

The mixed character of the SPPs results in the dispersion of the confined electric field at the metal-dielectric interface. The momentum of the surface plasmon modes ($\hbar k_{SP}$) propagating along the interface ($k_{SP} = k_x$) is larger than that of the free-propagating light of the same frequency ($k_0 = 2\pi/\lambda$). This can be explained quantitatively by applying Maxwell's equations with the appropriate boundary conditions to equation (3.1) which eventually leads to the SPP dispersion relation[100] as follows:

$$k_{SP} = k_0 \sqrt{\frac{\varepsilon_d \varepsilon_m}{\varepsilon_d + \varepsilon_m}} \tag{3.2}$$

where $\varepsilon_d$ and $\varepsilon_m$ are the frequency dependent permittivity of the dielectric and the metal respectively. The quantitative relationship between the permittivity values will determine the dispersion.

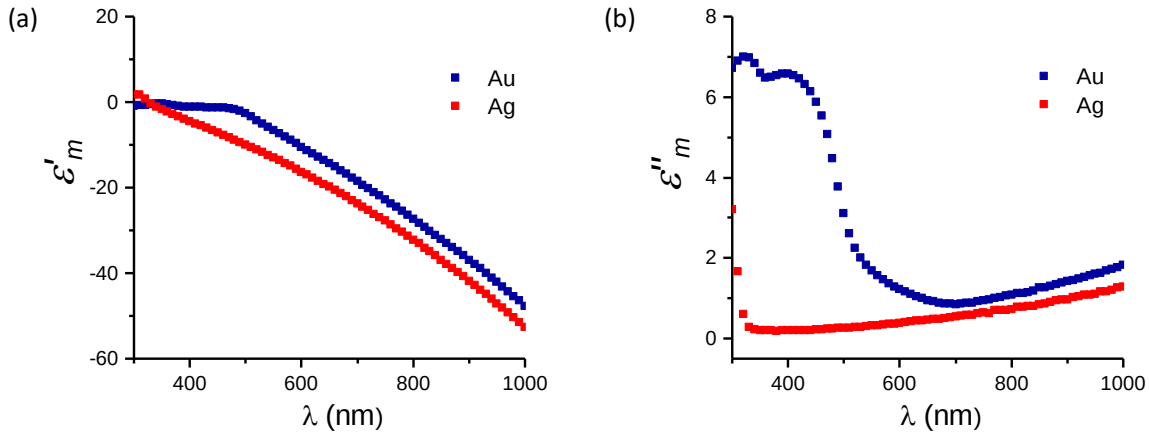



**Figure 3.2:** The real (a) and imaginary part (b) of the permittivity of silver (Ag) and gold (Au) as a function the wavelength $\lambda$. The values were calculated from the complex index of refraction taken from reference [101].[101]

For SPP excitations to be possible, the permittivity of the metal which is a complex number ($\varepsilon_m = \varepsilon'_m + i\varepsilon''_m$) should have a negative real part ($\varepsilon'_m$) with magnitude larger than that of the dielectric material at the interface which is real and positive in most cases.

This condition can be fulfilled by metals, for instance Au and Ag as shown in Figure 3.2a. The real part is negative for wavelengths above 400 nm and decreases rapidly starting from 500 nm. The imaginary part $\varepsilon''_m$ corresponds to the absorption (or dissipation) in the metal. From Figure 3.2b, it can be deduced that Ag is a better choice of metal for the generation of SPPs in the visible range between 400 nm and 600 nm, since it experiences less dissipation allowing for longer propagation of SPPs.

It also follows from equation (3.2) that the SPP dispersion curve exhibits a nonlinear characteristic. The dispersion of SPPs at an Ag-air interface in the energy range 1eV to 3.5 eV is shown in Figure 3.3 by substituting the permittivity data of Figure 3.2a into equation (3.2).

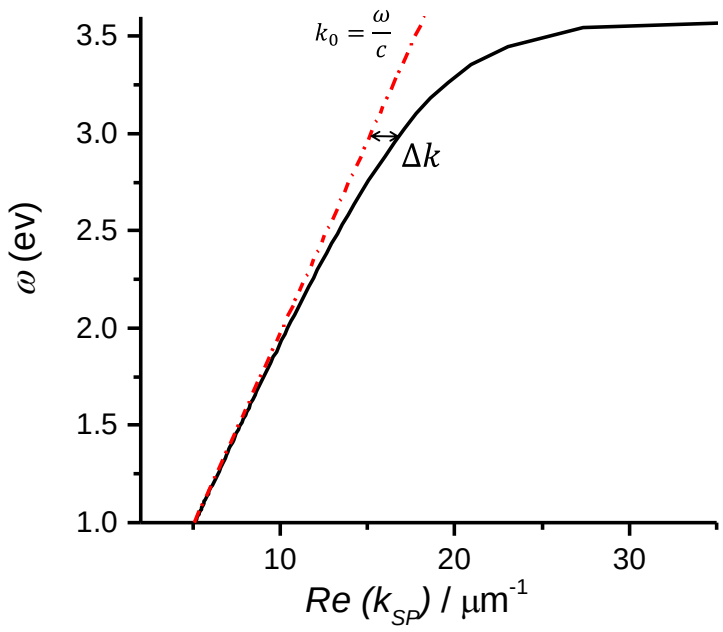



**Figure 3.3:** Comparison of the dispersion curves of SPPs at an Ag-air interface (solid black curve) with that of freely propagating light in the dielectric medium, in this case air (dash-dotted red curve).

At low energies, the dispersion curve of the SPPs is asymptotic to that of freely propagating light (the red dash-dotted line in Figure 3.3), at these energies the SPPs resemble grazing surface waves and are weakly bound to the interface. At higher energies,

SPPs have higher momentum than that of the feely propagating EM waves ($k_{SP} > k_0$) at the same energy (Figure 3.3). This increase in momentum is associated with the strong binding of the SPPs to the surface. The resulting momentum mismatch ($\Delta k$) must be compensated when generating SPPs by light or vice-versa. This can be experimentally achieved by using different methods as will be discussed in later paragraphs.

## 3.1.2- The Evanescent Field of SPPs

In contrast to the propagating nature of SPPs along the surface, the interaction between the surface charges and the electromagnetic field leads to an evanescent field in the plane normal to the metal-dielectric interface which decays exponentially into each of the metal and dielectric media as presented in Figure 3.1b.

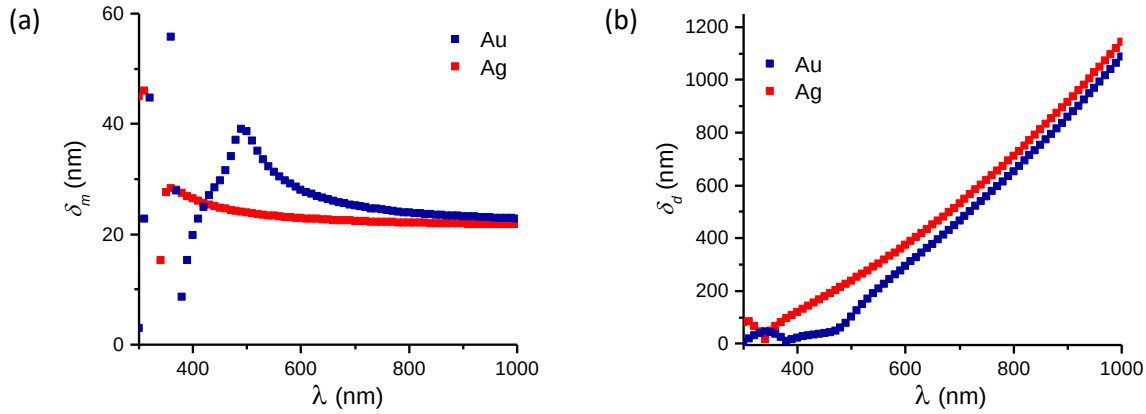



**Figure 3.4:** The spatial extension of SPPs into the metal $\delta_m$ (a) and dielectric $\delta_d$ (b) media as calculated from equation (3.3) for Au-air and Ag-air interfaces.

Due to the fact that $k_{SP} > k_0\sqrt{\varepsilon_{m,d}}$, the wave vector of the normal evanescent field $k_z^{m,d} = \sqrt{\varepsilon_{m,d}(k_0)^2 - (k_{SP})^2}$ is imaginary. In this case, the penetration depths in the dielectric ($\delta_d$) and the metal ($\delta_m$) (a.k.a. skin depth) are defined by:

$$\delta_{m,d} = \frac{1}{\left|k_z^{m,d}\right|} \tag{3.3}$$

at which the electric fields fall to 1/e. Equations from (3.3) are expressed as a function of the metal and dielectric permittivity as follows:[102]

$$\delta_m = \frac{\lambda}{2\pi}\left|\frac{\varepsilon_d + \varepsilon_m}{\varepsilon_m'^2}\right|^{1/2} \tag{3.4}$$

$$\delta_d = \frac{\lambda}{2\pi}\left|\frac{\varepsilon_d + \varepsilon'_m}{\varepsilon_d^2}\right|^{1/2} \tag{3.5}$$

The values from Figure 3.2a were used in equations (3.4) and (3.5) in order to calculate the skin depth of the normal field inside the metal (Figure 3.4a) and dielectric (Figure 3.4b) at each of the Au-air and Ag-air interface. It is obvious that the evanescent field has higher penetration depth in the semi-infinite dielectric medium than that of the metal, and this is due to the screening effect caused by the free charges in the metal. Nevertheless, in the dielectric, the normal fields are concentrated in small volumes at the surface of metal with values for 1/e on in the order of $\lambda/2$ in the visible spectrum.

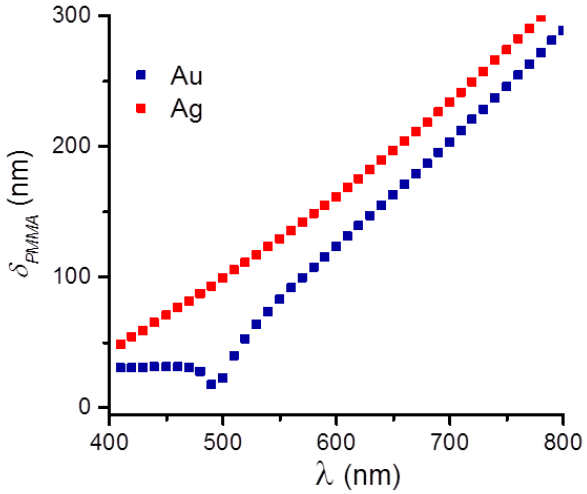



**Figure 3.5:** The penetration depth of SPPs normal field in PMMA at Au-PMMA (blue) and Ag-PMMA (red) interfaces.

To illustrate this point, Figure 3.5 shows the depth of the field inside a polymer matrix Poly (methyl methacrylate), PMMA, the dielectric medium at the surface of Au and Ag. As can be seen from Figure 3.5, the skin depth of the field at wavelengths between 550 nm and 600 nm is about 120 nm in Ag, and 100 nm in Au. These data correspond to the experiment that will be discussed below in this chapter. In addition, it is clear that the confined normal fields of SPPs provide a suitable environment for the observation of strong light-molecule coupling.

## 3.1.3- The Excitation of SPPs

According to the dispersion relation given by equation (3.2), the momenta of SPPs exceed that of freely propagating waves resulting in a momentum mismatch. The excitation of SPPs requires conservation of momentum and can be achieved by compensation for the missing momentum. There are several techniques to excite SPPs, such as Otto or Kretschman-Raether prism coupling,[103] leakage radiation spectroscopy,[98,104] scattering from a defect on the surface such as a subwavelength hole or slit,[99–101,103,104] and periodic corrugations on the surface of metals.[105,106] The latter is also referred as diffraction grating, and it is the technique we adapt in this thesis for the excitation of SPPs.

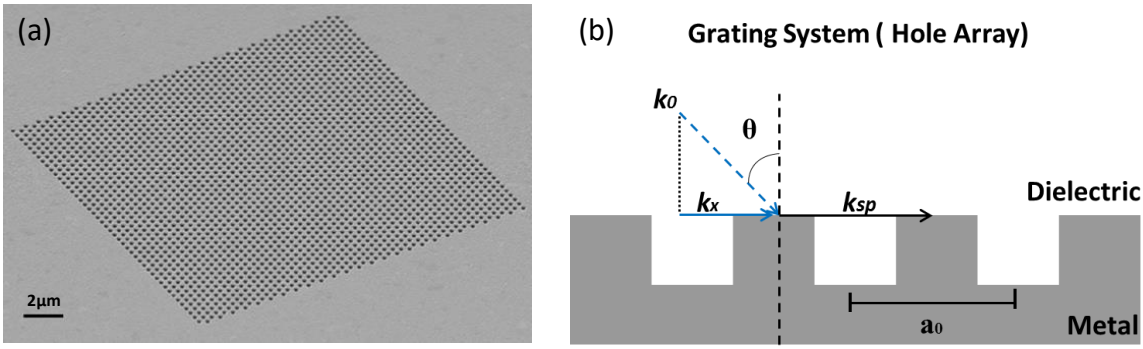



**Figure 3.6:** (a) SEM image of a hexagonal hole-array with periodicity $a_0 = 440$ nm and hole diameter $D$ = 200 nm milled in $t$ = 200 nm thick Ag film. (b) Schematic representation of $k_{SP}$ the grating system of periodicity $a_0$, showing the propagation wavevector of SPPs ($k_{SP}$) generated by the horizontal component of the incident beam $k_x$ .

The diffraction grating that we use to excite SPPs is formed by milling a periodic subwavelength array of cylindrical subwavelength holes through a metallic film (Figure 3.6a). SPPs are then generated when their momentum matches the momentum of the incident photon via Bragg's scattering according to the following equation:

$$|k_{SP}| = \left|k_x + iG_x + jG_y\right| \tag{3.5}$$

where $k_{SP}$ is the surface plasmon wavevector, $k_x = (2\pi/\lambda)sin\theta$ is the component of the incident photon's wavevector in the plane of the grating such that $\theta$ is the angle of incidence (see Figure 3.6b). $G_x$ and $G_y$ ($G_x = G_y = 2\pi/a_0$) are the reciprocal lattice vector for a square array with periodicity $a_0$. The scattering order of the SPP modes is denoted by (*i*, *j*) where *i* and *j* are integers.

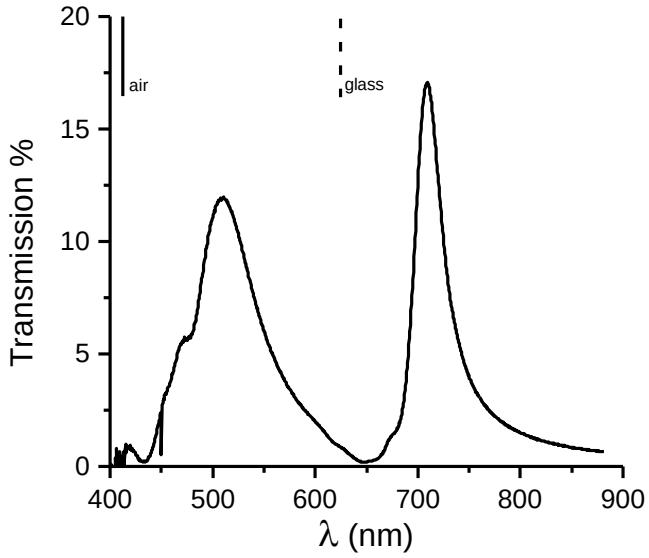



**Figure 3.7:** Zero-order transmission spectra of hole-array (square periodicity) at normal incidence. The array is milled on Ag film with periodicity 500 nm. The vertical solid and dashed lines correspond to the theoretical (1, 0) SP resonances at the air-metal and glass-metal interfaces respectively (see text).

It is interesting to note that the extraordinary optical transmission through holes having lateral dimensions less than half the wavelength of the incident beam exploits this

momentum matching mechanism.[107] This enhanced transmission results from the coupling of the incident light with surface plasmon (SPP) modes, and is observed for specific wavelengths ($\lambda_{SP}$). At normal incidence, the relationship between the SPP modes and the hole-array periodicity is given by the following equation:

$$\lambda_{SP} = \frac{a_0}{C}\sqrt{\frac{\varepsilon_d \varepsilon_m}{\varepsilon_d + \varepsilon_m}} \tag{3.6}$$

where $C(i,j)$ is given by $\sqrt{\mathrm{i}^2 + \mathrm{j}^2}$ for square arrays and $\sqrt{\frac{4}{3}(\mathrm{i}^2 + \mathrm{j}^2 + \mathrm{ij})}$ for hexagonal arrays. The black curve in Figure 4.7c shows the transmission spectrum of a square hole-array at normal incidence. The array has a periodicity of 500 nm, a hole diameter *D* of 260 nm, and is milled through a 200 nm Ag film deposited on glass substrate (more details about sample preparation and data acquisition are explained in the experimental section later in this chapter). The higher and lower energy peaks correspond to the SPPs at the Ag-air and Ag-glass interfaces respectively. The predicted theoretical resonances of the (1, 0)a (air) and (1, 0)g (glass) modes (represented by the short vertical lines in Figure 3.7) are in fact at transmission minima and located at a shorter wavelength than the experimental peak. This is explained by Wood's anomaly[108] which occurs when a diffracted order becomes tangent to the plane of the grating.[109] Moreover, the peaks have a Fano-type profile shape, which in addition to their displacement are the result of an interference effect between the resonant (SPPs) contribution and the non-resonant continuum of directly transmitted light.[110]

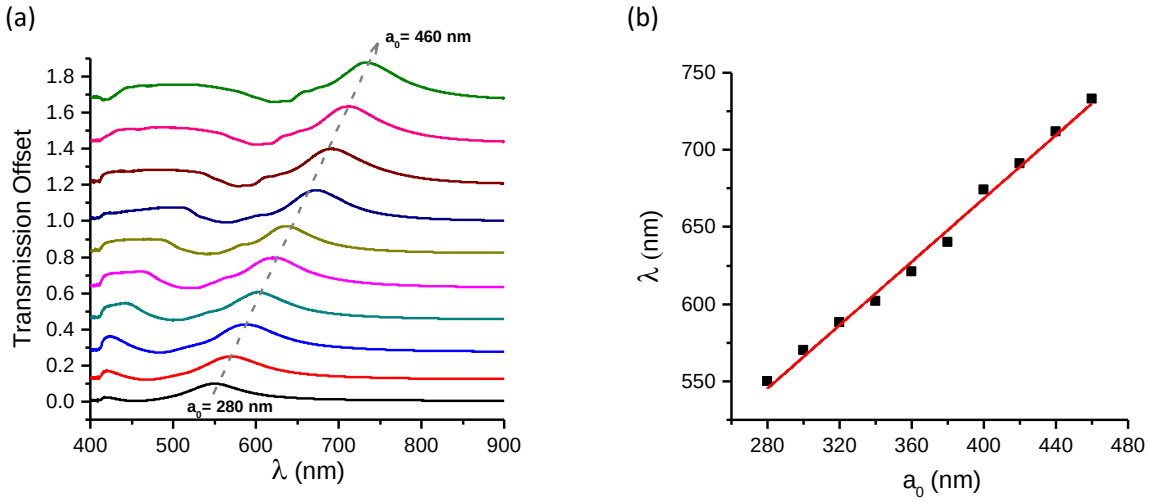



**Figure 3.8:** (a) The zero-order transmission spectra at normal incidence of hexagonal hole-arrays with varying periodicities ($a_0$) from 280 nm to 460 nm milled in Ag film. The grey dashed arrow marks the peaks of the (1, 0)g modes. (b) The wavelength of the (1, 0)g SPPs resonances as a function of the array periodicity. The red line is a linear fit.

It is clear from equation (3.6) that the transmission maxima of the arrays scale with the periodicity. Consequently, the plasmonic modes are periodic dispersive, and tuning these modes to a desired frequency can be achieved by modifying the array's periodicity as presented in Figure 3.8. A set of hexagonal hole-arrays, with increasing periodicities (by intervals of 20 nm), were milled through a 200 nm Ag film such that the diameter of all the holes is set to $a_0/2$. Their transmission spectra at normal incidence are presented in Figure 3.8a where the linear dependence of the (1, 0)g resonances with the periodicity is emphasized by the gray dashed arrow in Figure 3.8a, and linearly fitted by the red line in Figure 3.8b.

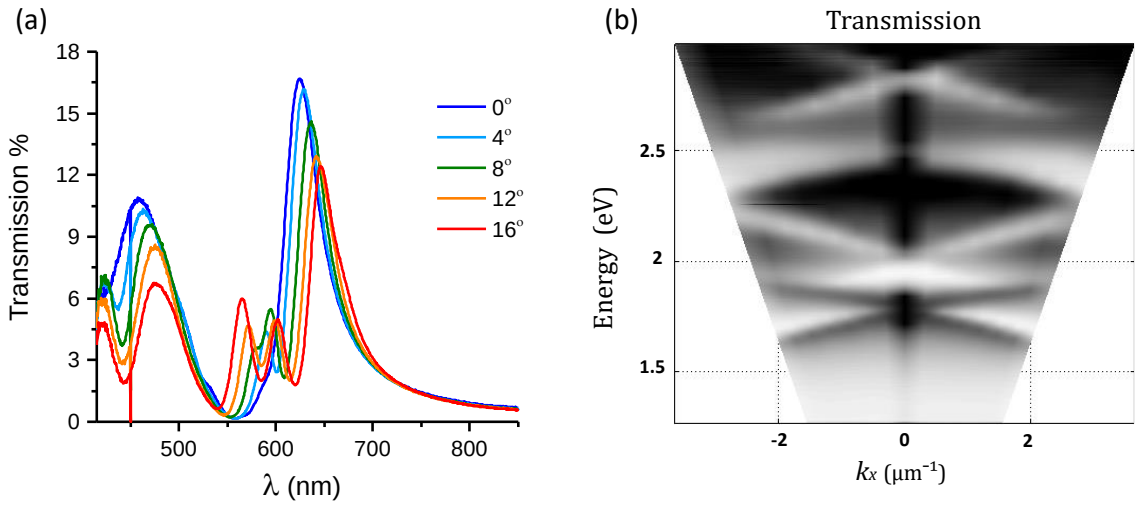



**Figure 3.9:** (a) The zero-order transmission spectra as a function of incident angle of the light in TM mode. Spectra were taken every 4° up to 16° for hexagonal array in Ag ($a_0$ = 400 nm, hole diameter = 205 nm, film thickness = 200 nm). (b) The energy-momentum dispersion of the same spectra present in (a) in addition to their symmetric values for negative angles. The bright lines represent peaks and dark ones represent dips.

The dispersion of the SPP modes can also be seen in the angular dependence of the spectra since $k_x = (2\pi/\lambda)sin\theta$. For example, the transmission spectra were taken for a hexagonal hole-array with periodicity 400 nm milled in Ag at varying angles from -16° to +16° with intervals of 4° (for clarity, only those from 0° to +16° are presented in Figure 3.9a). The spectra were taken using TM polarized light. The peaks shift to lower energy values (higher wavelength), change in intensity, and split into new peaks as the angle of incidence increases (see Figure 3.9a). The energy-momentum dispersion, presented in Figure 3.9b, was taken for all angles from -16° to +16°. The bright and dark areas represent peaks and dips respectively.

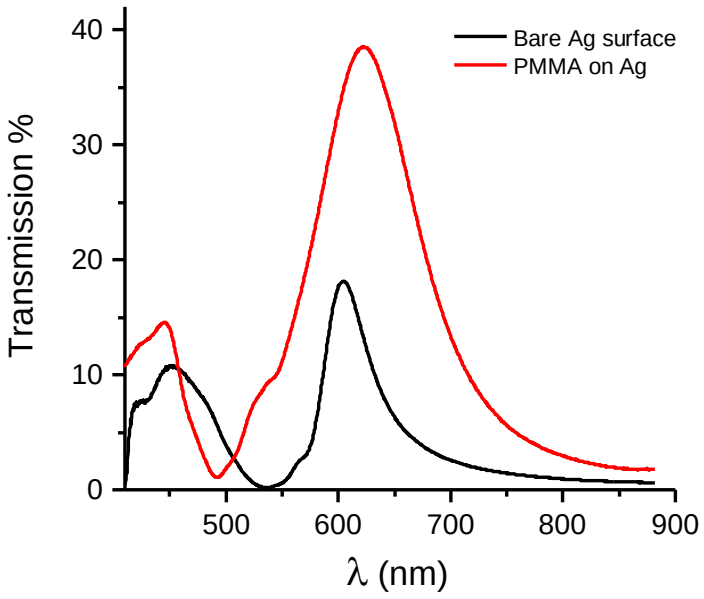



**Figure 3.10:** The zero-order transmission spectra at normal incidence for a hexagonal hole-array ($a_0$ = 380 nm) before (black curve) and after (red curve) the deposition of a 100 nm layer of PMMA on its surface.

Another consequence to the dispersion relation of SPPs (equation 3.6) is the dependence of their modes on the index of the dielectric medium. Figure 3.10 shows the transmission at normal incidence of a hexagonal array before and after the deposition of a PMMA. The 200 nm diameter holes were milled in 200 nm Ag film deposited on a glass substrate, with a lattice constant of 380 nm. The polymer is about 100 nm thick and has a refractive index of 1.49 in the visible range. The (1,0)g transmission peak is significantly boosted, and red shifted (by ca. 15 nm) upon the presence of the coated PMMA layer. This is explained by the fact that the index of refraction at both surfaces of Ag is matched.[111] The sensitivity of the SPP field to the index of refraction of the dielectric medium at the interface illustrates the potential of such arrays in functioning as sensing nano-devices.

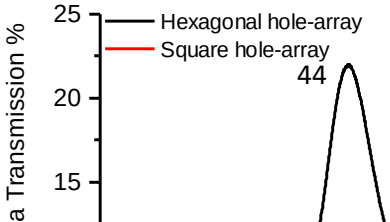


**Figure 3.11:** The normal incidence transmission spectra of hexagonal hole-array with $a_0$ = 440 nm (black curve) and square hole-array with $a_0$ = 380 nm (red curve). The diameter of holes in both cases is 140 nm. The hole-arrays are milled in 200 nm thick silver film.

It can be noticed from equation (3.6) that hexagonal and square hole-arrays do not have the same peak position for the same periodicity. This is due to the difference in the constant factor C between the two geometries. Figure 3.11 represents the normalized-to-area transmission spectra at normal incidence for a hexagonal and a square arrays with 440 nm and 380 nm periodicities respectively, milled in the same Ag film, and both having the same hole diameter *D* = 140 nm. Although both arrays have matching peaks at around 710 nm, the transmission intensity of the hexagonal array (the black curve in Figure 3.10) is ~ 2 times larger.[112] This can be explained by the number of degenerate modes which corresponds to the each geometry.

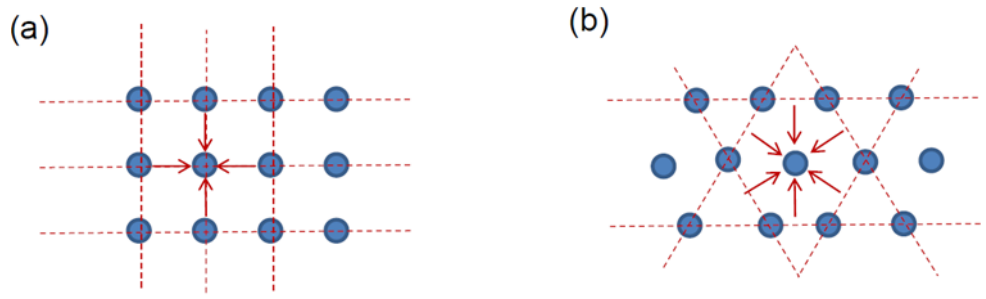



**Figure 3.12:** The degenerated SPPs modes in the case of square (a) and hexagonal hole-array (b).

The degeneracy of the SPPs modes supported by hole-arrays at normal incidence can be retrieved from the factor C in equation (3.6). One can obtain the same value for C in different configurations of the integers *i* and *j*. There are four degenerate modes for the square array: (1, 0), (-1, 0), (0, 1), and (0, -1) and six for the hexagonal array: (1, 0), (-1, 0), (0, 1), (0, -1) (1, -1), and (-1, 1). As illustrated in Figure 3.11a and b, modes with same energy propagate in different directions, and thus contributing to the degeneracy of the mode. As a result, one can obtain higher strong coupling efficiency simply by modifying the geometry of the array. In the next section, we will discuss strong coupling of organic material with surface plasmons and implement such system to investigate bulk property modifications which might arise from the SPP interaction with the material.

## 3.1.4- Strong Coupling on Plasmonic Arrays

As mentioned in the previous section, periodic arrays can excite selective SPP modes which are confined to the surface of metal and evanescent into the dielectric medium. Therefore, placing molecules having transitions that match with the confined SPP modes, can lead to strong coupling and consequently the observation of normal mode splitting. Next we provide experimental evidence of this by coupling merocyanine (MC) dye molecules to plasmonic arrays and then investigate its effect on the surface properties as we will see in the next section.

In order to achieve strong coupling of merocyanine (MC) dye molecules with plasmonic resonances, we first mill a hexagonal hole-array (having periodicity of 250 nm and hole diameter of 120 nm) in a 120 nm Ag film evaporated on a glass substrate. Then we deposit a thin film of spiropyran (SPI) molecules embedded in a PMMA matrix on the top of the milled array.

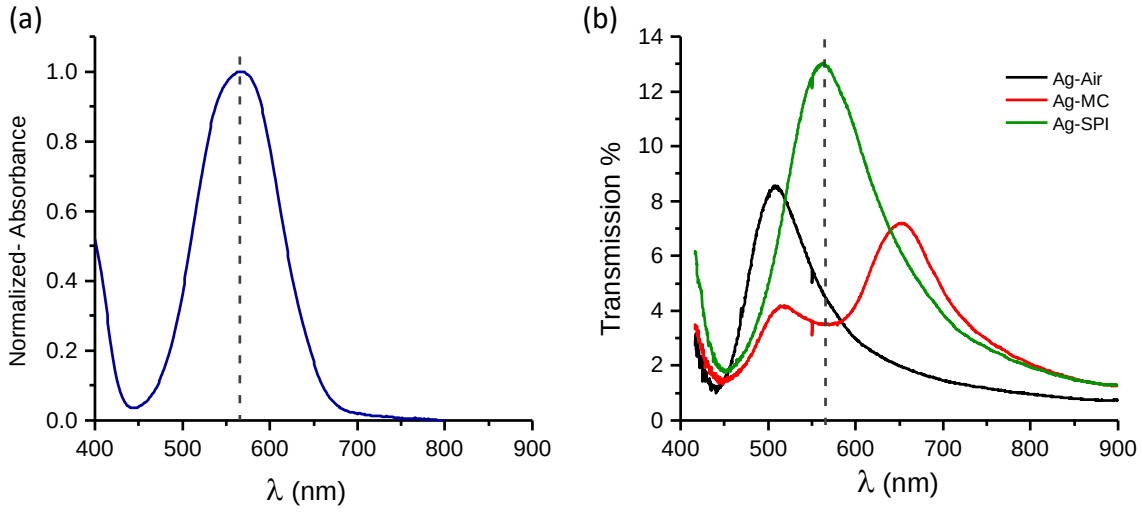



**Figure 3.13:** (a) Normalized absorbance of MC with a maximum centered at 565 nm (dashed line). (b) Transmission spectra at normal incidence for the same hole-array ($a_0$ = 250 nm, D = 120 nm) at different interfaces. The red curve represents the splitting of peaks due to the coupling of MC transition band (centered at the vertical dashed line) with the plasmonic resonances.

Here, we recall from section 1-4 of the first chapter, that spiropyran (SPI) is a transparent molecule in the visible spectrum that can be photisomerized to MC (which has an absorbance peak at 565 nm as presented in Figure 3.13a) under UV irradiation, the inverse process taking place under irradiation with visible light. This quality allows us to reversibly switch from weak to strong coupling using the same sample and acquire measurements under conditions where all other variables are constant.[40] Figure 3.13b shows the transmission spectra at normal incidence taken for the array in contact with air (black curve), then after the deposition of SPI in PMMA film (green curve), and after the photoisomeration to MC (red curve). The value of the Rabi frequency $\Omega_R$ is calculated to be 504 meV, which is in fact about 23% of the molecular transition energy (2.19 eV), consequently putting the system in the ultra-strong coupling regime.[40,45] Moreover, the described system was then used for the investigation of strong coupling effects on the wetting properties of a material as well detailed in the next section.

## 3.2- Wetting Properties Under Strong Coupling

In 2013, Hutchison et al. showed that the work-function of merocyanine (MC) photochromic molecules could be altered by strong coupling with resonant SPPs.[53] Such a change would in turn lead to a change in the polarizability of the medium and thus of the free surface energy. One way to test the existence of such a change is to measure the contact angle at the interface between liquid droplets and the surface of a thin film of MC molecules incorporated into the PMMA polymer matrix before and after their coupling to resonant SPP modes (Figure 3.14).

The contact angle $\theta_c$ is a parameter which quantifies the wetting characteristics of a liquid on a solid material.[113] While all parameters affecting the contact angle between two materials are fixed, any change in its value would indicate surface energy modifications of either or both materials. In fact, contact angle variations due to charge redistribution at the interface between the droplet and some insulators were observed in the so-called "electro-wetting" phenomenon[114,115] (which is achieved when potential difference is applied between the droplet and a semiconductor). Nevertheless, observing such changes would register a unique surface property refinement under strong coupling, and thus entering a new realm of research in both fundamental surface science and application.

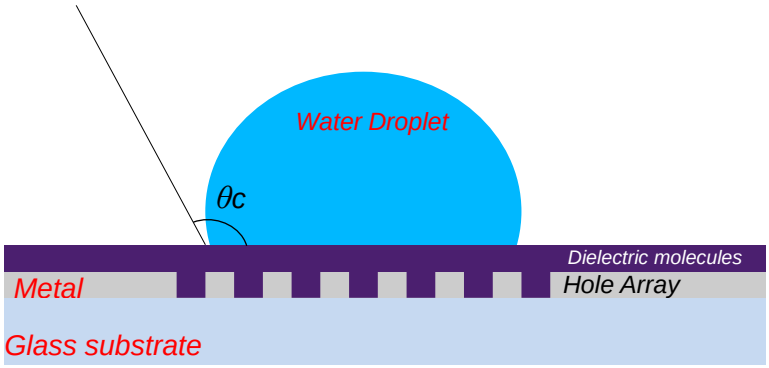



**Figure 3.14:** Schematic illustration of the experiment for measuring the contact angle $\theta_c$, located between a water droplet and the film containing MC molecules. The film is spin-coated at the top of hole-array.

First, it is important to give a brief introduction to the contact angle, its significance, and the factors affecting its values. In principle, the contact angle correlates with the interaction factors coexisting between three interfaces: solid-liquid (SL), solid-gas (SG) and gas-liquid (GL). Then, $\theta_c$ is defined by the angle between the solid-liquid interface (which is also called the "contact line")[116] and the tangent to the liquid-gas interface, and is given by Young's equation[117] as:

$$cos\theta_c = \frac{(\gamma_{SG} - \gamma_{SL})}{\gamma_{LG}} \tag{3.7}$$

where $\gamma_{SL}, \gamma_{LG},$ and $\gamma_{SG}$ represent the surface tension at the SL, LG, and SG interfaces respectively as represented in Figure 3.15.

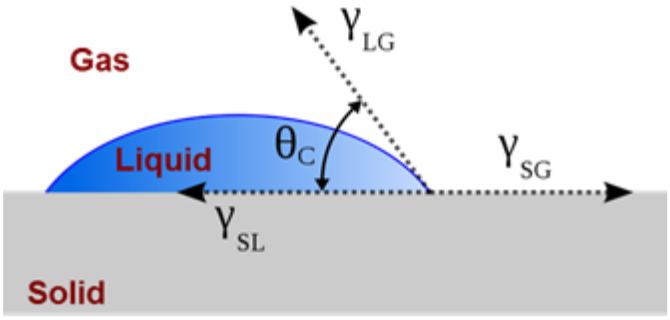



**Figure 3.15:** Schematic representation of the contact angle $\theta_c$ and the surface tension γ of the three coexisting interfaces. (Figure adapted from Wikipedia).

However, droplets on extended surface domains can exhibit contact angles which do not entirely satisfy the classical Young equation.[118] Consequently two famous models were proposed: the Wenzel model[119] (equation 3.8 below) which suggests that the area of contact at the SL interface is in fact larger than the actual area covered by the droplet due to the surface roughness, and the Cassie-Baxter model[120] (equation 3.9 below) which involves finer roughness features. As a result, each model defines a new contact angle (the Wenzel angle $\theta_w$ and the Cassie-Baxter angle $\theta_{CB}$) in order to incorporate the surface roughness factors ($r$ and $\phi$) at a microscopic scale as presented in equations (3.8) and (3.9).

As will be discussed later, the surface roughness factor plays a major role in our experiment.

$$cos\theta_w = rcos\theta_c \tag{3.8}$$

$$cos\theta_{CB} = \phi(cos\theta_c + 1) - 1 \tag{3.9}$$

## 3.2.1- Experimental Section

In this section we describe the methods and tools utilized in the experiments presented in this chapter. A special emphasis will be given to the Focused Ion Beam (FIB) instrument which played a major role in the fabrication of samples utilized in this entire thesis.

### A- Focused Ion Beam (FIB):

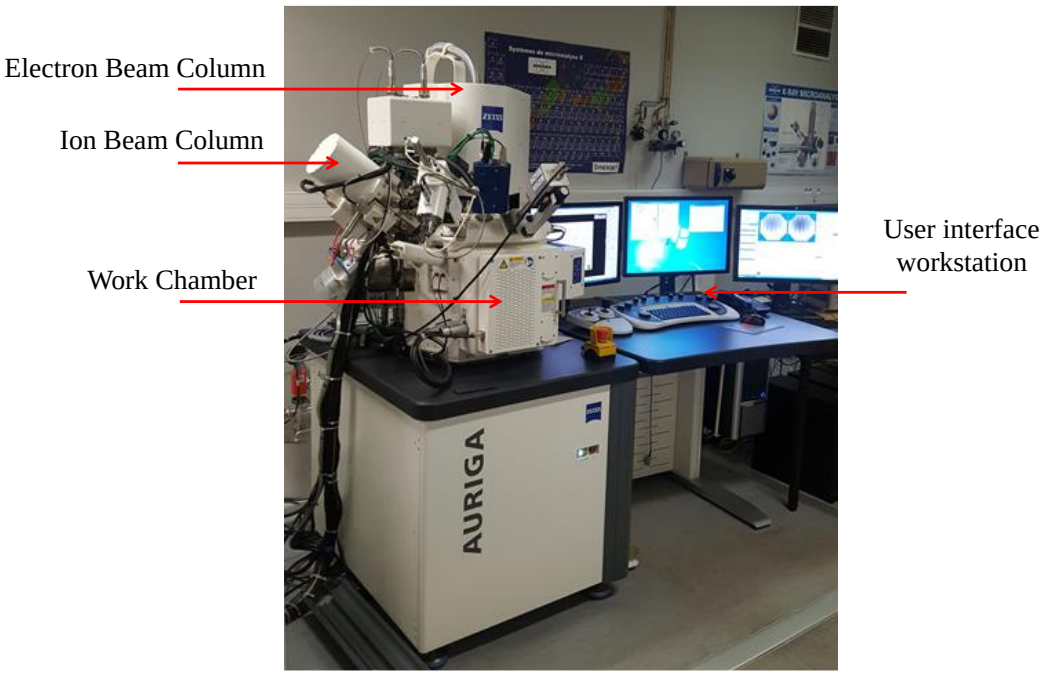



**Figure 3.16:** Photo of FIB system (Auriga Zeiss). The most important components are indicated by the red arrows.

The FIB is a technique which allows the execution of a set of state-of-the-art nanofabrication and nanocharacterization processes. The FIB instrument is an ideal tool for 3D high resolution imaging (in both ion beam and electron beam modes), patterning of complex nanostructures (e.g. hole-arrays), maskless deposition of both metal and insulator nano-sized materials, and detection of topographical and compositional information. Modern FIB systems have wide applications in semiconductor industry and processing environments[121] as being successful tools for device preparation modification, mask repairing, process control and failure analysis.[122] This technology is becoming widely spread in semiconductor research and more recently in biology for ultrastructural imaging of biological systems.[123]

Our lab is equipped with a dual-beam Auriga FIB device form Zeiss (the one present in Figure 3.16) which provides access to a number of sample preparation, imaging and characterization techniques. The Ga ion beam column is mainly used for milling while the electron beam column provides scanning electron microscopy (SEM) imaging. The working chamber provides a high vacuum (~ $10^{-7}$ mbar). All the mentioned components are controlled via the software system of the workstation.

The ion beam is generated by the extraction of Ga ions with a strong electric field. The ions are then directed by the column towards the sample through a set of lenses and aperture. High control over a set of discrete beam current values (ranging from 10 pA to 20 nA) allows a fine beam for high-resolution milling on sensitive samples and a heavy beam for fast and rough milling. Inside the work chamber, an electrically controlled mobile stage for the sample is used for sample positioning such that the same spot is simultaneously detected by both the ion and electron beams. Once the latter condition is achieved, the sample is then ready to receive the ion beam for milling. The removal of sample material (for example the metal) is the result of its physical sputtering under the action of the ion beam. The ion beam milling/deposition has a working field of view of 250 μm x 250 μm, but however such field of view can limit the milling resolution. For this reason, arrays are milled no larger than 100 μm x 100 μm in order to obtain quality structures (as we will see later in the next section).

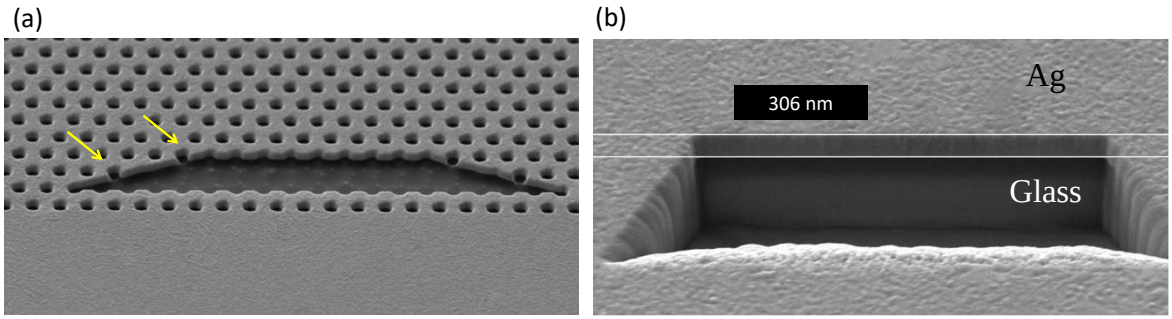



**Figure 3.17:** SEM images of cross-cuts created by the ion beam in: (a) Au film showing the cylindrical shapes of the milled holes as indicated by the yellow arrows, (b) a 300 nm Ag film evaporated on a glass substrate in order to measure the actual thickness of the film by imaging.

The features of the milled shapes (geometrical shape, sizes, periodicity, etc …) are chosen and processed via the Nanopatterning and Visualization Engine software. The same software allows the reproducibility of structuring which can be maintained by recording the dwell time (time of exposure of a certain point on the sample to the ion beam), number of dwelling repeats on the same spot, and dose (current per unit area). Figure 3.18 show a cross-cut created at the surface of the samples under the action of the ion beam, a feature which allows us to image the profile of the milled holes all the way through the metal depth (Figure 3.18a) and to measure the actual thickness of metals (Figure 3.17b). Consequently, all the SEM images (for instance Figure 3.6a), hole-arrays, and other structures presented in this thesis were obtained by using the SEM mode of this FIB device.

### B- <u>Acquisition of Transmission Spectra:</u>

The transmission spectra through the arrays were acquired using and inverted microscope (Nikon TE 200), which is connected to a spectrometer (Acton SpectraPro 300i) and a Si charged-coupled-device (CCD) (Princeton Instrument VersArray 1300B).

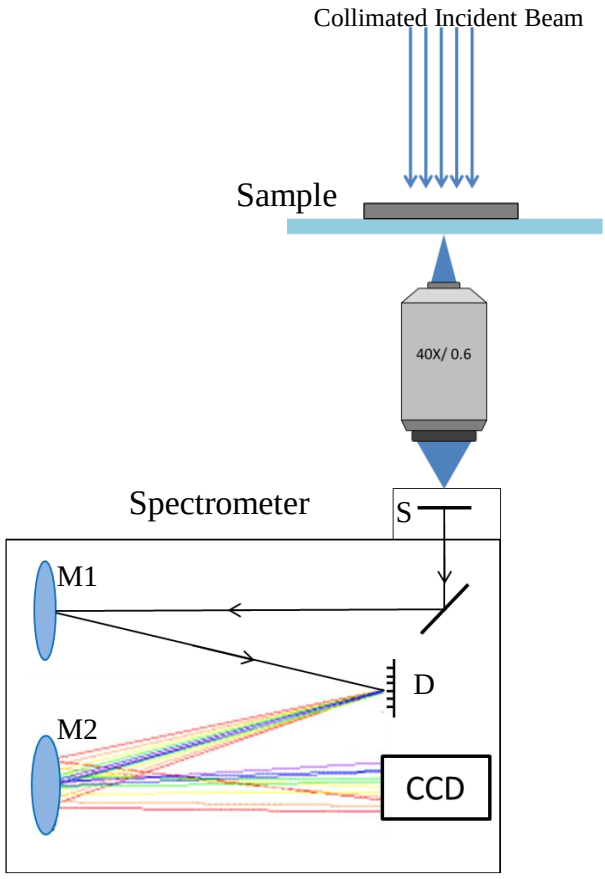



**Figure 3.18:** Schematic representation of the acquisition of transmission spectra showing the passage of the incident beam through the sample towards different parts of the system: the microscope objective, the spectrometer, and finally the CCD camera.

For the measurements, the sample is aligned on the optical axis of a microscope and illuminated with collimated light. Figure 3.18 shows how the transmitted light through the microscope objective lens ( with magnification of 40x and a numerical aperture (NA) of 0.6) enters the spectrometer through the entrance slit S, is reflected by the collimating mirror M1 towards the diffraction grating D and finally reflected by the focusing mirror M2 to be collected by the CDD camera. This measurement method was used for all the transmission spectra of microscopic structures that are present in this thesis. Moreover, the same microscope can be used in reflection mode where the incident beam arrives at the sample from the objective side. Hence, we were able to use the same system for acquiring reflection spectra and emission spectra as will be discussed in the next chapter.

### C- Contact Angle Measurements:

Contact angle measurements were carried out using a drop shape analyzer (DSA) (DSA100 from KRÜSS). The instrument is mainly composed of a syringe, a stage, a camera and light source which are all electronically controlled via computer software.

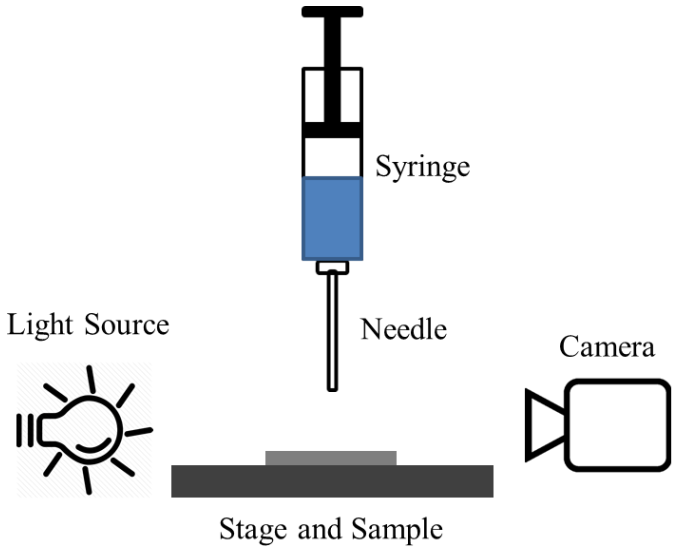



**Figure 3.19:** Schematic representation for the main parts of the drop shape analyser (DSA).

Figure 3.19 provides a simplified representation of the DSA set up including the main parts required for measuring the contact angle: The sample is held on a horizontal stage which can be moved manually in all 3-axes directions. A camera and a light source are placed horizontally and opposite to each other in order to acquire an image for the drop with a remarkable contrast compared with its background. The syringe is associated with a tip customized to fit a set of needles of different shapes, sizes, and material to control the size and the material of the desired drop. In our experiment we used NE50 needle with 5 µm internal diameter which has been designed for the manual dosing of small volumes below the microliter range. The piston is controlled via software and has a pressing resolution of 0.1 µL.

The drop shape analysis (DSA) is an image based method for determining the contact angle from the shadow image of a drop. There are several techniques for the measurement of contact angle,[113,124] but however, we adapt the static drop analysis technique.

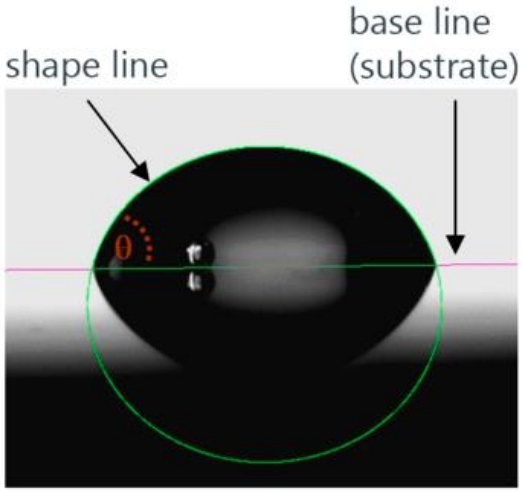



**Figure 3.20:** Image of a sessile drop taken by the DSA100 instrument with its fitted contour (shown in green). The figure is reproduced from (https://www.kruss.de/services/education-theory/glossary/drop-shape-analysis/)

In static drop analysis, a sessile drop (which is a free drop lying on the surface of a solid) is gently placed onto our sample. An image of the drop is recorded with the help of a camera and transferred to the drop shape analysis software (see Figure 3.20). Right after the image is captured, a baseline highlighting the drop-solid interface is usually selected manually. As a result a contour recognition (the green line in Figure 3.20) is initially carried out based on a grey-scale analysis of the image. In the second step, a geometrical model describing the drop shape is fitted to the contour and consequently giving information about the measured contact angle with an estimated volume of the drop.

### D- Sample Preparation:

Ag films (120 nm thick) were deposited on top of a cleaned glass substrate using an electron beam evaporator (Plassys ME 300) at optimized working pressure ~ $10^{-6}$ mbar and at a deposition rate ~0.2 nm/s. Sub-wavelength hole arrays (similar to one in Figure 3.21) were milled by Auriga FIB system in the Ag films with varying periodicities (220 nm, 250 nm, 280 nm, and 320 nm) and hole size kept equal to half the periodicity. A solution composed of a mixture of 1.5% in weight 1′,3′-Dihydro-1′,3′,3′-trimethyl-6-nitrospiro[2H-1-benzopyran-2,2′-(2H)-indole (Aldrich) SPI, and 1.5% in weight of Poly(methyl methacrylate) (average Mw ~120,000, Aldrich) PMMA in Toluene (anhydrous, 99.8%, Aldrich) was prepared. The solution was then deposited on the top of the arrays by spin coating. Photoisomerisation of SPI to MC was performed under the irradiation of 365 nm near UV light using VL-6.LC (from VILBER) for durations of 10 to 15 minutes.

## 3.2.3- Results and Discussions

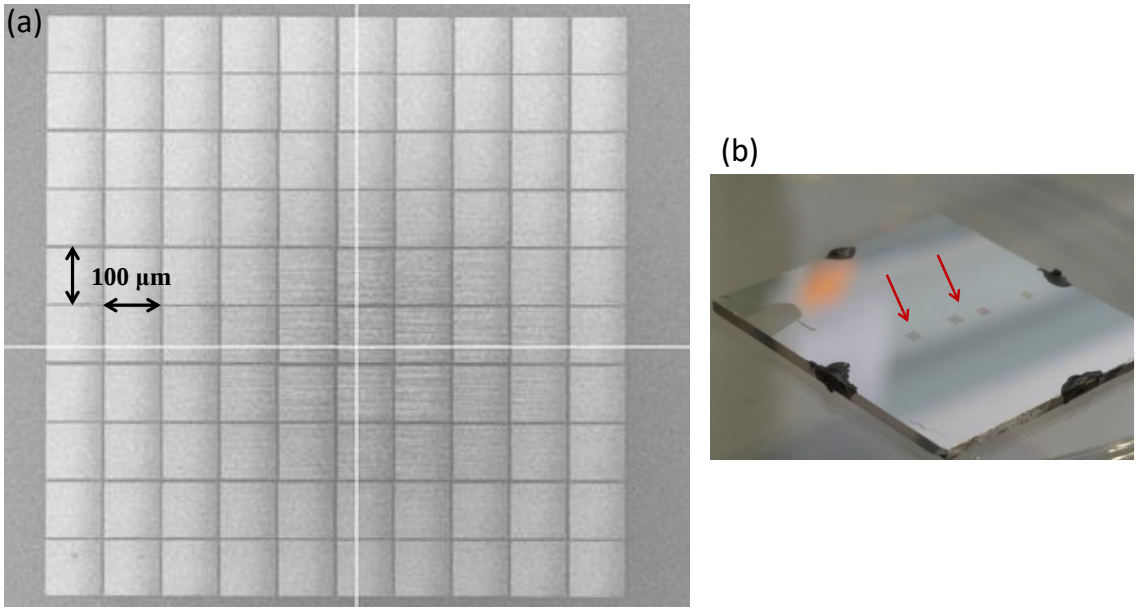



**Figure 3.21:** (a) SEM image of a ~ 1 mm$^2$ large plasmonic array milled in 120 nm Ag film by using Auriga FIB machine. The small squares are identical hexagonal hole-arrays ($a_0$ = 250 nm, D = 120 nm) separated by 5 µm from each side. (b) A captured photo for the sample carrying arrays different periodicities indicated by the red arrows.

The volume of the water droplet to be placed on the plasmonic arrays is on the order of 1 μL. Therefore, it required the milling of large hole-arrays (around 1mm$^2$ in area) in order to be able to accommodate the drop. This in fact is one of the major challenges for the sample preparation. The formation of large hole-arrays with custom geometry, periodicity, and hole-size is not straight forward (as it is the case of few tens of μm$^2$ size arrays) and it has been the interest of many nanofabrication studies due to their large application potential such as for biosensors.[125] Several techniques for the fabrication of large nano-arrays have been reported such as electron beam lithography,[126] nanoimprint lithography,[127] reactive ion etching (after lithography process),[128] and monolayer formation of self-assembled colloids over large areas.[129]

Here, we succeeded in the fabrication of large area hole-arrays by FIB. Figure 3.21a shows an SEM image to one of such arrays milled in 120 nm Ag film. The large overall square is an assembly of smaller squares which are separated by ~ 5 μm (vertically and horizontally). Each small square is a (100 μm x 100 μm) hole-array with hexagonal geometry (similar to the one present in Figure 3.6a), having periodicity of 250 nm and a hole-size of 120 nm. Such arrays were milled with different periodicities on the same sample as presented in Figure 3.21b. The transmission spectrum through this periodic structure, with and without the SPI/MC layer, is presented in Figure 3.13b.

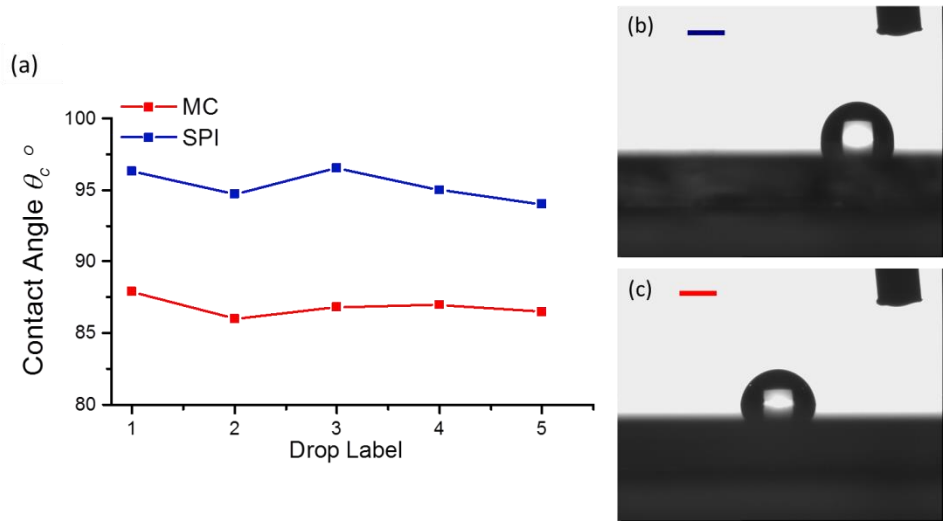


**Figure 3.22:** (a) The value of contact angle measured for a set of 5 different drops on the surface of (b) SPI before and (c) after irradiation with UV.

The first experiment for the contact angle measurement was conducted to highlight the difference in the surface tension between water droplets on bare surfaces of SPI and MC films, i.e. in the absence of strong coupling. To do so, 2% in weight SPI molecules mixed in Toluene were spin-coated on the top of an Ag film, deposited on a glass substrate, forming a 110 nm thick layer. Five distinct drops of Milli-Q water having different volumes were placed on the SPI layer and static drop analysis to measure the contact angle was performed. The same procedure was followed after the photoisomeration of SPI to MC by UV irradiation. The graph in Figure 3.22a displays the values of the measured contact angle for the 5 different drops on each of the bare molecule surfaces (SPI in blue and MC in red). The contact angle values vary between 94° and 96.5° on SPI, while they vary between 86° and 88° on MC. The contact angle difference ($\Delta\theta c = \theta_c^{SPI} - \theta_c^{MC}$) was calculated, and it averages ~8.5° (with an error range of ±1.3°). It can be concluded that MC has higher surface tension than SPI, and this is typical because MC has higher ground state energy as compared to that of SPI.[68] Contact angle variations for SPI molecules, before and after photo switching, on various surface textures were measured by other groups, and they reported similar $\Delta\theta c$.[130–132] Figures 3.22b and 3.22c are camera shots taken for the drops by the DSA, and they display the drop shape on the surfaces of SPI and MC respectively.

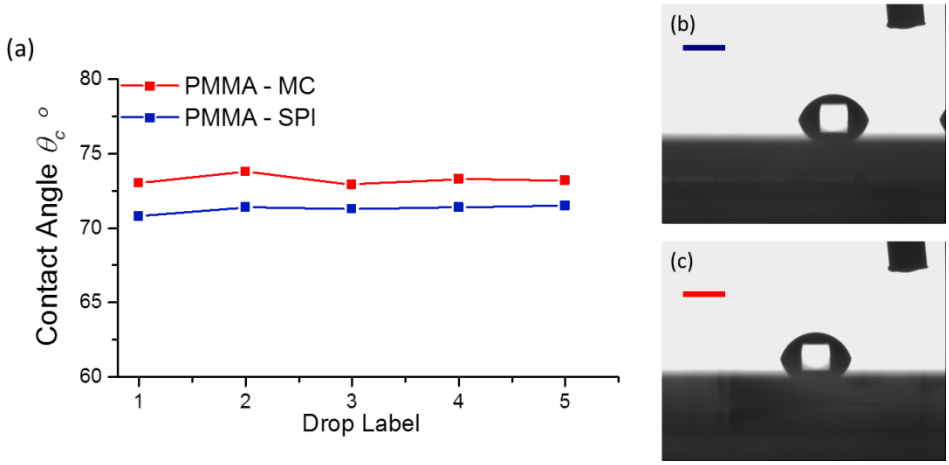


**Figure 3.23:** (a) The value of contact angle measured for a set of 5 different drops on the surface of (b) PMMA mixed with SPI before and (c) after irradiation with UV.

The same experiment described above was repeated, but this time when the SPI molecules are embedded in a PMMA polymer matrix (as described in the experimental section). The PMMA film ensures identical extended surface domains before and after the photoisermation process, and thus provides control over external factors which contact angle. The results presented in Figure 3.23a show measured contact angle values for 5 different drops placed on the surface of PMMA-SPI film before and after switching to MC. It is clear that small or no variation exist within the same molecule, and that the difference in contact angle $\Delta\theta_c$ has dropped to ~1.7°. However, the major aim is to see a larger contact angle difference once the experiment is performed on the MC molecules coupled on the resonant plasmonic structures. Figures 3.23b and 2.23c provide a visual confirmation to the numerical results, where the spherical curvature of the water droplets are observed to be very similar, (unlike those present in Figure 3.22 a and b).

Table 3.1: Variations in the contact angle measurements on plasmonic structures

| | Δθc (independent measurements) | | | | |
|---|---|---|---|---|---|
| On Resonance Array | 0.1 | 1.1 | 1 | 7.4 | 4 |
| Off Resonance Array | 2.3 | -0.9 | -0.6 | 1.5 | 1.3 |

Similarly, a set of measurements for the contact angle were acquired on plasmonic structures. Now that the large hole-arrays were deposited by a layer of SPI molecules embedded in PMMA matrix, small drops (~0.5μL) of Milli-Q water were placed on these structures and the contact angle was measured before and after the UV irradiation of SPI. The experiment was repeated for several times by placing the droplets above on resonance and off resonance plasmonic arrays (independently) and the contact angle difference $\Delta\theta c = \theta_c^{SPI} - \theta_c^{MC}$ was recorded (as presented in Table 3.1). It can be noticed from Table

3.1 that the values were inconsistent, and the negative values are obtained when $\theta_c^{SPI} < \theta_c^{MC}$.

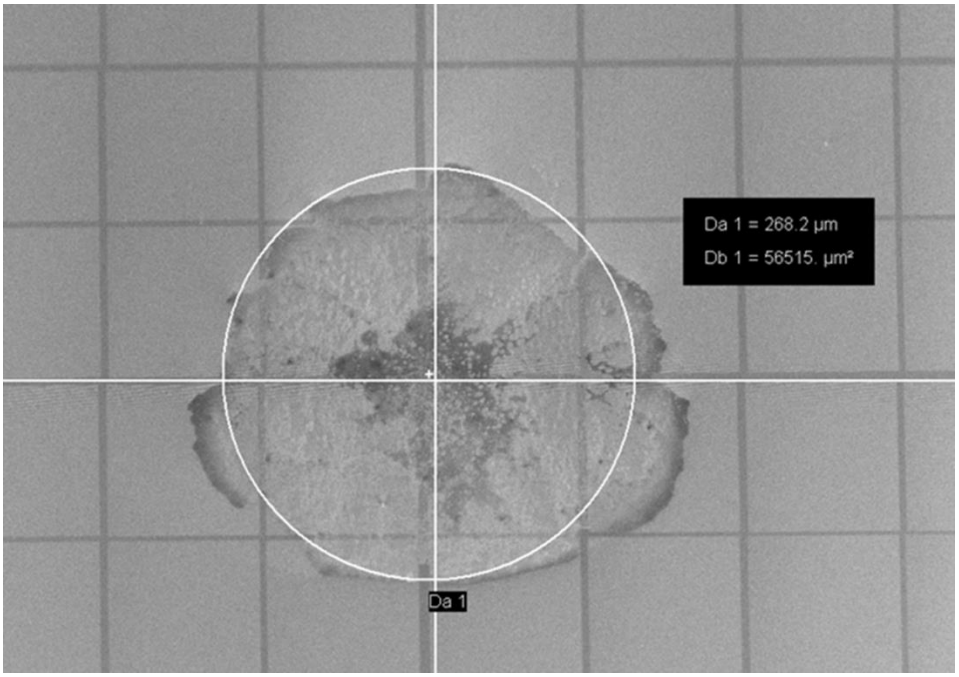



**Figure 3.24:** SEM image on a section of the large array showing the mark left by the water droplet (having an area of ~ 56515 µm$^2$) after its evaporation.

It was observed that the water droplets were leaving an impact on the surface structures as can be seen in Figure 3.24. These features were later realized to occur very rapidly leading to modifications in the surface structure and consequently the contact angle. In fact, this explains the dispersed $\Delta\theta c$ values presented in Table 1. In fact, we later observed that it was leaving the same impact on the surface of metals even without the presence of polymer (PMMA in our case). In order to better understand this behavior, a drop of water was randomly placed on the surface of Ag film and the time evolution of contact angle was recorded for the same drop and showed remarkable changes within periods ~10's of seconds. In fact, Ag surfaces are known for their reactivity with ambient environment,[133] and it was shown that water interaction with oxidized Ag surface enhances its surface restructuring.[134] For this reason, the phenomenon (impact of water droplets) was investigated with Au, which is assumed to be less reactive, to test whether water causes

surface restructuring in the absence of adsorbents. For this, Milli-Q water drops were placed on the surface of a Au film and were let to evaporate in normal laboratory conditions. After the droplet evaporation, similar features to those present in Figure 3.24 were observed. It was still unclear whether these features were surface restructuring or some contaminants from water.

Thereby, a water distillation setup was assembled and triple distillation of the Milli-Q water was performed in order to ensure the purity of the water droplets. On the other hand, 300 nm Au film was deposited by thermal evaporation at a low rate (~0.1 nm/s) on a quartz slide. Droplets of the triple distilled water were placed via well cleaned glass pipette, and the water droplets were left to evaporate. The experiment was carried out this time in a clean room in order to minimize the interaction with external contaminants.

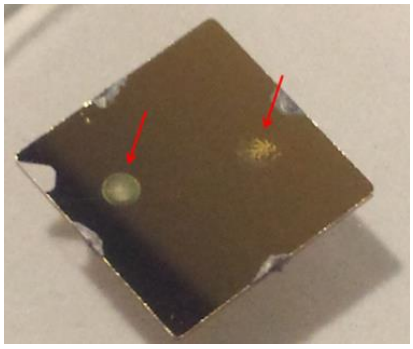


**Figure 3.25:** Captured photo for the Au sample showing the features (indicated by the red arrows) left after the evaporation of triple distilled water droplets.

The photo in Figure 3.25 was captured after the water droplets have evaporated. As indicated by the red arrows, features were formed can be clearly observed by the naked eye.

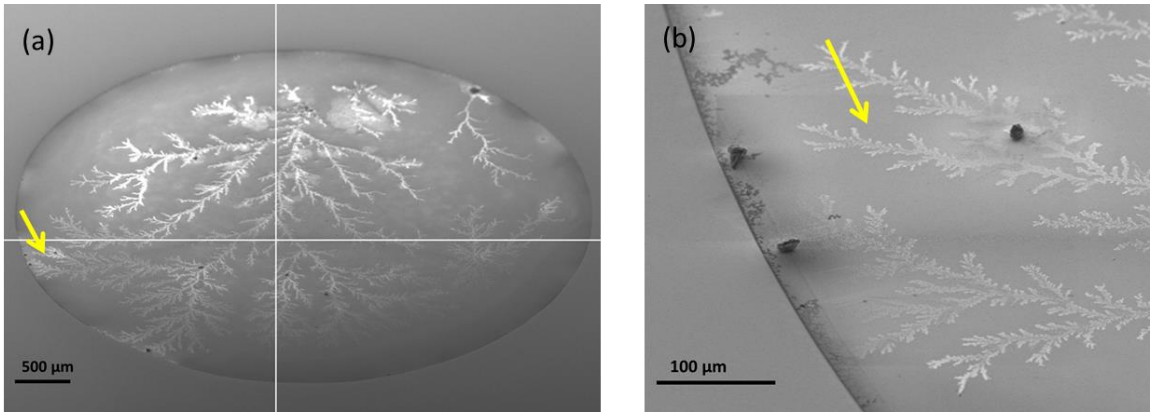



**Figure 3.26:** SEM image of the feature present in Figure 3.25 due to the water droplet. (a) The whole feature showing a contrast at the circumference. (b) A magnified SEM image of the area pointed by yellow arrow in (a).

The sample in Figure 3.25 was then imaged by SEM with different magnifications. Figure 3.26 a and b show structures having tree-like branches shapes on the surface of Au. At a certain magnification, one can also observe the circumference of the impact of the droplet inside which the features appear (see Figure 3.26 a and b).

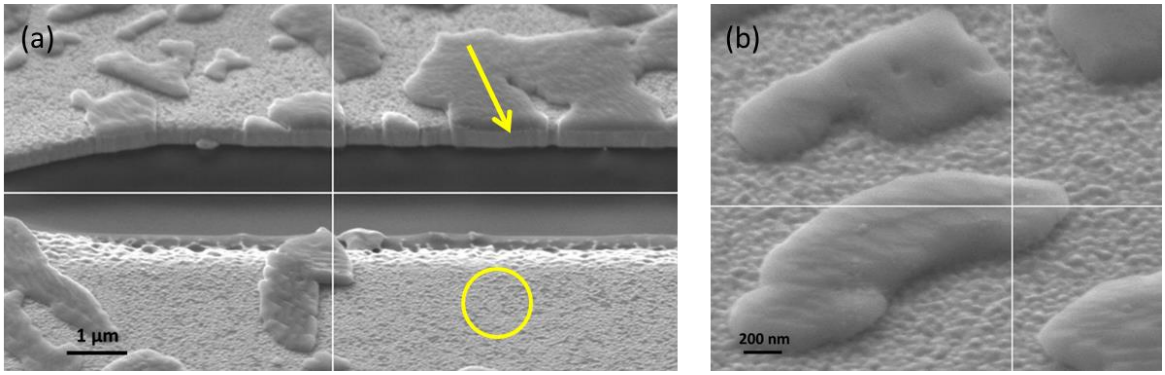



**Figure 3.27:** SEM images: (a) at 23K times magnification and shows the cross cut at the features. A clear contrast between the original Au film and the features is pointed by the yellow arrow. (b) At 90K times magnification, showing the area inside the yellow circle of (a) and highlighting the roughness modification to the surface imposed by the features.

A cross cut was made by FIB and subsequent SEM imaging reveals a contrast between the original gold film cross-section and that of the new features (as indicated by the yellow arrow in Figure 3.27a). It can be then concluded that the features and Au are of

different material. Moreover, those impurities residing at the surface of Au, form roughness of different sizes. For instance from Figure 3.27a, the large islands have roughness in the order of 100's of nm, while in Figure 3.27b (which a magnified image to the area in yellow circle of Figure 3.27a) they are in the order of 10's of nm. These values were confirmed by atomic force microscopy (AFM) measurements.

The final stage of the characterization of features residing on the surface of metals during their evaporation is the material identification by energy dispersive x-ray (EDX) spectroscopy.

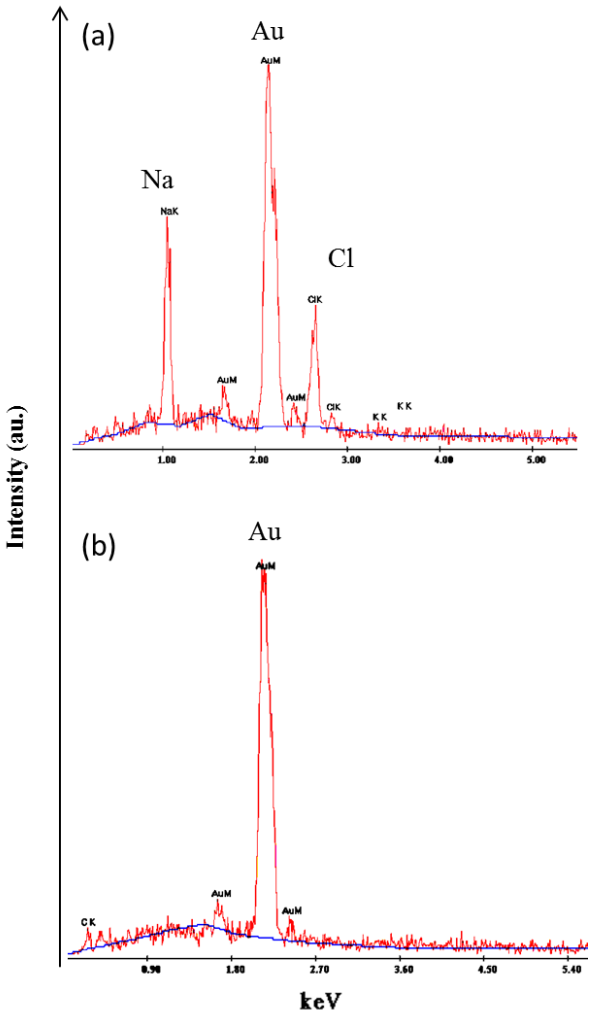


**Figure 3.28:** EDX analysis spectra showing the elemental analysis on sample of Figure 3.25 (a) when probing the features (b) when probing the Au surface away from features. The blue curve represents the background signal.

EDX analysis was performed on the sample of Figure 3.25 targeting both the new surface features and the untouched Au surface. The EDX spectra indicate the presence of two new elements (Na and Cl) besides Au (see Figure 3.28a). These elements were completely absent when probing the Au surface away from the features, as can be seen in Figure 3.28b. It can be concluded that those new elements came most likely from the environment and could possibly be collected from ambient air despite the triple distillation of water. This result shows again how difficult it is to make accurate measurements of wetting.

## 3.3- Conclusions

In this chapter, we show how SPPs can be excited by using hole-array structures milled on metal surfaces and demonstrated how hybrid light-matter states with large Rabi splitting achieved on such nanostructures of higher symmetry indicating the importance of SP mode degeneracy. Moreover, we made an attempt to investigate surface energy modifications under strong coupling of MC electronic excitations with plasmonic resonances. A brief introduction to measuring surface interactions via the contact angle was provided emphasizing on the effect of surface roughness.

After much effort, we could not demonstrate that the contact angle of the water is modified at the water-SPI and water-MC interfaces after strong coupling. Indeed, these measurements proved very difficult because we found that the water droplets leave a significant impact on the structure of the solid film, resulting in immediate changes in the values of the contact angle. After characterization of these structural modifications using scanning electron microscopy (SEM), atomic force microscopy (AFM) and electronic X-ray diffraction (EDX) analysis, we have been able to conclude that the evaporation of the

droplets affects the roughness of the surface of the polymeric film and could also leave impurities locally (such as Cl and Na) even when we use purified water. These changes not only affect the value of the contact angle for a single measurement but also make it very difficult to perform further measurements on the same set of holes and to ensure reproducibility of the results.

# CHAPTER 4:
# Strong Coupling in Liquid Fabry-Perot Nanocavities

It was discussed briefly in Chapter 1 that the strong coupling conditions could be experimentally achieved by different methods. In the previous chapter, we used periodic structures on metals to excite surface plasmon resonances. Due to their half-open character, such systems were ideal for our study of surface properties under strong coupling as it was for other preceding experiments.[47,53] In this chapter, the we exploit the Fabry-Perot (FP) cavity as another useful method for the investigation of molecular dynamics under strong coupling.

Firstly, the physics of FP cavities will be introduced in terms of multiple interferences. Then, a detailed explanation will follow outlining the fabrication of FP nanocavities in which solutions can be introduced such that light-molecule interactions can be studied at will in the liquid phase. These nano-fluidic cavities are fully characterized and put to use to achieve the strong coupling of electronic transitions of various dyes in solution. Particularly modifications to the photo-physical properties of a dissolved dye, chlorin e6, upon strong coupling to the optical modes of our cavities are presented and analyzed. Some paragraphs in this chapter are inspired by a submitted manuscript.[135]

# 4.1- The Physics of Fabry-Perot Cavities

A Fabry-Perot (FP) cavity behaves as an interferometer (or etalon) in which a beam of light undergoes multiple reflections between two semi-transparent reflecting surfaces, and whose resulting optical transmission (or reflection) is periodic in wavelength.

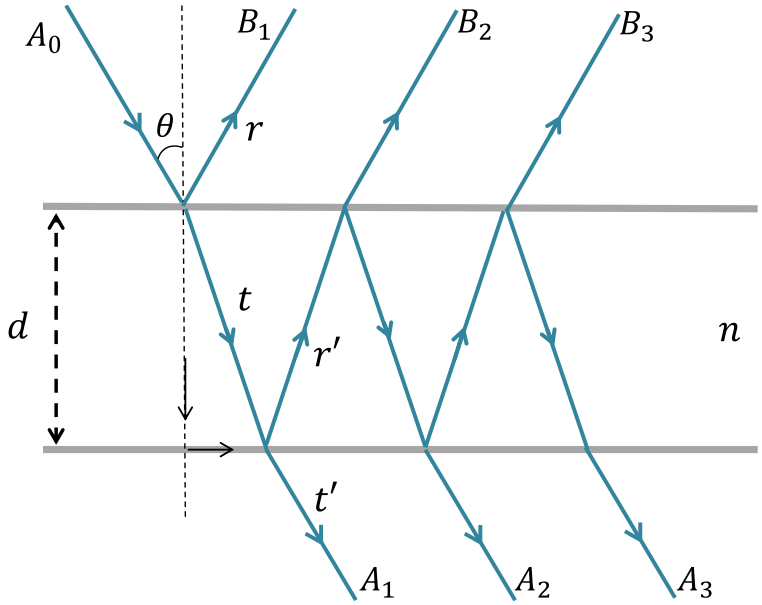



**Figure 4.1:** Schematic representation of multiple reflections occurring between the two mirrors in a FP cavity

For treating this system quantitatively, we consider the ideal case where the plates are infinitely thin and do not contribute to the optical losses. Also, we let the index of refraction ($n_{air} = 1$) to be the same anywhere outside the plates, and equal to $n$ in between (see Figure 4.1). Starting with the amplitude of the incident electric field $A_0$, the reflected amplitude from the first interface is given by $B_1$, while the partially transmitted amplitude from the second interface is given by $A_1$. The coefficients of amplitude reflection, $r$ and transmission $t$, denote light traveling from air to medium $n$ while the coefficients $r'$ and $t'$ denote light traveling from $n$ to air (all the details are represented in the scheme of Figure 4.1). Therefore, the amplitude of the transmitted waves can be thus written as:

$$A_1 = t\,t' A_0;\;\; A_2 = t\,t' r'^2 e^{i\delta} A_0;\;\; A_3 = t\,t' r'^4 e^{2i\delta} A_0;\;\ldots \tag{4.1}$$

The multiple output beams differ in phase due to the different path lengths traversed by each of the beams. The optical phase acquired by the light on one round trip between the plates is given by:

$$\delta = \frac{4\pi\, n\, d\, cos\theta}{\lambda} \tag{4.2}$$

where $d$ is the distance between the two plates, $\theta$ is the angle of incidence, and $\lambda$ is the wavelength of the incident beam. Now, the sum of transmitted wave amplitudes $A_T$ becomes:

$$A_T = t\,t' A_0 \left(1 + r'^2 e^{i\delta} + r'^4 e^{2i\delta} + \cdots\right) = \frac{t\,t'}{1 - r r'^2 e^{i\delta}} A_0 \tag{4.3}$$

The power transmission $T = I_t / I_0$ will be expressed in terms of equation (4.3) as:

$$T = \frac{I_t}{I_0} = \frac{A_T A_T^*}{A_0 A_0^*} = \frac{(t\,t')^2}{(1 - r\,r')^2 + 4\sqrt{r\,r'} sin^2(\delta/2)} \tag{4.4}$$

Since we consider a lossless system with identical surfaces, then: $r = r'$ and $r^2 + t^2 = 1$. Thus equation (4.4) simplifies to:

$$T = \frac{1}{1 + F sin^2(\delta/2)} \tag{4.5}$$

such that the factor

$$F = \frac{4R}{(1-R)^2} \tag{4.6}$$

is known as the finesse coefficient of the cavity and $R = (rr')^2$ is the reflectance of the mirrors. The fraction $[1 + Fsin^2(\delta/2)]^{-1}$ of equation (4.5) is called the Airy function and it shows strong dependence on the value $R$. The same equation imposes that the condition of a transmission maximum is $\delta/2 = m\pi$ where $m$ is an integer and represents the optical mode order of the cavity.

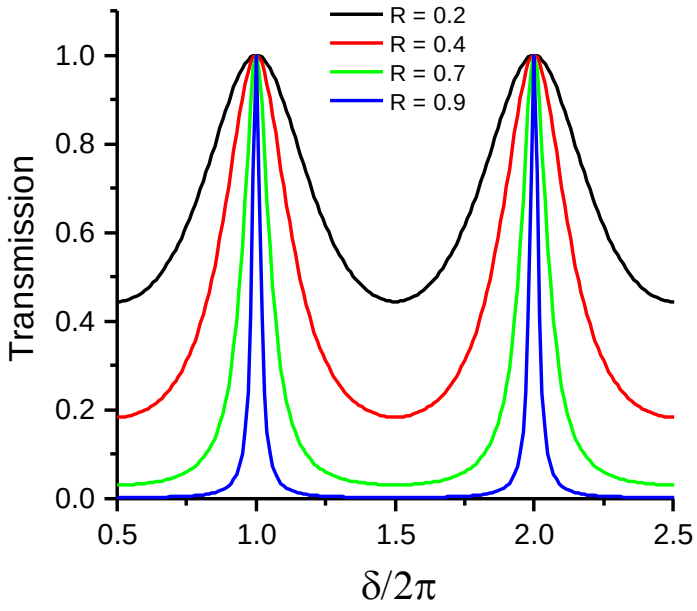



**Figure 4.2:** Airy function $[1 + Fsin^2(\delta/2)]^{-1}$ curves with different values of reflectance *R* of mirror.

The Airy function is plotted in Figure 4.2 for different $R$ values. It can be noticed that the transmission peaks are broad and indistinct for mirrors with weak reflections (for instance $R = 0.2$), whereas they appear to be large and sharp with high Q-factor in the case when *R* approaches unity (see Figure 4.2). Such large reflectivity values (0.7-0.9) could be obtained in the visible range for Ag mirrors of thickness ~ 30nm.

## 4.2- Electronic Light-Matter Strong Coupling in Liquid Fabry-Perot Nanocavities

In the presence of the growing interest in studying strongly coupled materials (as detailed in Chapter 1), there is a need to explore SC of molecules in liquid solutions since that it is the natural condition of many molecular processes. Experiments in liquid solutions have only been achieved for vibrational strong coupling (VSC) which is facilitated by the fact that the vibrational modes are in the IR which allows one to use micro-fluidic Fabry-Perot (FP) cavities (e.g. spacing 1~10 μm).[42,45,74–77,136,137] In contrast, electronic strong coupling (ESC) of molecules in the liquid form has not been reported yet for the simple reason that the cavity length in the visible is on the order of 100 nm which is technically very challenging. Among other things, the nanofluidic FP cavity mirrors (Figure 4.3a) need to be uniformly flat on a scale much smaller than the cavity length and the cavity must be accessible to the solution.

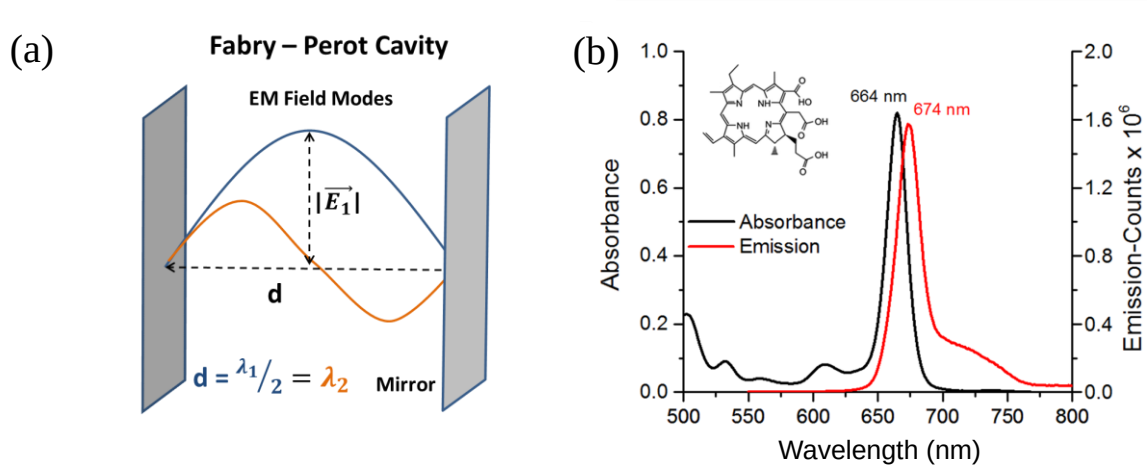



**Figure 4.3:** (a) Schematic illustration of the amplitude of the first and second Fabry−Perot (FP) cavity modes confined between two metallic mirrors. (b) Absorbance and emission spectra of Chlorin e6 in DMF and its molecular structure.

In this chapter, we explain the fabrication of nanofluidic FP cavities tunable over a wide range of visible wavelengths which can be filled with liquids. To illustrate the potential of such cavities we study the photophysical properties of a chlorophyll analog, Chlorin e6 (Ce6) shown in Figure 4.3b, in both the weak and strong coupling regimes. In particular, we compare the emission quantum yield and the radiative rate constant as a

function of detuning in both regimes which highlights the distinct features of the strong coupling condition.

Chlorin e6 has a sharp absorption peak (Q-band) at 664 nm and fluoresces with a small Stoke-shift at 674 nm (Figure 4.3b). In addition to these spectral features which are very suitable for studying light-matter interactions, it is characterized by high solubility in many solvents without forming aggregates.[138] In dilute conditions, it has a reasonably long fluorescence lifetime (4.4 ns) and a good emission quantum yield (~15% in ethanol).[139,140] These characteristics make Ce6 a good candidate among organic molecules for exploring liquid phase photoemission and relaxation processes under both strong and weak coupling regimes.

## 4.2.1- Fabrication of Fabry-Perot Liquid Nanocavities

To prepare the nanofluidic FP cavity having two parallel metallic mirrors separated by a distance *d* on the order of 100 nm, we developed the following technique. The sample preparation starts by evaporating a 50 nm thick Ag layer on a 2.5 cm x 2.5 cm glass substrate. The sample is then introduced in a Zeiss Auriga Focused Ion Beam (FIB) apparatus and a *ca.* 10-20 μm x 120 μm rectangular area is milled through the Ag layer and into the glass substrate to create the nanofluidic channel (Figure 4.4a and b). After the milling, another 30 nm of Ag is evaporated on the substrate to act as the cavity's bottom mirror. Another identical glass substrate with an Ag layer acting as the cavity's top mirror is also prepared. Then the two substrates are cold-welded by high pressure (~1.6 tons/cm$^2$) using a press normally employed for preparing pellets for IR measurements (Figure 4.4a). Cold-welding has already been used successfully to make solid state cavities.[141,142]

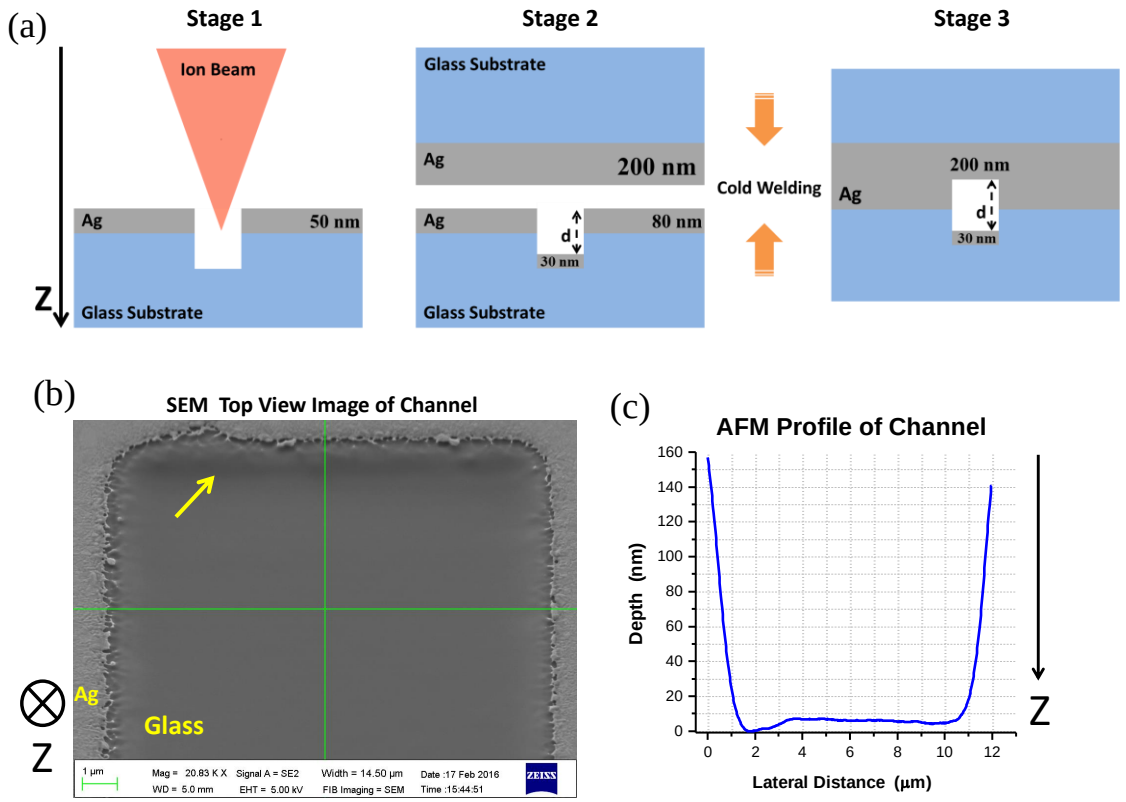



**Figure 4.4:** (a) The fabrication stages of nanocavities of thickness *d*, starting by milling through the Ag layer and glass substrate (stage 1), then Ag evaporation on the milled channels (stage 2) and finally cold-welding both substrates under high pressure (stage 3). (b) SEM image in top view of the upper part of a rectangle milled through 50 nm Ag and into the glass. A light shadow indicated by the yellow arrow shows milling also through the glass substrate. (c) The milled channel depth profile acquired by AFM along the width of the rectangle in (b).

A first set of cavities with increasing depth were milled along a line in the middle of the sample, connected between each other by a very small overlap area (emphasized by the yellow arrow in Figure 4.5c) resulting in a few millimeters long channel as shown in Figure 4.5a with and without solvent. The thickness of the top mirror layer depends on the required measurements. For instance, we used a 30 nm top Ag mirror when probing the cavities in transmission mode (as illustrated in Figure 4.5b) and 200 nm when characterizing the spectra in reflection mode (as we will see later in this Chapter). It is important to note that a 2 nm film of Cr layer is always present between the glass substrate and the Ag film in order to ensure strong adhesion. Finally, to introduce the molecules into the nanofluidic channels, the sample is simply dipped into the liquid solution which is

drawn in by capillary force. We have verified that many solvents including water wet the channels and therefore are spontaneously pulled in.

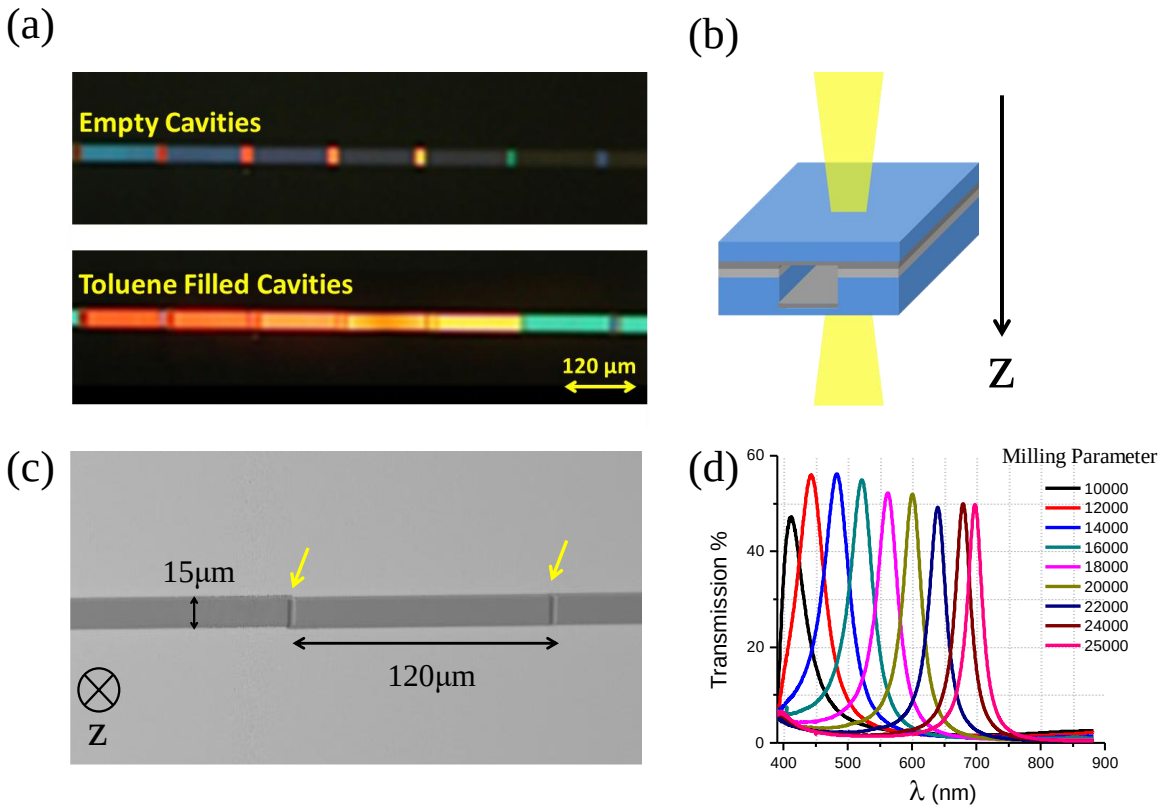



**Figure 4.5:** (a) Optical micrographs showing white light transmission through the nanofluidic FP cavities before and after filling them with toluene. The colored rectangles represent FP cavities of varying thicknesses, with the corresponding wavelength shift of the confined light mode. (b) Schematic diagram illustrating in 3D the final shape of the cavity and the transmission spectra obtained in (a). (c) SEM image in top view showing the milled channels through glass, and emphasizing the small overlap connections (indicated by the yellow arrows). (d) Transmission spectra through empty nanocavities, showing the photonic mode resonance as a function of FIB milling repeats.

The thickness of the nanofluidic FP cavity was controlled by milling different depths in the bottom substrate. High control over the cavity mode resonance is achieved by programming a large number of repeats on the Zeiss Auriga FIB to mill a given thickness. This enables very flat surfaces (less than a few nm variation over 5 µm) on

which the mirror can then be deposited (see Figure 4.4c). In Figure 4.5d, the transmission resonance of various channels is shown as a function of ion beam milling repeats. Under our milling conditions, the peak position moves by *ca.* 20 nm for every 1000 repeats reflecting the change in FP path length *d* as also can be seen in the colors of Figure 4.5a. In fact, this provides us with high control (up to 1nm) over the peak position. The color changes once again upon introduction of a solvent (here toluene) due to the increased medium refractive index inside the channel. The Q-factor of such cavities ranges between 20 and 60, depending on the type of metal (e.g. the imaginary part of the dielectric constant) and the mode used. The ability to mill FP nanocavities of 100s of microns lateral extent with desired shape, and with very high control of cavity thickness, is an outstanding point of our fabrication method, making these nanofluidic structures ideal for studying molecules in solutions in the weak and strong coupling regimes.

## 4.2.2- Experimental Section

### A- Sample Preparation:

BK7 glass substrates (25 x 25 mm) were subjected to standard cleaning procedures: sonicated in Helmanex solution (1% in MilliQ water), then rinsed with water and sonicated for 1 h in pure ethanol before being rinsed several times with pure water. The glass substrates were then dried in an oven. Layers of Cr (2 nm) and Ag (50 nm) were deposited consecutively on top of a cleaned glass substrate using an electron beam evaporator (Plassys ME 300) at optimized working pressure ~ $10^{-6}$ mbar and at a deposition rate of 0.2 nm/s. Channels were milled using a Zeiss Auriga FIB system. The ion beam current was fixed at 16nA and the dwell time to 1 µs. Only the number of milling repeats is varied to control the cavity thickness *d*. The milling removes the Ag layer and the desired depth in the glass (Figure 4.4b). Individual cavities were milled, for instance, as 12 µm x 120 µm rectangles, and a set of rectangles of various depths could be milled along a straight line forming a channel. Next, 30 nm of Ag was deposited over the milled sample to form the bottom mirror. Finally, another glass substrate with a 200 nm thick Ag layer was cold-

welded to the milled sample under high pressure (~1.6 tons/cm$^2$) using Specac Manual Hydraulic Pellet Press device.

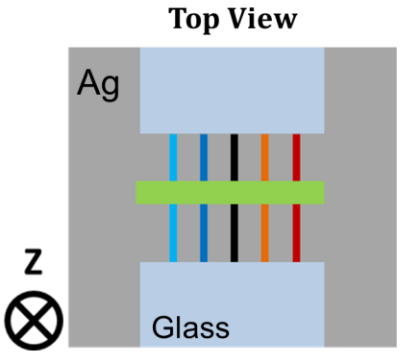



**Figure 4.6:** Schematic representation of the top view of samples used for our emission experiments. Each cavity is represented by a colored line based on its optical mode energy detuning relative to the molecule's absorption transition at 664 nm (*i.e.* cavities with photonic modes in neat DMF at 567 nm (light blue), 631 nm (blue), 665 nm (black), 678 nm (orange), and 733 nm (red)). The areas with neither top nor bottom mirror that act as reservoirs for liquid to enter the cavity are labelled 'glass'. The green horizontal rectangle is an area with only one mirror.

For practical reasons, we also prepared nanofluidic FP cavities of single optical path length in parallel as illustrated in Figure 4.6. Here, both ends of the substrate (blue area in Figure 4.6) were masked during metal evaporation to form a metal free space acting as a reservoir for the liquid to fill the channels. In addition, a mask was placed over parts of the milled channels (illustrated by the green rectangle in Figure 4.6) before evaporating the bottom mirror to create in each channel one-sided mirror areas which act as a reference for the optical characterization of the bare molecule.

**B- <u>Solution:</u>**

The solutions were prepared by dissolving Chlorin e6 (used as purchased from Frontier Scientific) in N,N-dimethylformamide (DMF) solvent (used as purchased from Sigma Aldrich ≥ 99.8%). The solution was then placed in a small beaker and the samples with the

nanocavities were dipped into the solution for ~ 1 hour to enable the liquid to fully enter the cavities.

### C- Reflection and Emission Dispersion Measurements

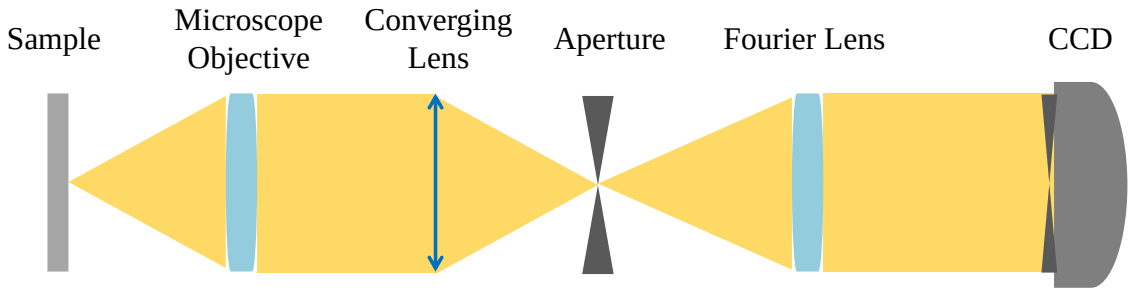



**Figure 4.7:** Detection scheme of the home built set up used for dispersion measurements showing the passage of light coming out of the sample through main parts of the set up.

A home built microscopy setup was used for the dispersive reflection and emission spectra. It consists of a microscope lens that focuses a broad band white light source (DH-2000-BAL, Ocean Optics) onto the cavity of interest. The reflected light was imaged on the slit of a monochromator (Princeton Instruments), couple to a charge-coupled device (CCD, Pixis, Princeton Instruments) detector to register the spectra. By using a Fourier lens, the angle resolved reflection spectra could be obtained. The reflection dispersion spectra were acquired for each cavity thickness, for both solutions of high concentration (strong coupling regime) and low concentration (weak coupling regime). The same microscopy set-up was used to obtain the angle resolved emission from each cavity. The system was excited at 532 nm using a continuous wave diode laser (Oxxius) with a focal spot of ~ 1.2 μm diameter and ~160 μW power. It should be noted the emission properties are independent of excitation wavelength.

### D- Emission Spectra Measurements at Normal Incidence

The emission spectra of the samples were collected in reflection mode using a Nikon Eclipse TE200 light microscope (illustrated in Figure 3.18 in Chapter 3), with a Nikon 40X objective having a 0.6 numerical aperture (NA) and 3.7-2.7 mm working distance (WD). After focusing at a point in the filled cavity, the system was excited in *epi* configuration by UV light produced by a mercury short arc HBO lamp (OSRAM). The excitation light was filtered by a Semrock bandpass filter centered at 365 nm. The emitted light from the cavities was collected by a spectrograph/CCD camera (Acton SP-300i/Roper ST133) coupled to the microscope. The emission spectrum was also recorded from the same channels in a region with only one mirror, the latter representing emission from the bare molecules. Emission spectra recorded for different cavity thicknesses recorded at normal incidence are shown in Figure 4.8.

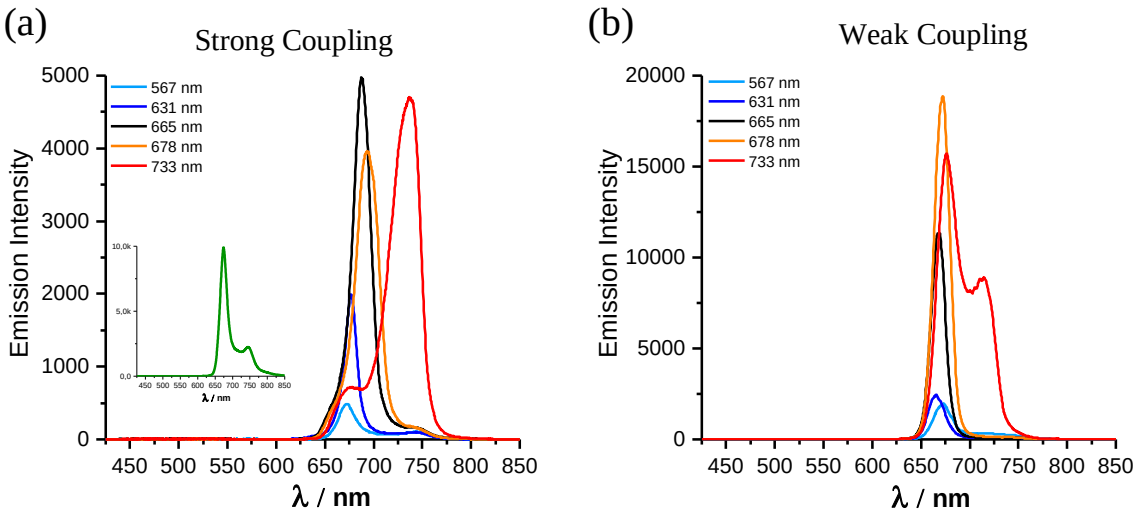



**Figure 4.8:** Emission spectra of Ce6 in DMF in cavities obtained at normal incidence for (a) high concentration (strong coupling regime) and (b) low concentration (weak coupling regime) and for different cavity detunings (indicated by the cavity peak wavelengths in neat DMF, 665 nm the resonant case). The inset in (a) is the emission spectrum of Ce6 at high concentration taken from a one-mirror channel.

As can be seen in Figure 4.8a, when the cavity is strongly red-detuned a large emission peak appears. This is especially apparent at high concentrations of Ce6 (0.18 M) used to achieve strong coupling and is attributed to excimer emission, peaking outside the cavity at ca. 745 nm (inset, Figure 4.8a). The fluorescence lifetime of the emission at 740 nm is longer than that observed for monomeric Ce6, while the excitation spectrum of this emission matches that of monomeric Ce6, perfectly in keeping with the emission properties of an excimer. This red-shifted emission >740 nm was thus excluded from the quantum yield determinations.

### E- Lifetime Measurements

The emission lifetimes were measured using the time-correlated single photon counting technique (TCSPC) on a Nikon Eclipse Ti confocal microscope coupled to a PicoQuant PicoHarp 300 pulse correlator. A 40X objective with 0.6 NA and 3.7-2.7 WD was employed. The excitation source was a picosecond pulsed diode laser (PicoQuant PDL 800-D) at 640 nm, instrument response-limited pulse width of 83 ps, repetition rate of 80 MHz and average power of 9 mW. The emitted photons were detected by a single photon avalanche diode (SPAD) detector. A 685 nm ± 10 nm bandpass filter was placed before the detector in order to measure emission only from monomeric Ce6-cavity interactions. The emission decay lifetimes could be well fit by single exponential decay profiles in all cases using using PicoQuant SymphoTime64 software.

## 4.2.3- Results and Discussions

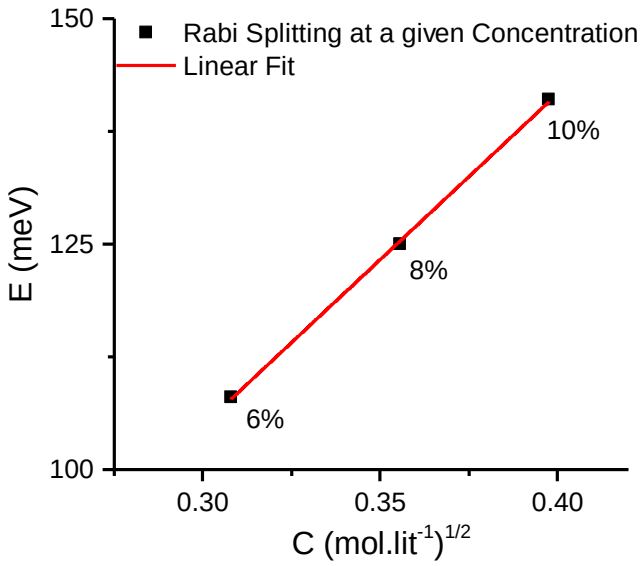



**Figure 4.9:** Variation of the Rabi splitting as a function of the square root of Ce6 concentration in DMF. The black squares are the Rabi splitting value corresponding to each concentration (6%, 8%, and 10% in weight in DMF), and the red line is their linear fit.

We recall from Chapters 1 and 2 that for a system with N molecules coupled to a resonant mode, the Rabi splitting is directly proportional to the square root of the concentration of molecules coupled to the field since $\hbar\Omega_R \propto \sqrt{\mathrm{N}/V} = \sqrt{C}$. The first mode of the fluidic FP nanocavities was coupled to Ce6 molecules having three different concentrations in DMF (6%, 8% and 10% in weight). The Rabi splitting values were recorded and plotted for each concentration respectively (see Figure 4.9). The linear fit of the recorded data (indicated by the red line in Figure 4.9) verifies the linear relationship of the Rabi splitting $\hbar\Omega_R$ to the square root of the molecular concentration $C$. So as we will show next, decreasing the concentration is one way to bring the system from the strong to the weak coupling regime.

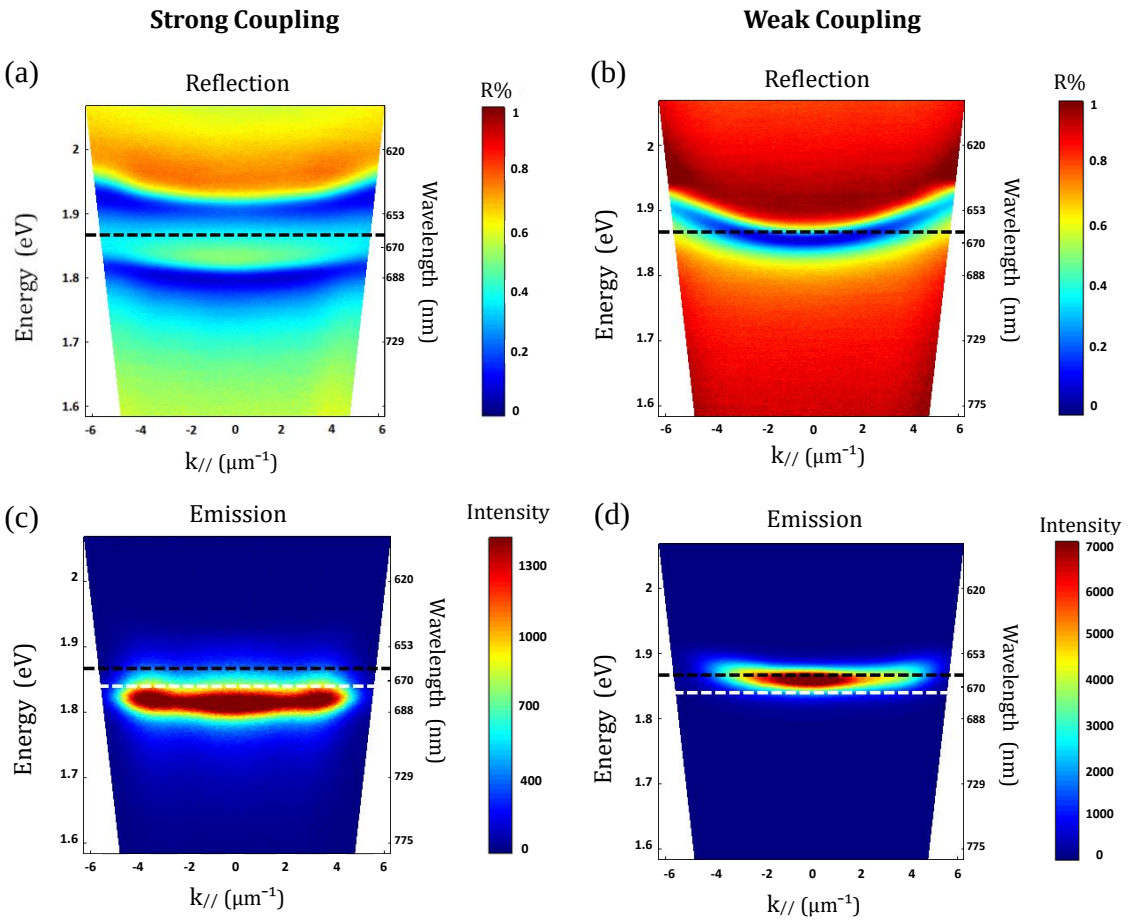



**Figure 4.10:** Angle resolved dispersion reflection spectra from high concentration (strong coupling regime) (a) and low concentration (weak coupling regime) (b) Ce6/DMF solution-filled cavities resonant with the Ce6 transition energy (dashed lines). The emission dispersion curves from the same cavities are shown in (c) and (d) with normal incidence excitation at 532 nm.

To study the properties of Ce6 under weak and strong coupling regime in liquid solution, samples with parallel FP cavities, such as in Figure 4.6, were prepared with a thick top mirror so that the spectroscopic measurements could be recorded in reflection mode. This has no particular consequence on the Q-factor.

Solutions of Ce6 in dimethylformamide (DMF), at high (0.18 M) and low concentrations (3.6 mM) were introduced into the nanocavities by capillarity. Reflection dispersion spectra for these two concentrations in cavities where the λ mode (Figure 4.3a) is resonant with the Ce6 absorption peak at 664 nm are plotted in Figures 4.10 a and 4.10

b respectively. In Figure 4.10 a, a mode splitting can be seen due to the strength of the interaction between the mode and molecular transition (represented by the dashed line in all Figures 4.10). The splitting has a value of ca. 110 meV, which is larger than the full width at half-maximum (FWHM) of both the molecular absorption peak (67 meV) and the FP resonance (62 meV). The system is therefore clearly in the strong coupling regime. The polaritonic states are dispersive due to the photonic character they inherit from the FP mode. As discussed above, the Rabi splitting depends on the square root of Ce6 concentration (see Figure 4.9) and at a certain threshold when the Rabi splitting becomes smaller than the FWHM of the original components, the system is no longer in the strong coupling regime. This is the case when the concentration is decreased by a factor of *ca.* 50 such as in Figure 4.10b. The FP mode then displays the normal parabolic dispersive shape and the system is in the weak coupling regime with no avoided crossing at the molecular absorption.

The emission dispersions in the strong and weak coupling regimes at resonance are displayed in Figures 3c and 3d. The emission of $P^-$ in the strong-coupling case (Figure 3c) is at slightly lower energies than that in the weak coupling regime and only the reflection dispersion curves reveal unambiguously whether the system is in the weak or strong coupling regimes. However, as we will see next, the effect of the coupling regime on the emission quantum yield and radiative lifetimes are quite distinct.

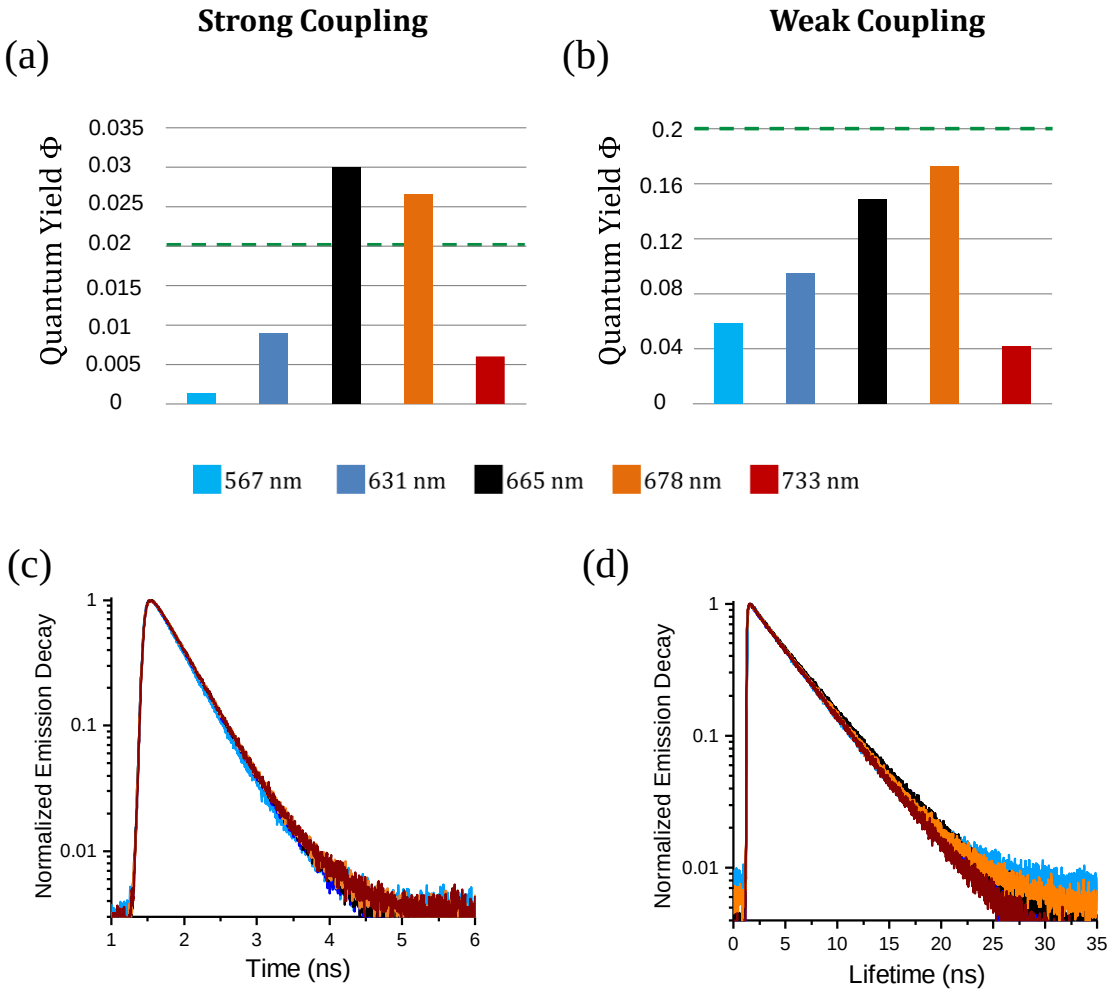



**Figure 4.11:** Emission quantum yield (a) and (b) and decay (c) and (d) as function of cavity mode detuning in the weak and strong coupling regimes respectively for Ce6 in DMF solution. Each cavity is represented by a colored cylinder based on its optical mode energy detuning relative to the molecule's absorption transition at 664 nm (i.e. cavities with photonic modes in neat DMF at 567 nm (light blue), 631 nm (blue), 665 nm (black), 678 nm (orange), and 733 nm (red)). The resonant case is in black. The green lines in (a) and (b) correspond to the emission quantum yields of the bare molecule at the same concentrations.

Figure 4.11a and 4.11b show the variation of the emission quantum yield as a function of cavity mode detuning in the strong and weak coupling regimes respectively. While the absolute value of Φ are determined within ± 10%, the relative values between different detunings are accurate up to the signal to noise ratio of the spectroscopic equipment. Firstly, we observe that the emission quantum yields in the strong coupling

case are always much lower than those in the weak coupling case due to self-quenching at high Ce6 concentration, discussed further down. In the strong coupling regime, the maximal quantum yield is achieved for the resonant cavity and decreases when the cavity is blue or red detuned. The yield at resonance is much higher than that of the bare molecule at the same concentration (dashed green line in Figure 4.11a). This likely reflects the enhanced radiative nature of the collective polaritonic state, and indeed the radiative rate constant $k_r$ (extracted from the emission lifetimes ($\tau$) (Figures 4.11c and 4.11d) and the quantum yield as $k_r = \Phi/\tau$) follows the same trend as the quantum yield for different detunings (see Table 4.1). Other studies have found both enhanced and suppressed emission quantum yields under strong coupling. [4,5,10] Such variations, which depend on the coupled molecules and the experimental conditions, reflect most likely differences in the non-radiative channels available for decay and the fact that $\Phi$ is dominated by $k_{nr}$ [59,87,143] (e.g. values in Table 1).

However, a different trend was observed in the weak coupling case, here the emission quantum yield is maximum when the cavity mode overlaps with the Ce6 fluorescence (orange bar in Figure 4b). Again this correlates with the extracted radiative rate (Table 4.1) and is the trend one would expect from a Purcell effect on the radiative decay rate of the molecule. It should however be noted that the emission quantum yield does not exceed that of the bare molecule in solution, perhaps because we are observing an averaging effect across the mode amplitude with some molecules experiencing very high mode density but others being at the central node or near the mirrors (Figure 1b).

In contrast to the quantum yields, the emission lifetimes measured from the cavities are nearly invariant as a function of detuning in both the weak and strong coupling regime. This is because the non-radiative rate constant $k_{nr}$ dominates $k_r$ in both weak and strong coupling regimes (Table 4.1). In the weak coupling limit (3.6 mM Ce6), $k_{nr}$ is determined mainly by the internal vibrational relaxation and inter-system crossing as its lifetime ~4.3 ns is similar to that in $10^{-5}$ M solutions where interactions between Ce6 molecules within the excited state lifetime are unlikely. In the strong coupling limit (0.18 M Ce6), excited Ce6 can also be quenched efficiently by interaction with surrounding Ce6 molecules in the ground state (self-quenching), increasing $k_{nr}$ by an order of magnitude.

**Table 4.1:** Measured fluorescence quantum yield (Φ), fluorescence lifetime (τ), and calculated radiative rate constant (kr) and non-radiative rate constant (knr) for DMF solutions of Chlorin e6 of 0.18 M concentration (strong coupling regime) and 3.6 mM concentration (weak coupling regime) in Fabry-Perot nanocavities with optical modes of various detunings (the on resonance mode is highlighted in green) relative to the Chlorin absorption at 664 nm.

Table 4.1: Radiative and non-radiative emission rates of Ce6 in DMF

Strong Coupling

| cavity resonance | ϕ | τ (ns) | $k_r$ ($s^{-1}$) | $k_{nr}$ ($s^{-1}$) |
|---|---|---|---|---|
| 567 nm | 1.4E-03 | 0.40 | 3.4E+06 | 2.5E+09 |
| 631 nm | 8.9E-03 | 0.42 | 2.1E+07 | 2.4E+09 |
| 665 nm | 3.0E-02 | 0.42 | 7.1E+07 | 2.3E+09 |
| 678 nm | 2.7E-02 | 0.42 | 6.3E+07 | 2.3E+09 |
| 733 nm | 6.0E-03 | 0.43 | 1.4E+07 | 2.3E+09 |

Weak Coupling

| cavity resonance | ϕ | τ (ns) | $k_r$ ($s^{-1}$) | $k_{nr}$ ($s^{-1}$) |
|---|---|---|---|---|
| 567 nm | 5.9E-02 | 4.0 | 1.5E+07 | 2.3E+08 |
| 631 nm | 9.5E-02 | 4.4 | 2.2E+07 | 2.1E+08 |
| 665 nm | 1.5E-01 | 4.5 | 3.3E+07 | 1.9E+08 |
| 678 nm | 1.7E-01 | 4.2 | 4.1E+07 | 2.0E+08 |
| 733 nm | 4.2E-02 | 4.2 | 1.0E+07 | 2.3E+08 |

## 4.2.4- Quantum Yield Calculation

The emission quantum yield Φ values were determined relative to that of dilute solutions of the bare Ce6, using the following equation:

$$\Phi_c = \Phi_R \cdot \frac{A_R(\lambda_{ex})}{E_R} \cdot \frac{E_c}{A_c(\lambda_{ex})} \cdot \frac{n_c^2\,(\lambda_{em})}{n_R^2\,(\lambda_{em})} \tag{4.7}$$

where $A$ is the fractional absorption ($1\text{-}10^{-\text{Absorbance}}$) at the excitation wavelength, $E$ the integral of emission counts, and $n$ the index of refraction of the solvent at the emission wavelength. Indices $c$ and $R$ represent the cavity and the reference molecule (Ce6)

respectively. Importantly, the quantum yields were referenced to Ce6 in dilute ethanol,[139,140] and transfer matrix simulations were used to determine the absorption in the Ce6/DMF layer in each cavity. Note that at high concentration, excimer emission is apparent at long wavelengths >740 nm for highly concentrated solutions and we excluded this from the analysis as explained in the Experimental Section. Reabsorption of the emission is minimal (<0.5%) even at the highest concentration used for strong coupling due to the extremely short pathlength.

The calculation of the fluorescence quantum yield values (Φ) for cavity emission were obtained through a two-step procedure as follows:[144]

i) Calculation of Ce6 quantum yield in DMF:

The Φ of Ce6 in DMF (Ce6-d) was determined by comparing it to that of the known value in ethanol[139,145] (0.15) using dilute solutions (~ 8 x $10^{-6}$ M) and correcting for the relative fraction of light absorbed as per equation (4.7). Steady-state fluorescence spectra were taken with a Horiba Jobin Yvon-Spex Fluorolog-3 fluorimeter, and the emission values were obtained by integrating the area under the spectra. The quantum yield of 8 x $10^{-6}$ M Ce6 in DMF was found to be 0.21. To determine Φ at higher concentrations (3.6 mM and 0.175M), where the solution becomes increasingly optically dense we assume that the radiative decay rates remain constant, but non-radiative decay rates increase with concentration due to self-quenching. In such conditions the quantum yield as a function of concentration can be obtained from the lifetime of the concentrated solution using:

$$\frac{\Phi_m}{\tau_m} = \frac{\Phi}{\tau} \tag{4.8}$$

where $\tau$ is the decay lifetime and the index $m$ is the value measured in dilute solution (here ~ 8 x $10^{-6}$ M Ce6). Consequently, the Φ values for Ce6 in DMF at 3.6 x $10^{-3}$ M and 0.18 M were found to be 0.2 and 0.0187 respectively.

ii) Calculation of the fluorescence quantum yield from FP cavities:

The final quantum yield values that are presented in Table 1 were calculated by using Equation (4.7) and using as reference the emission from one-mirror channels, assumed to have the quantum yield values determined in i) above. The total emission from each cavity was obtained by integrating the areas under the spectra up to 720 nm in Figure 4.8a and 4.8b, to avoid including excimer emission in the analysis**.** The absorbance values ($Abs$) from the one-mirror channels were calculated by using Beer Lambert's equation

$$Abs = C.\varepsilon.2d \tag{4.9}$$

where C the molecular concentration, $\varepsilon$ the molecule's extinction coefficient, $d$ is the channel path length and the factor 2 accounts for the fact that the excitation light is reflected off the back-mirror.

In the case of the FP cavities, the fraction of light absorbed in the Ce6/DMF layer at 365 nm (A) was obtained by using Transfer matrix simulations of the system (glass - Cr (2nm) – Ag (30nm) – Active layer (solution) – Ag (200nm)). These absorption values are related to Absorbance as:

$$A = 1 - 10^{-Abs} \tag{4.10}$$

Finally, after the calculation of the quantum yield, the radiative $k_r$ and non-radiative $k_{nr}$ rate constants in Table1 were calculated using the following equations:

$$\Phi = \frac{k_r}{k_r + k_{nr}} = \tau.k_r \tag{4.11}$$

which leads to:

$$k_r = \frac{\Phi}{\tau} \tag{4.12}$$

$$k_{nr} = \frac{1-\Phi}{\tau} \tag{4.13}$$

## 4.3- Conclusions

In summary we have succeeded in preparing nanoscale liquid Fabry-Perot nanocavities that have the excellent optical qualities necessary to observe strong coupling effects for molecular solutions. In particular we demonstrate the enhanced radiative nature of polaritonic states generated from concentrated DMF solutions of Chlorin e6. Our fabrication method allows for the facile preparation of FP nanocavities of any desired lateral shape and lateral extent up to the millimeter scale, but with exquisite control over the nanoscale thickness. Thus samples can be customized to various geometries and length scales for different experimental purposes. While these FP nanocavities were made with Ag mirrors, we have tested that the same approach can be used for other metals such as Au. Furthermore, many solvents including water are easily taken up by our cavities such that studies of biological systems in their native solvation environment become possible. The observation of light-matter strong coupling of electronic transitions in the liquid state opens the possibility to study other molecular processes in this regime where diffusion and orientation plays a role, such as chemistry, with potential to broaden the scope of this field immensely.

# Thesis Conclusions and Outlook

In general, the overall aim of this thesis was to contribute to the fundamental understanding of the strong coupling phenomenon of light with organic molecules by implementing new systems and techniques in order to investigate property modifications of coupled molecular systems with photonic resonances. Consequently our conclusion can be divided into two main headings which correspond to the tools we exploited to achieve strong coupling experimentally.

In our first project, we intended to take advantage of the open character of plasmonic structures in order to extract subsequently surface property modifications, such as wetting, induced by the strong coupling of merocyanine (MC) whose work-function had been found to be tunedunder similar conditions.[53] We overcame many experimental challenges such as milling resonant hole-array structures over relatively large areas (~ 1 $mm^2$) on the surface of metals, and observing the Rabi splitting experienced by the coupled MC molecules on the surface of these arrays. When considering future prospects, such large plasmonic structures should be ideal tools for surface-enhanced Raman scattering spectroscopy (SERS) and biosensing applications.[127]

The study of wetting on such structures by contact angle measurements encountered many difficulties. In particular, both the metal and polymer surfaces were restructured, damaged and contaminated by the evaporation of the water droplets used in the experiments. This happened even under very stringent purity conditions and therefore it became clear that such wetting experiments are not feasible with the current experimental conditions. Nevertheless, with some modifications, the original hypothesis of the experiment might still hold. For example, it would be possible to try replacing water by droplets by an inert liquid with high boiling point such that they would not experience quick evaporation.

Since many natural dynamic processes of molecules occur in the liquid phase, there was a need to find a system which allows us to explore strong coupling effects on

molecules dissolved in liquid solvents. Experiments in liquid solutions have only been achieved for vibrational strong coupling (VSC) where micro-fluidic Fabry-Perot (FP) cavities can be easily used.[42,45,77] In this second project, the strong coupling of molecular electronic transitions with resonant photonic modes was achieved in the liquid phase for the first time. This required the development of a fabrication method of Fabry-Perot nanocavities, having modes in the visible range, in which liquids can be introduced. The method is easy to implement and extends to the formation of custom cavities with various geometries and sizes based on the experimental requirements. Due to the fact that cavities with different modes and in various shapes can be fabricated on the same substrate, thus it opens the potential for an all-fluidic strong coupling chip.

To illustrate the potential of these systems, the photophysical properties of weakly and strongly coupled chlorin e6 (Ce6) molecules mixed in DMF solvent were studied. The emission quantum yield of Ce6 was observed to be larger for coupled molecules than the uncoupled ones. The quantum yield decreases as the system moves away from the strongly coupled resonance conditions. Moreover, a different trend was observed in the weak coupling case following what one would expect from a Purcell effect. The latter observation supports the conclusion that the quantum yield enhancement observed for the lower polariton relative to the bare molecule was a consequence of the strong coupling phenomenon.

In addition, unlike the emission quantum yield, the fluorescence lifetime decay did not result in any significant differences when measured for different detunings. The calculation of radiative and non-radiative decay constants reveals that the non-radiative relaxation processes dominates the radiative ones by two orders of magnitude. The non-radiative rates for different cavity detunings were also similar in value and this explains the absence of variation in fluorescence lifetimes. Building on these results, it would be interesting to look for coherence of emission from strongly coupled molecules in the liquid phase.

Other projects relying on coupling electronic transitions of molecules in the liquid phase are still in progress. For instance, recent theoretical studies report that collective interactions of dipoles with a photonic cavity can generate optomechanical effects, which might lead to a second order transition of the coupled dipoles from an isotropic to an aligned phase.[146] We believe that our system, in which molecules have freedom of movement, is ideal to verify experimentally this theory and perhaps show realignment effects of strongly coupled molecular dipoles.

This work has been technically very challenging. Nevertheless, our results are a small but important contribution to this emerging field of modified molecular properties under light-matter strong coupling. We believe that a number of molecular processes can and will be studied in the nano-fluidic cavity configuration developed here deepening our fundamental understanding and opening the door to future applications.

# References:

(1) Eugene Hecht. *Optics*, 4th Editio.; Alfred Zajac, Ed.; Addison-Wesley, 1987.

(2) G.R. Fowles. *Introduction to Modern Optics*; Courier Corporation, 2012.

(3) Haroche, S. Controlling Photons in a Box and Exploring the Quantum to Classical Boundary. *Ann. Phys.* **2013**, *525*, 753–776.

(4) M.Ducloy; D.Block. *Quantum Optics of Confinded Systems*; Kluwer Academic Publishers, 1996.

(5) Purcell, E. M. Spontaneous Emission Probabilities at Radio Frequencies. *Physical Review*. 1946, p 681.

(6) Főrster, T. 10th Spiers Memorial Lecture. Transfer Mechanisms of Electronic Excitation. *Discuss. Faraday Soc.* **1959**, *27*, 7–17.

(7) Kasha, M. Energy Transfer Mechanisms and the Molecular Exciton Model for Molecular Aggragates. *Radiat. Res.* **1963**, *20*, 55–70.

(8) Rodriguez, S. R. K. Classical and Quantum Distinctions between Weak and Strong Coupling. *Eur. J. Phys.* **2016**, *37*, 25802.

(9) Ebbesen, T. W. Hybrid Light-Matter States in a Molecular and Material Science Perspective. *Acc. Chem. Res.* **2016**, *49*, 2403–2412.

(10) Kaluzny, Y.; Goy, P.; Gross, M.; Raimond, J. M.; Haroche, S. Observation of Self-Induced Rabi Oscillations in Two-Level Atoms Excited inside a Resonant Cavity: The Ringing Regime of Superradiance. *Phys. Rev. Lett.* **1983**, *51*, 1175–1178.

(11) Rempe, G.; Walther, H.; Klein, N. Observation of Quantum Collapse and Revival in a One-Atom Maser. *Phys. Rev. Lett.* **1987**, *58*, 353–356.

(12) Raizen, M. G.; Thompson, R. J.; Brecha, R. J.; Kimble, H. J.; Carmichael, H. J. Normal-Mode Splitting and Linewidth Averaging for Two-State Atoms in an

Optical Cavity. *Phys. Rev. Lett.* **1989**, *63*, 240–243.

(13) Thompson, R. J.; Rempe, G.; Kimble, H. J. Observation of Normal-Mode Splitting for an Atom in an Optical Cavity. *Phys. Rev. Lett.* **1992**, *68*, 1132–1135.

(14) Haroche, S.; Raimond, J. M. *Exploring the Quantum: Atoms, Cavities, and Photons*, 1st Editio.; Oxford University Press, 2006.

(15) Haroche, S.; Kleppner, D. Cavity Quantum Electrodynamics. *Phys. Today* **1989**, *42*, 24–30.

(16) Andreani, L. C. *Strong Light-Matter Coupling From Atoms to Solid-State Systems*; Singapore: World Scientific, 2013.

(17) Deng, H.; Haug, H.; Yamamoto, Y. Exciton-Polariton Bose-Einstein Condensation. *Rev. Mod. Phys.* **2010**, *82*, 1489–1537.

(18) Weisbuch, C.; Nishioka, M.; Ishikawa, A.; Arakawa, Y. Observation of the Coupled Exciton-Photon Mode Splitting in a Semiconductor Quantum Microcavity. *Phys. Rev. Lett.* **1992**, *69*, 3314–3317.

(19) Houdré, R. Early Stages of Continuous Wave Experiments on Cavity-Polaritons. *Phys. Status Solidi Basic Res.* **2005**, *242*, 2167–2196.

(20) Houdré, R.; Weisbuch, C.; Stanley, R. P.; Oesterle, U.; Pellandini, P.; Ilegems, M. Measurement of Cavity-Polariton Dispersion Curve from Angle-Resolved Photoluminescence Experiments. *Phys. Rev. Lett.* **1994**, *73*, 2043–2046.

(21) Baumberg, J. J. Spin Condensates in Semiconductor Microcavities. In *Semiconductor Spintronics and Quantum Computation*; Awschalom, D. D., Loss, D., Samarth, N., Eds.; Springer Berlin Heidelberg: Berlin, Heidelberg, 2002; pp 195–219.

(22) Saba, M.; Ciuti, C.; Bloch, J.; Thierry-Mieg, V.; André, R.; Dang, L. S.; Kundermann, S.; Mura, A.; Bongiovanni, G.; Staehli, J. L.; Deveaud, B. High-Temperature Ultrafast Polariton Parametric Amplification in Semiconductor

Microcavities. *Nature* **2001**, *414* (6865), 731–735.

(23) Carusotto, I.; Ciuti, C. Quantum Fluids of Light. *Rev. Mod. Phys.* **2013**, *85*, 299–366.

(24) Khitrova, G.; Gibbs, H. M.; Kira, M.; Koch, S. W.; Scherer, A. Vacuum Rabi Splitting in Semiconductors. *Nat. Phys.* **2006**, *2*, 81–90.

(25) W Y Liang. Excitons. *Phys. Educ.* **1970**, *5*, 226.

(26) Sellers, I. R.; Semond, F.; Leroux, M.; Massies, J.; Disseix, P.; Henneghien, A. L.; Leymarie, J.; Vasson, A. Strong Coupling of Light with a and B Excitons in GaN Microcavities Grown on Silicon. *Phys. Rev. B - Condens. Matter Mater. Phys.* **2006**, *73*, 1–4.

(27) Gómez, D. E.; Vernon, K. C.; Mulvaney, P.; Davis, T. J. Surface Plasmon Mediated Strong Exciton-Photon Coupling in Semiconductor Nanocrystals. *Nano Lett.* **2010**, *10*, 274–278.

(28) Liu, X.; Galfsky, T.; Sun, Z.; Xia, F.; Lin, E. Strong Light-Matter Coupling in Two-Dimensional Atomic Crystals. *Nat. Photonics* **2015**, *9*, 30–34.

(29) Wang, S.; Li, S.; Chervy, T.; Shalabney, A.; Azzini, S.; Orgiu, E.; Hutchison, J. A.; Genet, C.; Samorì, P.; Ebbesen, T. W. Coherent Coupling of WS2 Monolayers with Metallic Photonic Nanostructures at Room Temperature. *Nano Lett.* **2016**, *16*, 4368–4374.

(30) Reithmaier, J. P.; Sek, G.; Löffler, A.; Hofmann, C.; Kuhn, S.; Reitzenstein, S.; Keldysh, L. V; Kulakovskii, V. D.; Reinecke, T. L.; Forchel, A. Strong Coupling in a Single Quantum Dot-Semiconductor Microcavity System. *Nature* **2004**, *432*, 197–200.

(31) Agranovich, V. M.; Malshukov, A. G. Surface Polariton Spectra If The Resonance with the Transition Layer Vibrations Exist. *Opt. Commun.* **1974**, *11*, 169–171.

(32) Pockrand, I.; Brillante, A.; Möbius, D. Exciton–surface Plasmon Coupling: An

Experimental Investigation. *J. Chem. Phys.* **1982**, *77*, 6289–6295.

(33) Lidzey, D. G.; Bradley, D. D. C.; Skolnick, M. S.; Virgili, T.; Walker, S.; Whittaker, D. M. Strong Exciton-Photon Coupling in an Organic Semiconductor Microcavity. *Nature* **1998**, *395*, 53–55.

(34) Fujita, T.; Sato, Y.; Kuitani, T.; Ishihara, T. Tunable Polariton Absorption of Distributed Feedback Microcavities at Room Temperature. *Phys. Rev. B* **1998**, *57* (19), 12428–12434.

(35) Kéna-Cohen, S.; Forrest, S. R. Room-Temperature Polariton Lasing in an Organic Single-Crystal Microcavity. *Nat. Photonics* **2010**, *4*, 371–375.

(36) Ramezani, M.; Halpin, A.; Fernández-Domínguez, A. I.; Feist, J.; Rodriguez, S. R.-K.; Garcia-Vidal, F. J.; Gómez-Rivas, J. Plasmon-Exciton-Polariton Lasing. *Optica* **2016**, *4*, 22–27.

(37) Daskalakis, K. S.; Maier, S. a; Murray, R.; Kéna-Cohen, S. Nonlinear Interactions in an Organic Polariton Condensate. *Nat. Mater.* **2014**, *13*, 271–278.

(38) Plumhof, J. D.; Stöferle, T.; Mai, L.; Scherf, U.; Mahrt, R. F. Room-Temperature Bose–Einstein Condensation of Cavity Exciton–polaritons in a Polymer. *Nat. Mater.* **2013**, *13*, 247–252.

(39) Atkin, P.; Paula, J. *Physical Chemistry*; 2006.

(40) Schwartz, T.; Hutchison, J. A.; Genet, C.; Ebbesen, T. W. Reversible Switching of Ultrastrong Light-Molecule Coupling. *Phys. Rev. Lett.* **2011**, *106*, 196405–(1–4).

(41) Törmä, P.; Barnes, W. L. Strong Coupling between Surface Plasmon Polaritons and Emitters: A Review. *Rep. Prog. Phys.* **2015**, *78*, 13901.

(42) George, J.; Chervy, T.; Shalabney, A.; Devaux, E.; Hiura, H.; Genet, C.; Ebbesen, T. W. Multiple Rabi Splittings under Ultrastrong Vibrational Coupling. *Phys. Rev. Lett.* **2016**, *117*, 1–5.

(43) George, J.; Wang, S.; Chervy, T.; Canaguier-Durand, A.; Schaeffer, G.; Lehn, J.-

M.; Hutchison, J. a; Genet, C.; Ebbesen, T. W. Ultra-Strong Coupling of Molecular Materials: Spectroscopy and Dynamics. *Faraday Discuss.* **2015**, 281–294.

(44) Kéna-Cohen, S.; Maier, S. A.; Bradley, D. D. C. Ultrastrongly Coupled Exciton-Polaritons in Metal-Clad Organic Semiconductor Microcavities. *Adv. Opt. Mater.* **2013**, *1*, 827–833.

(45) George, J.; Shalabney, A.; Hutchison, J. A.; Genet, C.; Ebbesen, T. W. Liquid-Phase Vibrational Strong Coupling. *J. Phys. Chem. Lett.* **2015**, *6*, 1027–1031.

(46) Fontcuberta i Morral, A.; Stellacci, F. Light-Matter Interactions: Ultrastrong Routes to New Chemistry. *Nat. Mater.* **2012**, *11*, 272–273.

(47) Orgiu, E.; George, J.; Hutchison, J. a.; Devaux, E.; Dayen, J. F.; Doudin, B.; Stellacci, F.; Genet, C.; Schachenmayer, J.; Genes, C.; Pupillo, G.; Samorì, P.; Ebbesen, T. W. Conductivity in Organic Semiconductors Hybridized with the Vacuum Field. *Nat. Mater.* **2014**, *14*, 1123–1130.

(48) Coles, D. M.; Somaschi, N.; Michetti, P.; Clark, C.; Lagoudakis, P. G.; Savvidis, P. G.; Lidzey, D. G. Polariton-Mediated Energy Transfer between Organic Dyes in a Strongly Coupled Optical Microcavity. *Nat. Mater.* **2014**, *13*, 712–719.

(49) Holmes, R. J.; Forrest, S. R. Strong Exciton-Photon Coupling and Exciton Hybridization in a Thermally Evaporated Polycrystalline Film of an Organic Small Molecule. *Phys. Rev. Lett.* **2004**, *93*, 1–4.

(50) Bellessa, J.; Symonds, C.; Laverdant, J.; Benoit, J.-M.; Plenet, J. C.; Vignoli, S. Strong Coupling between Plasmons and Organic Semiconductors. *Electronics* **2014**, *3*, 303–313.

(51) Gubbin, C. R.; Maier, S. A.; Kéna-Cohen, S. Low-Voltage Polariton Electroluminescence from an Ultrastrongly Coupled Organic Light-Emitting Diode. *Appl. Phys. Lett.* **2014**, *104*.

(52) Lunz, M.; de Boer, D.; Lozano, G.; Rodriguez, S. R. K.; Gómez-Rivas, J.;

Verschuuren, M. A. Plasmonic LED Device. *Proc.SPIE* **2014**, *9127*, 91270N–91270N–6.

(53) Hutchison, J. A.; Liscio, A.; Schwartz, T.; Canaguier-Durand, A.; Genet, C.; Palermo, V.; Samorì, P.; Ebbesen, T. W. Tuning the Work-Function via Strong Coupling. *Adv. Mater.* **2013**, *25*, 2481–2485.

(54) Shalabney, A.; George, J.; Hiura, H.; Hutchison, J. A.; Genet, C.; Hellwig, P.; Ebbesen, T. W. Enhanced Raman Scattering from Vibro-Polariton Hybrid States. *Angew. Chemie - Int. Ed.* **2015**, *54*, 7971–7975.

(55) Hao, Y. W.; Wang, H. Y.; Jiang, Y.; Chen, Q. D.; Ueno, K.; Wang, W. Q.; Misawa, H.; Sun, H. B. Hybrid-State Dynamics of Gold Nanorods/dye J-Aggregates under Strong Coupling. *Angew. Chemie - Int. Ed.* **2011**, *50*, 7824–7828.

(56) Schwartz, T.; Hutchison, J. A.; Léonard, J.; Genet, C.; Haacke, S.; Ebbesen, T. W. Polariton Dynamics under Strong Light-Molecule Coupling. *ChemPhysChem* **2013**, *14*, 125–131.

(57) Tischler, J. R.; Scott Bradley, M.; Zhang, Q.; Atay, T.; Nurmikko, A.; Bulović, V. Solid State Cavity QED: Strong Coupling in Organic Thin Films. *Org. Electron.* **2007**, *8*, 94–113.

(58) Wiederrecht, G. P.; Hall, J. E.; Bouhelier, A. Control of Molecular Energy Redistribution Pathways via Surface Plasmon Gating. *Phys. Rev. Lett.* **2007**, *98*, 1–4.

(59) Wang, S.; Chervy, T.; George, J.; Hutchison, J. A.; Genet, C.; Ebbesen, T. W. Quantum Yield of Polariton Emission from Hybrid Light-Matter States. *J. Phys. Chem. Lett.* **2014**, *5*, 1433–1439.

(60) Zhong, X.; Chervy, T.; Wang, S.; George, J.; Thomas, A.; Hutchison, J. A.; Devaux, E.; Genet, C.; Ebbesen, T. W. Non-Radiative Energy Transfer Mediated by Hybrid Light-Matter States. *Angew. Chemie - Int. Ed.* **2016**, *55*, 6202–6206.

(61) Tischler, J. R.; Bradley, M. S.; Bulović, V.; Song, J. H.; Nurmikko, A. Strong Coupling in a Microcavity LED. *Phys. Rev. Lett.* **2005**, *95*, 1–4.

(62) Vasa, P.; Wang, W.; Pomraenke, R.; Lammers, M.; Maiuri, M.; Manzoni, C.; Cerullo, G.; Lienau, C. Real-Time Observation of Ultrafast Rabi Oscillations between Excitons and Plasmons in J-Aggregate/metal Hybrid Nanostructures. *2013 Conf. Lasers Electro-Optics Eur. Int. Quantum Electron. Conf. CLEO/Europe-IQEC 2013* **2013**, *7*, 1–5.

(63) Aberra Guebrou, S.; Symonds, C.; Homeyer, E.; Plenet, J. C.; Gartstein, Y. N.; Agranovich, V. M.; Bellessa, J. Coherent Emission from a Disordered Organic Semiconductor Induced by Strong Coupling with Surface Plasmons. *Phys. Rev. Lett.* **2012**, *108*, 1–5.

(64) Shi, L.; Hakala, T. K.; Rekola, H. T.; Martikainen, J. P.; Moerland, R. J.; Törmä, P. Spatial Coherence Properties of Organic Molecules Coupled to Plasmonic Surface Lattice Resonances in the Weak and Strong Coupling Regimes. *Phys. Rev. Lett.* **2014**, *112*.

(65) Lagoudakis, P. Polariton Condensates: Going Soft. *Nat. Mater.* **2014**, *13*, 227–228.

(66) Chervy, T.; Xu, J.; Duan, Y.; Wang, C.; Mager, L.; Frerejean, M.; Münninghoff, J. A. W.; Tinnemans, P.; Hutchison, J. A.; Genet, C.; Rowan, A. E.; Rasing, T.; Ebbesen, T. W. High-Efficiency Second-Harmonic Generation from Hybrid Light-Matter States. *Nano Lett.* **2016**, 7352–7356.

(67) Chikkaraddy, R.; de Nijs, B.; Benz, F.; Barrow, S. J.; Scherman, O. A.; Rosta, E.; Demetriadou, A.; Fox, P.; Hess, O.; Baumberg, J. J. Single-Molecule Strong Coupling at Room Temperature in Plasmonic Nanocavities. *Nature* **2016**, *535*, 127–130.

(68) Hutchison, J. A.; Schwartz, T.; Genet, C.; Devaux, E.; Ebbesen, T. W. Modifying Chemical Landscapes by Coupling to Vacuum Fields. *Angew. Chemie - Int. Ed.* **2012**, *51*, 1592–1596.

(69) Hutchison, J. A.; Schwartz, T.; Genet, C.; Devaux, E.; Ebbesen, T. W. Modifying Chemical Landscapes by Coupling to Vacuum Fields. *Angew. Chemie - Int. Ed.* **2012**, *51*, 1592–1596.

(70) Wang, S.; Mika, A.; Hutchison, J. a; Genet, C.; Jouaiti, A.; Hosseini, M. W.; Ebbesen, T. W. Phase Transition of a Perovskite Strongly Coupled to the Vacuum Field. *Nanoscale* **2014**, *6*, 7243–7248.

(71) Holmes, R. J. Organic Polaritons: Long-Distance Relationships. *Nat. Mater.* **2014**, *13*, 669–670.

(72) Hakala, T. K.; Toppari, J. J.; Kuzyk, A.; Pettersson, M.; Tikkanen, H.; Kunttu, H.; Törmä, P. Vacuum Rabi Splitting and Strong-Coupling Dynamics for Surface-Plasmon Polaritons and Rhodamine 6G Molecules. *Phys. Rev. Lett.* **2009**, *103*, 1–4.

(73) Shalabney, A.; George, J.; Hutchison, J. a.; Pupillo, G.; Genet, C.; Ebbesen, T. W. Coherent Coupling of Molecular Resonators with a Microcavity Mode. *Nat. Commun.* **2015**, *6*, 5981.

(74) Simpkins, B. S.; Fears, K. P.; Dressick, W. J.; Spann, B. T.; Dunkelberger, A. D.; Owrutsky, J. C. Spanning Strong to Weak Normal Mode Coupling between Vibrational and Fabry–Pérot Cavity Modes through Tuning of Vibrational Absorption Strength. *ACS Photonics* **2015**, *2*, 1460–1467.

(75) Dunkelberger, A. D.; Spann, B. T.; Fears, K. P.; Simpkins, B. S.; Owrutsky, J. C. Modified Relaxation Dynamics and Coherent Energy Exchange in Coupled Vibration-Cavity Polaritons. *Nat. Commun.* **2016**, *7*, 13504.

(76) Thomas, A.; George, J.; Shalabney, A.; Dryzhakov, M.; Varma, S. J.; Moran, J.; Chervy, T.; Zhong, X.; Devaux, E.; Genet, C.; Hutchison, J. A.; Ebbesen, T. W. Ground-State Chemical Reactivity under Vibrational Coupling to the Vacuum Electromagnetic Field. *Angew. Chemie - Int. Ed.* **2016**, *55*, 11462–11466.

(77) Vergauwe, R. M. A.; George, J.; Chervy, T.; Hutchison, J. A.; Shalabney, A.;

Torbeev, V. Y.; Ebbesen, T. W. Quantum Strong Coupling with Protein Vibrational Modes. *J. Phys. Chem. Lett.* **2016**, *7*, 4159–4164.

(78) Coles, D. M.; Yang, Y.; Wang, Y.; Grant, R. T.; Taylor, R. A.; Saikin, S. K.; Aspuru-Guzik, A.; Lidzey, D. G.; Kuo, J.; Tang, -Hsiang; Smith, J. M. Strong Coupling between Chlorosomes of Photosynthetic Bacteria and a Confined Optical Cavity Mode. *Nat. Commun.* **2014**, *5*, 5561.

(79) González-Tudela, A.; Huidobro, P. A.; Martín-Moreno, L.; Tejedor, C.; García-Vidal, F. J. Theory of Strong Coupling between Quantum Emitters and Propagating Surface Plasmons. *Phys. Rev. Lett.* **2013**, *110*, 126801.

(80) Flick, J.; Ruggenthaler, M.; Appel, H.; Rubio, A. Atoms and Molecules in Cavities, from Weak to Strong Coupling in Quantum-Electrodynamics (QED) Chemistry. *Proc. Natl. Acad. Sci.* **2017**, *114*, 3026–3034.

(81) Schachenmayer, J.; Genes, C.; Tignone, E.; Pupillo, G. Cavity-Enhanced Transport of Excitons. *Phys. Rev. Lett.* **2015**, *114*, 1–6.

(82) Herrera, F.; Spano, F. C. Cavity-Controlled Chemistry in Molecular Ensembles. *Phys. Rev. Lett.* **2016**, *116*, 1–6.

(83) Kowalewski, M.; Bennett, K.; Mukamel, S. Non-Adiabatic Dynamics of Molecules in Optical Cavities. *J. Chem. Phys.* **2016**, *144*, 1–8.

(84) Del Pino, J.; Feist, J.; Garcia-Vidal, F. J. Signatures of Vibrational Strong Coupling in Raman Scattering. *J. Phys. Chem. C* **2015**, *119*, 29132–29137.

(85) Marchetti, F. M.; Keeling, J. Collective Pairing of Resonantly Coupled Microcavity Polaritons. *Phys. Rev. Lett.* **2014**, *113*, 1–5.

(86) Gómez, D. E.; Lo, S. S.; Davis, T. J.; Hartland, G. V. Picosecond Kinetics of Strongly Coupled Excitons and Surface Plasmon Polaritons. *J. Phys. Chem. B* **2013**, *117*, 4340–4346.

(87) Grant, R. T.; Michetti, P.; Musser, A. J.; Gregoire, P.; Virgili, T.; Vella, E.;

Cavazzini, M.; Georgiou, K.; Galeotti, F.; Clark, C.; Clark, J.; Silva, C.; Lidzey, D. G. Efficient Radiative Pumping of Polaritons in a Strongly Coupled Microcavity by a Fluorescent Molecular Dye. *Adv. Opt. Mater.* **2016**, *4*, 1615–1623.

(88) Canaguier-Durand, A.; Genet, C.; Lambrecht, A.; Ebbesen, T. W.; Reynaud, S. Non-Markovian Polariton Dynamics in Organic Strong Coupling. *Eur. Phys. J. D* **2015**, *69*.

(89) Jackson, J. D. Classical Electrodynamics. John Wiley & Sons, Inc. 1962.

(90) Oughstun, K.; Cartwright, N. On the Lorentz-Lorenz Formula and the Lorentz Model of Dielectric Dispersion: Addendum. *Opt. Express* **2003**, *11*, 2791–2792.

(91) Lucarini, V.; Saarinen, J. J.; Peiponen, K.-E.; Vartiainen, E. M. *Kramers-Kronig Relations in Optical Materials Research*; Springer: Berlin, 2005.

(92) Grusdt, F. Introduction to Cavity QED. **2011**, 1–8.

(93) Garraway, B. M. The Dicke Model in Quantum Optics: Dicke Model Revisited. *Philos. Trans. A. Math. Phys. Eng. Sci.* **2011**, *369*, 1137–1155.

(94) Radiation, S. I, 19&4. *Phys. Rev.* **1954**, *93*, 99–110.

(95) Bhaseen, M. J.; Mayoh, J.; Simons, B. D.; Keeling, J. Dynamics of Nonequilibrium Dicke Models. *Phys. Rev. A - At. Mol. Opt. Phys.* **2012**, *85*, 1–25.

(96) Tavis, M. Exact Solution for an N-Molecule Radiation-Field Hamiltonian. *Phys. Rev.* **1968**, *170*, 379–384.

(97) Barnes, W. L.; Dereux, A.; Ebbesen, T. W. Surface Plasmon Subwavelength Optics. *Nature* **2003**, *424*, 824–830.

(98) Stein, B.; Laluet, J. Y.; Devaux, E.; Genet, C.; Ebbesen, T. W. Surface Plasmon Mode Steering and Negative Refraction. *Phys. Rev. Lett.* **2010**, *105*, 1–4.

(99) Genet, C.; Ebbesen, T. W. Light in Tiny Holes. *Nature* **2007**, *445*, 39–46.

(100) Laluet, J. Y.; Drezet, A.; Genet, C.; Ebbesen, T. W. Generation of Surface Plasmons at Single Subwavelength Slits: From Slit to Ridge Plasmon. *New J. Phys.* **2008**, *10*.

(101) Yi, J. M.; Cuche, A.; de León-Pérez, F.; Degiron, A.; Laux, E.; Devaux, E.; Genet, C.; Alegret, J.; Martìn-Moreno, L.; Ebbesen, T. W. Diffraction Regimes of Single Holes. *Phys. Rev. Lett.* **2012**, *109*, 1–5.

(102) Raether, H. Surface Plasmons on Smooth and Rough Surfaces and on Gratings. *Springer Tracts Mod. Phys.* **1988**, *111*, 136.

(103) Hendry, E.; Garcia-Vidal, F. J.; Martin-Moreno, L.; Rivas, J. G.; Bonn, M.; Hibbins, A. P.; Lockyear, M. J. Optical Control over Surface-Plasmon-Polariton-Assisted THz Transmission through a Slit Aperture. *Phys. Rev. Lett.* **2008**, *100*, 26–29.

(104) Ditlbacher, H.; Krenn, J. R.; Felidj, N.; Lamprecht, B.; Schider, G.; Salerno, M.; Leitner, A.; Aussenegg, F. R. Fluorescence Imaging of Surface Plasmon Fields. *Appl. Phys. Lett.* **2002**, *80*, 404–406.

(105) Ritchie, R. H.; Arakawa, E. T.; Cowan, J. J.; Hamm, R. N. Surface-Plasmon Resonance Effect in Grating Diffraction. *Phys. Rev. Lett.* **1968**, *21*, 1530–1533.

(106) Gómez Rivas, J.; Schotsch, C.; Haring Bolivar, P.; Kurz, H. Enhanced Transmission of THz Radiation through Subwavelength Holes. *Phys. Rev. B* **2003**, *68*, 201306.

(107) Ebbesen, T. W.; Lezec, H. J.; Ghaemi, H. F.; T. Thio; A.Wolff, P.; Thio, T.; A.Wolff, P. Extraordinary Optical Transmission through Sub-Wavelength Hole Arrays. *Nature* **1998**, *86*, 1114–1117.

(108) Wood, R. W. Anomalous Diffraction Gratings. *Phys. Rev.* **1935**, *48*, 928–936.

(109) Ghaemi, H. F.; Thio, T.; Grupp, D. E.; Ebbesen, T. W.; Lezec, H. J. Surface Plasmons Enhance Optical Transmission through Subwavelength Holes. *Phys. Rev. B* **1998**, *58*, 6779–6782.

(110) Genet, C.; Van Exter, M. P.; Woerdman, J. P. Fano-Type Interpretation of Red Shifts and Red Tails in Hole Array Transmission Spectra. *Opt. Commun.* **2003**, *225*, 331–336.

(111) Krishnan, A.; Thio, T.; Kim, T. J.; Lezec, H. J.; Ebbesen, T. W.; Wolff, P. A.; Pendry, J.; Martin-Moreno, L.; Garcia-Vidal, F. J. Evanescently Coupled Resonance in Surface Plasmon Enhanced Transmission. *Opt. Commun.* **2001**, *200*, 1–7.

(112) Salomon, A.; Wang, S.; Hutchison, J. A.; Genet, C.; Ebbesen, T. W. Strong Light-Molecule Coupling on Plasmonic Arrays of Different Symmetry. *ChemPhysChem* **2013**, 1882–1886.

(113) Bracco, G.; Holst, B. *Surface Science Techniques*; 2013; Vol. 51.

(114) Saeki, F.; Baum, J.; Moon, H.; Yoon, J.-Y.; Kim, C.-J.; Garrell, R. L. Electrowetting on Dielectrics (EWOD): Reducing Voltage Requirements for Microfluidics. *Polym. Mater. Sci. Eng.* **2001**, *85*, 12–13.

(115) Khodayari, M.; Hahne, B.; Crane, N. B.; Volinsky, A. A. Floating Electrode Electrowetting on Hydrophobic Dielectric with an SiO2 Layer. *Appl. Phys. Lett.* **2013**, *102*, 1–13.

(116) Quéré, D. Rough Ideas on Wetting. *Phys. A Stat. Mech. its Appl.* **2002**, *313*, 32–46.

(117) Young, T. An Essay on the Cohesion of Fluids. *Philos. Trans. R. Soc. London* **1805**, *95*, 65–87.

(118) Lipowsky, R.; Lenz, P.; Swain, P. S. Wetting and Dewetting of Structured and Imprinted Surfaces. *Colloids Surfaces A Physicochem. Eng. Asp.* **2000**, *161*, 3–22.

(119) Wenzel, R. N. Resistance Of Solid Surfaces To Wetting By Water. *Ind. Eng. Chem.* **1936**, *28*, 988–994.

(120) Cassie, B. D.; Cassie, A. B. D.; Baxter, S. Of Porous Surfaces,. *Trans. Faraday*

*Soc.* **1944**, *40*, 546–551.

(121) Reyntjens, S.; Puers, R. A Review of Focused Ion Beam Applications in Microsystem Technology. *J. Micromechanics Microengineering* **2001**, *11*, 287–300.

(122) Kim, C. S.; Ahn, S. H.; Jang, D. Y. Review: Developments in Micro/nanoscale Fabrication by Focused Ion Beams. *Vacuum* **2012**, *86*, 1014–1035.

(123) Narayan, K.; Subramaniam, S. Focused Ion Beams in Biology. *Nat. Methods* **2015**, *12*, 1021–1031.

(124) Chau, T. T.; Bruckard, W. J.; Koh, P. T. L.; Nguyen, A. V. A Review of Factors That Affect Contact Angle and Implications for Flotation Practice. *Adv. Colloid Interface Sci.* **2009**, *150*, 106–115.

(125) Ohno, T.; Wadell, C.; Inagaki, S.; Shi, J.; Nakamura, Y.; Matsushita, S.; Sannomiya, T. Hole-Size Tuning and Sensing Performance of Hexagonal Plasmonic Nanohole Arrays. *Opt. Mater. Express* **2016**, *6*, 1594.

(126) Altewischer, E.; Genet, C.; van Exter, M. P.; Woerdman, J. P.; Alkemade, P. F. a; van Zuuk, A.; van der Drift, E. W. J. M. Polarization Tomography of Metallic Nanohole Arrays. *Opt. Lett.* **2005**, *30*, 90–92.

(127) Kumar, S.; Cherukulappurath, S.; Johnson, T. W.; Oh, S. H. Millimeter-Sized Suspended Plasmonic Nanohole Arrays for Surface-Tension-Driven Flow-through SERS. *Chem. Mater.* **2014**, *26*, 6523–6530.

(128) Lee, S. H.; Bantz, K. C.; Lindquist, N. C.; Oh, S. H.; Haynes, C. L. Self-Assembled Plasmonic Nanohole Arrays. *Langmuir* **2009**, *25*, 13685–13693.

(129) Vogel, N.; Goerres, S.; Landfester, K.; Weiss, C. K. A Convenient Method to Produce Close- and Non-Close-Packed Monolayers Using Direct Assembly at the Air-Water Interface and Subsequent Plasma-Induced Size Reduction. *Macromol. Chem. Phys.* **2011**, *212*, 1719–1734.

(130) Samanta, S.; Locklin, J. Formation of Photochromic Spiropyran Polymer Brushes via Surface-Initiated, Ring-Opening Metathesis Polymerization: Reversible Photocontrol of Wetting Behavior and Solvent Dependent Morphology Changes. *Langmuir* **2008**, *24*, 9558–9565.

(131) Dattilo, D.; Armelao, L.; Fois, G.; Mistura, G.; Maggini, M. Wetting Properties of Flat and Porous Silicon Surfaces Coated with a Spiropyran. *Langmuir* **2007**, *23*, 12945–12950.

(132) Athanassiou, A.; Lygeraki, M. I.; Pisignano, D.; Lakiotaki, K.; Varda, M.; Mele, E.; Fotakis, C.; Cingolani, R.; Anastasiadis, S. H. Photocontrolled Variations in the Wetting Capability of Photochromic Polymers Enhanced by Surface Nanostructuring. *Langmuir* **2006**, *22*, 2329–2333.

(133) Xu, Y.; Greeley, J.; Mavrikakis, M. Effect of Subsurface Oxygen on the Reactivity of the Ag(111) Surface. *J. Am. Chem. Soc.* **2005**, *127*, 12823–12827.

(134) Bao, X.; Muhler, M.; Pettinger, B.; Uchida, Y.; Lehmpfuhl, G.; Schlögl, R.; Ertl, G. The Effect of Water on the Formation of Strongly Bound Oxygen on Silver Surfaces. *Catal. Letters* **1995**, *32*, 171–183.

(135) Bahsoun, H.; Chervy, T.; Thomas, A.; Börjesson, K.; Hertzog, M.; George, J.; Devaux, E.; Genet, C.; Hutchison, J. A.; Ebbesen, T. W. Electronic Light-Matter Strong Coupling in Liquid Fabry-Perot Nanocavities. *ACS Photonics* **2017**, Submitted.

(136) Casey, S. R.; Sparks, J. R. Vibrational Strong Coupling of Organometallic Complexes. *J. Phys. Chem. C* **2016**, *120*, 28138–28143.

(137) Trichet, A. A. P.; Foster, J.; Omori, N. E.; James, D.; Dolan, P. R.; Hughes, G. M.; Vallance, C.; Smith, J. M. Open-Access Optical Microcavities for Lab-on-a-Chip Refractive Index Sensing. *Lab Chip* **2014**, *14*, 4244–4249.

(138) Paul, S.; Heng, P. W. S.; Chan, L. W. Optimization in Solvent Selection for Chlorin e6 in Photodynamic Therapy. *J. Fluoresc.* **2013**, *23*, 283–291.

(139) Zenkevich, E.; Sagun, E.; Knyukshto, V.; Shulga, A.; Mironov, A.; Efremova, O.; Bonnett, R.; Songca, S. P.; Kassem, M. Photophysical and Photochemical Properties of Potential Porphyrin and Chlorin Photosensitizers for PDT. *J. Photochem. Photobiol. B Biol.* **1996**, *33*, 171–180.

(140) Kay, A.; Humphry-Baker, R.; Graetzel, M. Artificial Photosynthesis. 2. Investigations on the Mechanism of Photosensitization of Nanocrystalline TiO2 Solar Cells by Chlorophyll Derivatives. *J. Phys. Chem.* **1994**, *98*, 952–959.

(141) Ferguson, G. S.; Chaudhury, M. K.; Sigal, G. B.; Whitesides, G. M. Contact Adhesion of Thin Gold Films on Elastomeric Supports: Cold Welding under Ambient Conditions. *Science (New York, N.Y.)*. 1991, pp 776–778.

(142) Kéna-Cohen, S.; Davanço, M.; Forrest, S. R. Strong Exciton-Photon Coupling in an Organic Single Crystal Microcavity. *Phys. Rev. Lett.* **2008**, *101*, 116401.

(143) Ballarini, D.; De Giorgi, M.; Gambino, S.; Lerario, G.; Mazzeo, M.; Genco, A.; Accorsi, G.; Giansante, C.; Colella, S.; D'Agostino, S.; Cazzato, P.; Sanvitto, D.; Gigli, G. Polariton-Induced Enhanced Emission from an Organic Dye under the Strong Coupling Regime. *Adv. Opt. Mater.* **2014**, *2*, 1076–1081.

(144) Würth, C.; Grabolle, M.; Pauli, J.; Spieles, M.; Resch-genger, U. Relative and Absolute Determination of Fluorescence Quantum Yields of Transparent Samples. *Nat. Protoc.* **2013**, *8*, 1535–1550.

(145) Kay, A.; Humphry-Baker, R.; Gratzel, M. Artificial Photosynthesis. 2. Investigations on the Mechanism of Photosensitization of Nanocrystalline TiO2 Solar Cells by Chlorophyll Derivatives. *J. Phys. Chem.* **1994**, *98*, 952–959.

(146) Cortese, E.; Lagoudakis, P.; Liberato, S. De. Collective Optomechanical Effects in Cavity Quantum Electrodynamics. *arXiv* **2017**, 1–6.

## Publication:

H. Bahsoun, A. Thomas, T. Chervy, K. Börjesson, M. Hertzog, J. George, E. Devaux, C. Genet, J.A. Hutchison, T.W. Ebbesen. *Light-Matter Strong Coupling in Liquid Fabry-Perot Nanocavities*. ACS Photonics, *accepted.*

---

## List of Attended Conferences:

1. H. Bahsoun, A. Thomas, T. Chervy, K. Börjesson, M. Hertzog, J. George, E. Devaux, C. Genet, J.A. Hutchison, T.W. Ebbesen; Poster "Light-Matter Strong Coupling in Liquid Fabry-Perot Nanocavities"; Advanced Nanomatierials - **Nanotech Conference 28-30/ 06/2017**, Paris

2. H. Bahsoun, A. Thomas, T. Chervy, K. Börjesson, M. Hertzog, J. George, E. Devaux, C. Genet, J.A. Hutchison, T.W. Ebbesen; Poster "Light-Matter Strong Coupling in Liquid Fabry-Perot Nanocavities"; Photochemistry and photophysics - **ICP 16-21/07/ 2017**, Strasbourg

**Introduction:**

Au cours des dernières années, des études ont montré que le couplage fort entre la matière et la lumière et la formation associée d'états hybrides lumière-matière (Figure 1) donnent lieu à des différente propriétés moléculaires et matérielles de celles des constituants originaux, à savoir le mode de lumière et la molécule subissant le couplage. Le régime de couplage fort (SC) a été exploré en détail dans différentes configurations expérimentales et étudié théoriquement par de nombreux groupes.[1–21] Des exemples de processus et propriétés modifiés sous couplage fort sont le taux de transfert d'énergie non-radiatif,[11] la conductivité[12] et la fonction de travail des matériaux semi-conducteurs[13] et le rendement quantique d'émission.[1]

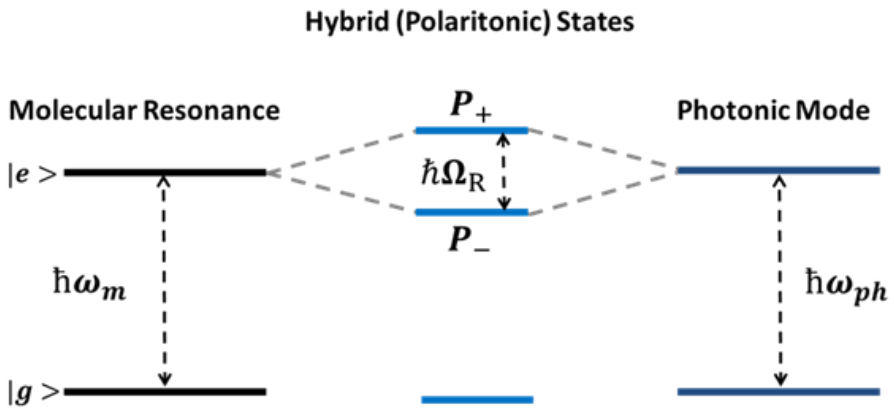



**Figure 1.** (a) Représentation schématique du couplage fort d'une transition moléculaire d'énergie $\hbar\omega_m$ et d'une résonance optique d'énergie $\hbar\omega_{ph}$ formant les états hybrides P + et P- séparés par l'énergie de séparation de Rabi $\hbar\Omega_R$.

Nous rappelons que lorsqu'un matériau avec un moment dipolaire de transition bien défini est placé dans un environnement électromagnétique (EM) avec des modes propres qui résonnent avec l'énergie d'une transition du matériau, ils peuvent interagir en échangeant de l'énergie grâce à des événements successifs d'émission et d'absorption. Si le taux de change de l'énergie est plus rapide que toute dissipation dans le système, l'interaction donnera lieu à la formation de deux nouveaux états hybrides ou polaritoniques, et on dit que le système est dans le régime de couplage fort.[14] Les deux nouveaux états, P + et P- représentés sur la figure 1a, sont séparés par une énergie appelée « séparation de Rabi » $\hbar\Omega_R$ (Figure 1). La théorie montre que même lorsque le nombre de photons dans

le système passe à zéro, la séparation de Rabi a encore une valeur finie. Ceci est dû à l'interaction du matériau avec les fluctuations d'énergie du point zéro du mode confiné.[15] Dans ce cas, le système est dit dans le régime de Rabi du vide, les conditions de toutes nos expériences durant cette thèse. Pour un système avec N molécules couplées avec un mode résonnant, la séparation de Rabi est directement proportionnelle à la racine carrée de la concentration de molécules couplée au champ : $\hbar\Omega_R \propto \sqrt{\mathrm{N}/V} = \sqrt{C}$. Ainsi, la diminution de la concentration est une façon d'amener le système du régime de couplage fort au couplage faible.

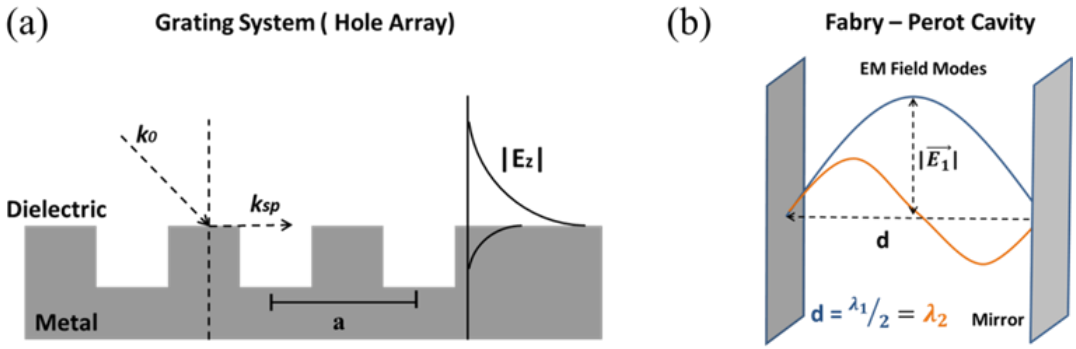



**Figure 2.** (a) Représentation schématique du couplage d'un système de réseau avec une périodicité a, indiquant la direction du vecteur $k_{sp}$ du moment du plasmon de surface. Le champ électrique évanescent ($E_z$) à l'interface métal-diélectrique est représenté par la ligne noire sur le côté droit de la figure. (b) Exemple schématique de l'amplitude des premier et deuxième modes de cavité Fabry-Pérot (FP) confinés entre deux miroirs métalliques parallèles.

L'environnement électromagnétique nécessaire pour le couplage fort de la matière légère peut être réalisé expérimentalement par plusieurs méthodes telles qu'une cavité Fabry-Perot (FP) ou des résonances plasmons de surface de nanostructures métalliques[16] (Figure 2). Dans nos premières expériences, nous avons utilisé des réseaux de trous périodiques afin de générer les polaritons de plasmon de surface (SPP) associés aux modes photoniques confinés à la surface d'un métal (Figure 2a). Ensuite, nous avons utilisé une cavité de Fabry-Pérot (FP) composée de deux miroirs parallèles séparés par une distance *d* qui est égale à un multiple de la moitié de la longueur d'onde du mode EM souhaité (Figure 2b). Nous pouvons diviser le travail principal de la thèse en deux parties, qui sont brièvement présentées comme suit:

- Dans la première partie, le couplage de la transition électronique moléculaire de merocyanine (MC) aux SPP résonnants a été exploré pour étudier sous couplage fort les modifications de la propriété de surface, en particulier l'énergie de surface par les changements dans les angles de mouillage de $H_2O$.
- Dans la deuxième partie, nous décrivons le développement d'une méthode efficace et facile pour la fabrication de cavités FP *nano-fluidiques* qui permettent d'étudier le couplage fort de molécules en solution ayant des transitions électroniques dans le visible. Pour démontrer le potentiel de ces FP nano-fluidiques, nous avons étudié les propriétés photo-physiques des molécules de Chlorin e6 (Ce6) en fonction du désaccord avec les modes de cavité. Nous montrons l'évolution de la durée de vie radiative et le rendement quantique d'émission de Ce6 en solution liquide dans les deux régimes de couplage faible et fort. Ce travail ouvre de nouvelles perspectives pour étudier des processus physico-chimiques en solution sous couplage fort.

**Résultats et Discussions:**

En 2013, Hutchison et al ont montré que la fonction de travail des molécules photochromiques de merocyanine (MC) pouvait être modifiée par couplage fort avec des SPP résonnants.[13] Un tel changement devrait entraîner à son tour un changement de la polarisabilité du milieu et donc de l'énergie libre de surface. Une façon de tester l'existence d'un tel changement consiste à mesurer l'angle de contact à l'interface entre des gouttelettes de liquide et la surface d'un film mince de molécules MC incorporées dans la matrice polymère PMMA, avant et après son couplage à des SPP résonnants (Figures 3a et 3b). Ici, nous notons que le spiropyran (SPI) est une molécule transparente dans le spectre visible qui peut être photo-isomérisée en MC sous irradiation UV, le processus inverse ayant lieu sous irradiation avec de la lumière visible. Cette qualité devait nous permettre de passer de manière réversible du couplage faible au fort en utilisant le même échantillon et d'acquérir des mesures dans des conditions où toutes les autres variables étaient constantes.[17,18]

Pour observer l'interaction entre des gouttelettes d'eau et le système fortement couplé, il nous a d'abord fallu développer une technique pour graver au FIB (faisceau à

ions focalisés) des réseaux périodiques dans un film d'Ag plus grand que les gouttelettes à mesurer, c'est-à-dire environ 1 mm x 1 mm (Figure 3c). La périodicité des réseaux est choisie pour générer des SPP ayant un mode résonnant avec le pic d'absorption de MC à 560 nm. Un couplage fort entre MC et SPP a ainsi été obtenu avec une séparation de Rabi ~ 470 meV (Figure 3d). Les mesures de l'angle de contact ont ensuite été effectuées à la surface de MC mélangées dans une matrice polymère de PMMA étalée sur la surface des réseaux de trous par centrifugation (spin-coating).

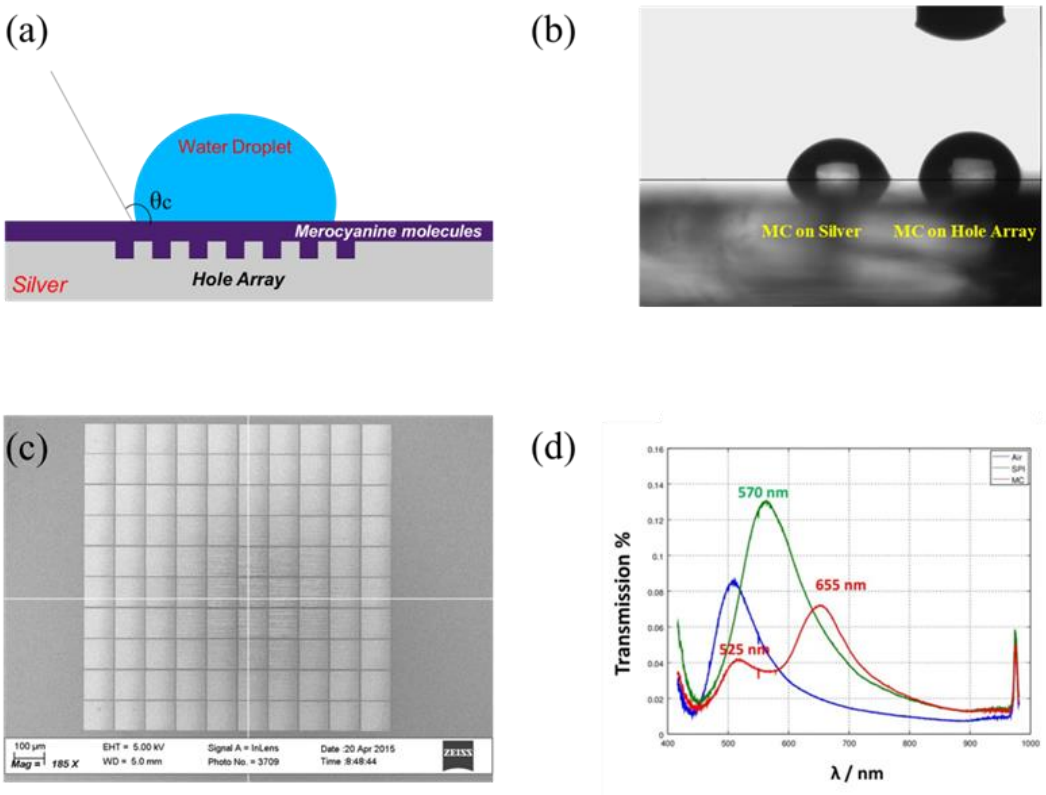



**Figure 3.** (a) Illustration schématique de l'expérience, montrant une gouttelette d'eau sur la couche de MC déposée au-dessus des trous gravés dans le film d'Ag et l'angle de contact (θc). (b) Une image de deux gouttes d'eau reposant sur la surface de la couche MC sur et hors du réseau de trous. (c) image SEM des grands réseaux de trous de 1 mm x 1 mm gravés à l'aide du système FIB Auriga. (d) Les spectres de transmission du réseau de trous Ag (bleu), avec une couche de SPI (vert) et avec la MC (rouge) respectivement.

Après de nombreux efforts, nous n'avons pas pu démontrer que l'angle de contact de l'eau est modifié aux interfaces eau-SPI et eau-MC même sous couplage fort. En effet, ces mesures se sont avérées très difficiles car nous avons constaté que les gouttelettes d'eau laissent un impact significatif sur la structure du film solide, ce qui entraîne des

changements immédiats dans les valeurs de l'angle de contact.[22] Après la caractérisation de ces modifications structurales utilisant la microscopie électronique à balayage (SEM), la microscopie à force atomique (AFM) et l'analyse par diffraction des rayons X électroniques (EDX), nous avons pu conclure que l'évaporation des gouttelettes affecte la rugosité de la surface du film polymérique et pouvait aussi laisser localement des impuretés (telles que Cl et Na) même lorsque nous utilisions de l'eau purifiée. Ces changements affectent non seulement la valeur de l'angle de contact pour une seule mesure, mais aussi rend très difficile la possibilité d'effectuer d'autres mesures sur le même ensemble de trous et de garantir la reproductibilité des résultats.

Dans un autre axe de recherche, nous avons cherché à explorer le couplage fort de molécules dans des solutions liquides car c'est la condition naturelle de nombreux processus moléculaires. Les expériences dans des solutions liquides n'ont été réalisées à ce jour que pour un couplage fort vibrationnel qui est facilité par le fait que les transitions vibrationnelles sont dans l'IR, ce qui permet d'utiliser des cavités micro-fluidiques FP[2,19-21] (e.g. espacement des miroirs ~ 10 μm). En revanche, le couplage fort électronique de molécules en solution liquide n'a pas jamais été signalé pour la simple raison que la longueur de la cavité dans le visible doit être de l'ordre de 100 nm, ce qui est techniquement très difficile à fabriquer. Entre autres, les miroirs de la cavité FP nano-fluidique (Figure 1b) doivent être uniformément plats sur une échelle beaucoup plus petite que la longueur de la cavité et la cavité doit être accessible à la solution.

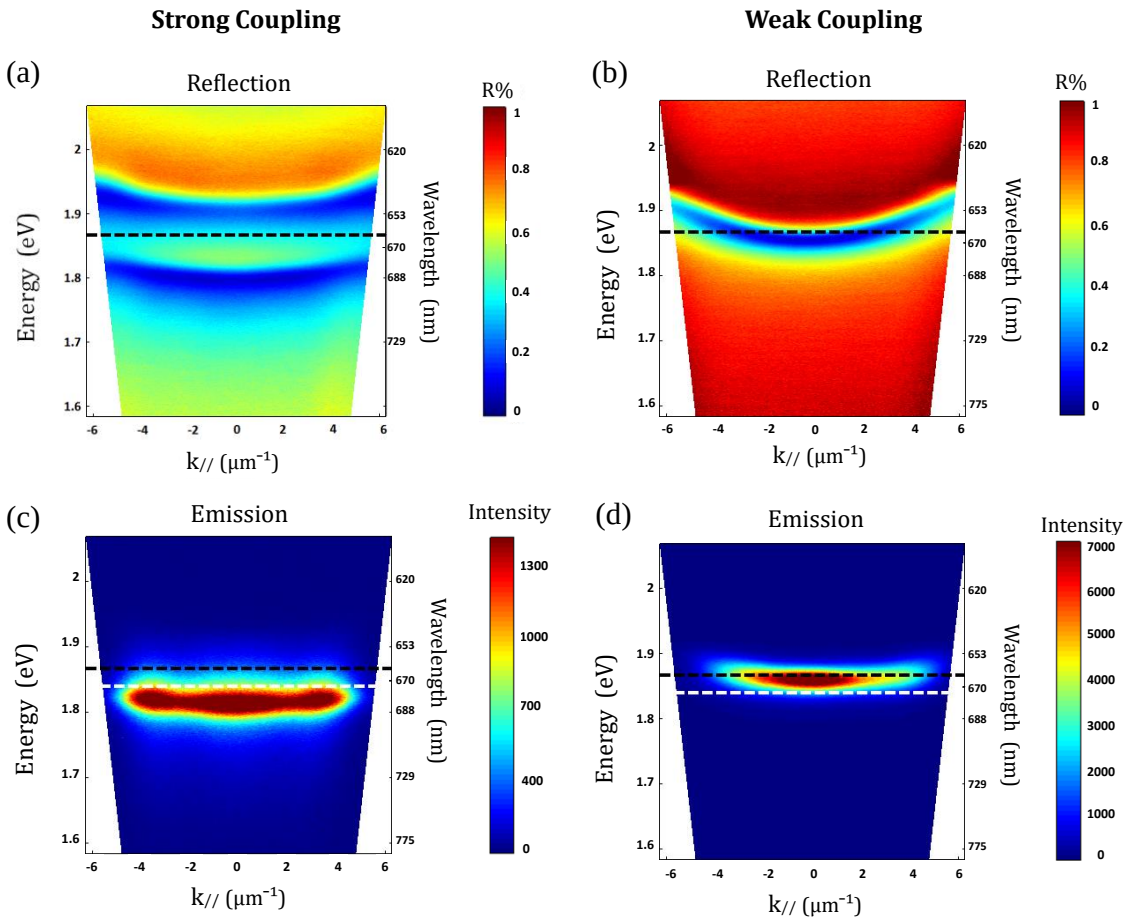



**Figure 4.** Spectres dispersifs de réflexion (a) à haute concentration (régime de couplage fort) et (b) à faible concentration (couplage faible) pour des cavités remplies de solution Ce6 / DMF résonnant avec l'énergie de transition du Ce6 (lignes pointillées). Les courbes de dispersion d'émission provenant des mêmes cavités sont indiquées en (c) et (d).

Dans ce travail de thèse, nous avons développé un processus original de fabrication des cavités FP nano-fluidiques accordables sur une large gamme de longueurs d'ondes visibles qui peuvent être remplies de liquides. Cette technique, détaillée dans la thèse, combine de la gravure au FIB, ainsi que de la soudure à froid sous pression des miroirs formant la cavité FP. Ces cavités ont un facteur de qualité suffisant pour être utilisé dans des expériences de couplage fort. Pour illustrer le potentiel de ces cavités, nous avons étudié les propriétés photo-physiques d'un analogue de la chlorophylle, Chlorin e6 (Ce6), dans les régimes de couplage faible et fort. En particulier, nous comparons le rendement

quantique d'émission et la constante radiative en fonction du désaccord dans les deux régimes qui met en évidence les caractéristiques distinctes de la condition de couplage fort.

Des solutions de Ce6 dans le di-méthyl-formamide (DMF), à haute concentration (0,18 M) et faibles concentration (3,6 mM) ont été introduites dans les nano-cavités par capillarité. Des exemples des spectres de dispersion d'émission et de réflexion pour ces deux concentrations dans les cavités sont montrés dans la Figure 4. L'anti-croisement (séparation de Rabi) en réflexion (Figure 4a) a une valeur de ca. 110 meV, qui est plus large que la pleine largeur à mi-hauteur du pic d'absorption moléculaire (67 meV) et de la résonance FP (62 meV). Le système est donc clairement dans le régime de couplage fort. Les états polaritoniques sont dispersifs en raison du caractère photonique qu'ils héritent du mode FP. Lorsque la concentration est diminuée d'un facteur d'environ 50 tel que dans la Figure 4b, il n'y a plus d'anti-croisement du pic car le système est maintenant dans le régime de couplage faible.

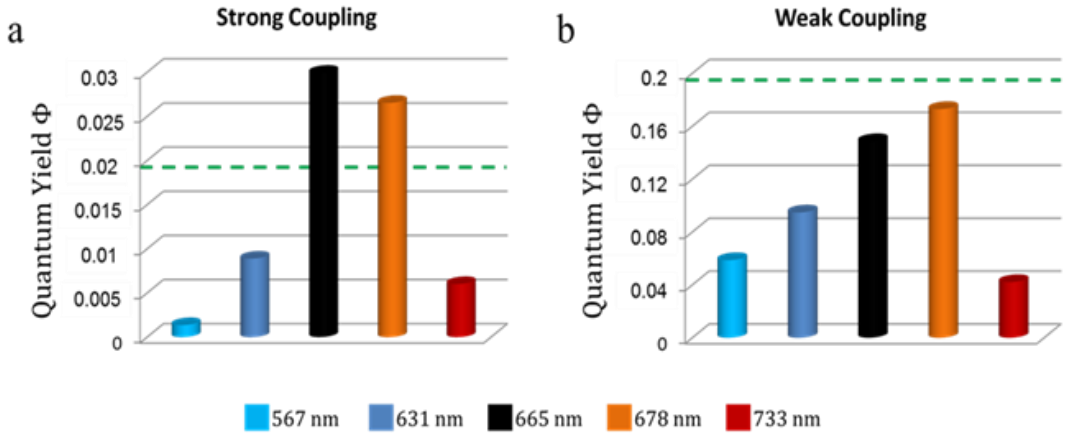



**Figure 5.** Le rendement quantique d'émission (a) et (b) en fonction du désaccord du mode cavité dans les régimes de couplages forts et faibles respectivement pour des solutions de Ce6 dans le DMF. Chaque cavité est représentée par un cylindre coloré basé sur son désaccord énergétique de mode optique par rapport à la transition d'absorption de la molécule à 664 nm. Les longueurs d'ondes précises pour chaque couleur sont en légende. Le cas résonnant est en noir. Les lignes vertes dans (a) et (b) correspondent aux rendements quantiques d'émission de la molécule nue aux mêmes concentrations.

Les valeurs Φ du rendement quantique d'émission ont été calculées et la variation du rendement quantique d'émission en fonction du désaccord du mode cavité dans les régimes de couplage fort et faible respectivement (Figures 5a et 5b). Dans le régime de couplage fort, le rendement quantique maximal est atteint pour la cavité résonnante et diminue lorsque la cavité est désaccordée dans le bleu ou le rouge. Cependant, une tendance différente a été observée dans le cas de couplage faible, ici le rendement quantique d'émission est maximal lorsque le mode cavité chevauche le spectre de fluorescence de Ce6. Ceci s'explique facilement par le fait que dans ce cas la densité d'état optique est maximum à la longueur d'émission ce qui augmente la constante radiative $k_r$ pour cette condition et ainsi Φ. De manière générale, on peut constater que les variations de Φ reflètent principalement les changements dans $k_r$ dans les deux régimes de couplage car la constante non-radiative est quasi-invariante du désaccord de la cavité.

**Conclusion:**

Durant cette thèse, nous avons exploré différents effets du couplage fort sur les processus et propriétés moléculaires. Même si les expériences sur le mouillage se sont avérées infructueuses par rapport au but recherché, cela a été très pédagogique. Nous avons réussi à préparer des nano-cavités Fabry-Pérot liquides nanométriques qui ont de très bonnes qualités optiques nécessaires pour observer les effets de couplage fort pour des solutions moléculaires. En particulier, nous montrons que la nature radiative des états polaritoniques est améliorée par rapport à ceux des molécules de Chlorin e6 non-couplées. Notre méthode de fabrication de FP nano-fluidiques est facile et sera accessible à d'autres chercheurs. Ainsi, les échantillons peuvent être personnalisés selon diverses géométries et échelles de longueur à des fins expérimentales différentes. L'observation du couplage fort des transitions électroniques à l'état liquide ouvre la possibilité d'étudier d'autres processus moléculaires dans ce régime que nous sommes déjà en train d'explorer.

## References:


(1) Wang, S.; Chervy, T.; George, J.; Hutchison, J. A.; Genet, C.; Ebbesen, T. W. *J. Phys. Chem. Lett.* **2014**, 1433–1439.

(2) Thomas, A.; George, J.; Shalabney, A.; Dryzhakov, M.; Varma, S. J.; Moran, J.; Chervy, T.; Zhong, X.; Devaux, E.; Genet, C.; Hutchison, J. A.; Ebbesen, T. W. *Angew. Chemie - Int. Ed.* **2016**, 11462–11466.

(3) Wang, S.; Mika, A.; Hutchison, J. a; Genet, C.; Jouaiti, A.; Hosseini, M. W.; Ebbesen, T. W. *Nanoscale* **2014**, 7243–7248.

(4) Kéna-Cohen, S.; Forrest, S. R. *Nat. Photonics* **2010**, 371–375.

(5) Vergauwe, R. M. A.; George, J.; Chervy, T.; Hutchison, J. A.; Shalabney, A.; Torbeev, V. Y.; Ebbesen, T. W. *J. Phys. Chem. Lett.* **2016**, 4159–4164.

(6) Chervy, T.; Xu, J.; Duan, Y.; Wang, C.; Mager, L.; Frerejean, M.; Münninghoff, J. A. W.; Tinnemans, P.; Hutchison, J. A.; Genet, C.; Rowan, A. E.; Rasing, T.; Ebbesen, T. W. *Nano Lett.* **2016**, 7352-7356.

(7) Shalabney, A.; George, J.; Hiura, H.; Hutchison, J. A.; Genet, C.; Hellwig, P.; Ebbesen, T. W. *Angew. Chemie - Int. Ed.* **2015**, 7971–7975.

(8) Galego, J.; Garcia-Vidal, F. J.; Feist, J. *Phys. Rev. X* **2015**, 1–14.

(9) Herrera, F.; Spano, F. C. *Phys. Rev. Lett.* **2016**, 1–6.

(10) Litinskaya, M.; Tignone, E.; Pupillo, G. *J. Phys. B At. Mol. Opt. Phys.* **2016**, 164006.

(11) Zhong, X.; Chervy, T.; Wang, S.; George, J.; Thomas, A.; Hutchison, J. A.; Devaux, E.; Genet, C.; Ebbesen, T. W. *Angew. Chemie - Int. Ed.* **2016**, 6202–6206.

(12) Orgiu, E.; George, J.; Hutchison, J. a.; Devaux, E.; Dayen, J. F.; Doudin, B.; Stellacci, F.; Genet, C.; Schachenmayer, J.; Genes, C.; Pupillo, G.; Samorì, P.; Ebbesen, T. W. *Nat. Mater.* **2014**, 1123 - 1130.

(13) Hutchison, J. A.; Liscio, A.; Schwartz, T.; Canaguier-Durand, A.; Genet, C.; Palermo, V.; Samorì, P.; Ebbesen, T. W. *Adv. Mater.* **2013**, 2481–2485.

(14) Haroche, S.; Kleppner, D. *Phys. Today* **1989**, 24–30.

(15) Ebbesen, T. W. *Acc. Chem. Res.* **2016**, 2403–2412.

(16) Törmä, P.; Barnes, W. L. *Rep. Prog. Phys.* **2015**, 13901.

(17) Schwartz, T.; Hutchison, J. A.; Genet, C.; Ebbesen, T. W. *Phys. Rev. Lett.* **2011**, 196405.

(18) Hutchison, J. A.; Schwartz, T.; Genet, C.; Devaux, E.; Ebbesen, T. W. *Angew. Chemie - Int. Ed.* **2012**, 1592–159.

(19) George, J.; Chervy, T.; Shalabney, A.; Devaux, E.; Hiura, H.; Genet, C.; Ebbesen, T. W. *Phys. Rev. Lett.* **2016**, 1–5.

(20) Shalabney, A.; George, J.; Hutchison, J. a.; Pupillo, G.; Genet, C.; Ebbesen, T. W. *Nat. Commun.* **2015**, 5981.

(21) Simpkins, B. S.; Fears, K. P.; Dressick, W. J.; Spann, B. T.; Dunkelberger, A. D.; Owrutsky, J. C. *ACS Photonics* **2015**, 1460–1467.

(22) Hejazi, V.; Moghadam, A. D.; Rohatgi, P.; Nosonovsky, M. *Langmuir* **2014**, 9423–9429.